

# Feedback control of spatially evolving flows

by

Espen Åkervik

March 2007  
Technical Reports from  
Linné Flow Centre  
KTH Mechanics  
Royal Institute of Technology  
SE-100 44 Stockholm, Sweden

Typsatt i  $\mathcal{A}\mathcal{M}\mathcal{S}$ - $\mathcal{L}\mathcal{A}\mathcal{T}\mathcal{E}\mathcal{X}$ .

Akademisk avhandling som med tillstånd av Kungliga Tekniska Högskolan i Stockholm framlägges till offentlig granskning för avläggande av teknologie licentiatexamen torsdagen den 8:e mars 2007 kl 10.30 i S40, Teknikringen 8, Kungliga Tekniska Högskolan, Valhallavägen 79, Stockholm.

©Espen Åkervik, 2007 Universitetservice US-AB, Stockholm 2007

## Feedback control of spatially evolving flows

Espen Åkervik

Linné Flow Centre, KTH Mechanics, SE-100 44 Stockholm, Sweden

### Abstract

In this thesis we apply linear feedback control to spatially evolving flows in order to minimize disturbance growth. The dynamics is assumed to be described by the linearized Navier–Stokes equations. Actuators and sensor are designed and a Kalman filtering technique is used to reconstruct the unknown flow state from noisy measurements. This reconstructed flow state is used to determine the control feedback which is applied to the Navier–Stokes equations through properly designed actuators. Since the control and estimation gains are obtained through an optimization process, and the Navier–Stokes equations typically forms a very high-dimensional system when discretized there is an interest in reducing the complexity of the equations. One possible approach is to perform Fourier decomposition along (almost) homogeneous spatial directions and another is by constructing a reduced order model by Galerkin projection on a suitable set of vectors. The first strategy is used to control the evolution of a range of instabilities in the classical family of Falkner–Skan–Cooke flows whereas the second is applied to a more complex cavity type of geometry.

**Descriptors:** Stability, control, estimation, absolute/convective instabilities, model reduction.

## Preface

This thesis deals with the application of linear feedback control to spatially evolving flows. In part 1 some background of the concepts that are assumed known when reading the papers in part 2 are presented. The papers in part II are adjusted to comply with the present thesis format for consistency, but their contents have not been altered compared to published or submitted versions, except for minor corrections. The included papers are:

**Paper 1.** Chevalier, M., Høpfner, J., Åkervik, E. and Henningson, D. S. 2007, Linear feedback control and estimation applied to instabilities in spatially developing boundary layers, *J. Fluid Mech.* under review.

**Paper 2.** Åkervik, E., Brandt, L., Henningson, D. S., Høpfner, J., Marxen, O. and Schlatter, P. 2006, Steady solutions of the Navier-Stokes equations by selective frequency damping, *Phys. Fluids* **18**, 068102 (2006).

**Paper 3.** Åkervik, E., Høpfner, J., Ehrenstein, U. and Henningson, D. S., 2007, Optimal growth, model reduction and control in a separated boundary-layer flow using global eigenmodes, *J. Fluid Mech.* accepted for publication.

**Paper 4.** Åkervik, E., Ehrenstein, U., Gallaire, F. and Henningson, D. S., Two-dimensional optimal growth in the flat plate boundary-layer flow, 2007, to be submitted.

## Contents

Abstract	iii
Preface	iv
Part 1. Summary	1
Chapter 1. Introduction	3
Chapter 2. Stability of spatially evolving flows	5
Chapter 3. Feedback Control of Flows	9
Chapter 4. Conclusions and outlook	15
Chapter 5. Summary of Papers	17
Acknowledgements	19
Bibliography	20
Part 2. Papers	23
Paper 1. Linear feedback control and estimation applied to instabilities in spatially developing boundary layers	27
Paper 2. Steady solutions of the Navier-Stokes equations by selective frequency damping	59
Paper 3. Optimal growth, model reduction and control in a separated boundary-layer flow using global eigenmodes	73
Paper 4. Two-dimensional optimal growth in the flat plate boundary-layer flow	89



**Part 1**

**Summary**



## CHAPTER 1

### Introduction

It is hard not to be fascinated by flowing fluids. The water in the pond reacts to your footsteps by turning some of your energy into beautiful waves, searching for equilibrium. The cigarette smoke enters free air peacefully suddenly to break down into chaotic patterns due to its inability to counteract inertia. The teapot never pours a straight beam until you have learnt the exact angle of tilting and how fast to tilt it. Fluids seemingly live their own lives, yet we are forced (and pleased) to interact with them everyday.

Understanding how fluid flows develops from being ordered and predictable, or so called laminar, to becoming swirling, chaotic and seemingly unpredictable, in other words turbulent, has been the occupation of transition research for over a century. The importance of obtaining knowledge on this process is substantial both from an industrial and an environmental point of view. This is because turbulence on one hand increases the drag along immersed bodies making for instance aeroplanes and boats more fuel consuming. On the other hand turbulence increases the mixing properties of the flow, making combustion more efficient.

The transition process may be divided into three stages; receptivity where disturbances enter the flow; disturbance growth where the linear mechanisms are important; and finally breakdown where non-linear processes starts to redistribute energy to smaller and smaller scales. Hydrodynamic stability deals with the second stage of this process. This is done through studying the response of the flow to small amplitude disturbances about a laminar flow either by experiments or by mathematical models. An accurate mathematical description of most encountered fluid flows are provided by the Navier–Stokes equations. If the flow responds to the disturbance by returning to its laminar state it is stable, otherwise it is unstable.

While the subject of hydrodynamic stability is to understand the disturbance growth mechanisms, i.e. providing a model of the flow, flow control aims at using this knowledge to correctly interact with it. The objective of the interaction might be to delay transition to turbulence along an aeroplane wing or it might be to promote turbulence in combustion processes. Control of fluid flows can be performed in essentially two ways; either passively or actively. The optimized shape of an aeroplane wing, the rough surface of the golf ball or the

evolutionary design of the skin of fishes are all examples of passive control. By controlling flows in this manner no energy is put into the system, there is only a cooperation with the flow. In active control on the other hand, energy is put into the system through actuators, hopefully gaining more energy than what is spent. Active control can be split into two main categories, namely open-loop and closed-loop control. The former assumes exact knowledge of the system so that the interaction with it is prescribed a priori. However if disturbances that are not accounted for in the model are present, the controller will in general fail. The latter, which is commonly called feedback control, uses information from the system in order to detect the real disturbances present, making it more robust to deviations from the assumed model.

A successful feedback control strategy is the Linear Quadratic Gaussian (LQG) synthesis, which provides a way of coupling sensors to actuators with optimality guarantees. In this setting a linear model of the system is assumed, a quadratic objective is to be minimized and random disturbances, accounting for modelling uncertainties and sensor noise, are Gaussian distributed.

Feedback controllers are run online, measuring the state and feeding back control signals to the actuators. Further the optimal control feedback law is achieved through the solution of optimization problems. Both tasks challenge the available computer hardware, since the numerical approximation of the Navier–Stokes equations yields a very high dimensional system. There is hence the need to construct reduced models that can accurately describe the connection between the sensors and actuators. A systematic way of obtaining reduced models is to perform a projection of the equations on a reduced basis.

In the following a short introduction focusing on stability for spatially evolving flows and LQG control will be given.

## CHAPTER 2

### Stability of spatially evolving flows

The flow evolution of fluids are generally described by laws governing conservation of mass, momentum and energy. If the fluid is Newtonian and compressible effects are negligible these conservation laws ends up in the non-linear incompressible Navier–Stokes equations. These equations describe the evolution of the velocities  $\mathbf{u} = [u, v, w]^T$  and pressure  $p$ . In a cartesian coordinate system  $u$ ,  $v$  and  $w$  are the streamwise, wall normal and spanwise velocity components, respectively. For small disturbances  $\mathbf{u}'$  to a base flow  $\mathbf{U}$ , a linearization is relevant, so that the evolution of the disturbances are governed by the linearized Navier–Stokes equations

$$\begin{cases} \frac{\partial \mathbf{u}'}{\partial t} = -(\mathbf{U} \cdot \nabla) \mathbf{u}' - (\mathbf{u}' \cdot \nabla) \mathbf{U} - \nabla p + \frac{1}{Re} \Delta \mathbf{u}', & \mathbf{u}'(0) = \mathbf{u}'_0, \\ \nabla \cdot \mathbf{u}' = 0. \end{cases} \quad (2.1)$$

A characteristic velocity scale  $V$  together with a typical length  $L$  and the kinematic viscosity  $\nu$  defines the non-dimensional Reynolds number  $Re = UL/\nu$ . This quantity describes the relation between inertial and viscous forces, making it the critical parameter for transition. Note that the above system can be written in state-space form as  $\dot{q} = Aq$ , where  $q$  contains the velocities and the pressure, and  $A$  is referred to as the dynamic matrix. This system has the formal solution  $q(t) = \exp(At)q_0$  for an initial condition  $q_0$ . The strategy of determining whether a flow is stable or unstable is to consider the response of the numerically approximated (2.1) to an initial condition. The classical approach to stability takes the so called normal-mode assumption, where the time dependence is assumed to be exponential,  $q(x, y, z, t) = \phi(x, y, z) \exp(-i\omega t)$ , leading to a temporal eigenvalue problem for the complex frequency  $\omega$ . If any eigenvalues have positive imaginary part the flow is unstable, otherwise it is stable. The high dimensionality of the resulting problem, however poses a great computational challenge since typically the size of the operators are of the order of  $4n_x n_y n_z$ . Increased computer capacities together with iterative Krylov-subspace methods such as the Arnoldi method (see Nayar & Ortega 1993) has made it possible to compute both two- and three-dimensional eigenmodes, both of which are commonly called global eigenmodes. A substantial simplification can be achieved if the base flow under consideration is parallel. In these situations a Fourier transformation along the homogeneous directions, that means

$q(x, y, z, t) = \phi(y) \exp(\alpha x + \beta z - i\omega t)$ , decouples the problem into a sequence of one dimensional problems, known as the Orr–Sommerfeld–Squire (OSS) equations (Orr 1907; Sommerfeld 1908; Squire 1933), parametrized by the wave numbers  $\alpha, \beta$  and the local Reynolds number. This approach is referred to as local. For slowly varying flows it is still possible to use the OSS equations as long as there is a separation of the scales, i.e. the base flow changes slowly in comparison to a typical instability wave length. In this case at each streamwise station the base flow is extended to infinity and local stability characteristics are studied. Successful theoretical findings within the normal-mode approach includes the discovery of the so called Tollmien–Schlichting (TS) waves (Tollmien 1929; Schlichting 1933) and the connection between temporal and spatial behaviour of the disturbances Gaster (1965). An improvement of the locally parallel assumption lead to the Parabolized Stability Equations (Bertolotti *et al.* 1992) that incorporated the variation of the flow into the eigenvalue problem.

The normal mode assumption provides the asymptotic behaviour of the disturbances, but there are situations where short time behaviour plays an important role. This is for instance the case when the boundary layer is subject to free-stream turbulence, leading to the formation of streaks through the “lift-up” mechanism (Landahl 1980), which may gain large amplitudes and eventually non-linearly break down. A mathematical framework able to predict the experiments was presented in Butler & Farrell (1992); Reddy & Henningson (1993); Trefethen *et al.* (1993), showing that the OSS equations supported transient growth, related to the non-normal nature of the underlying operators. For properties of non-normal operators and procedures to compute transient growth (also called optimal growth) we refer to Schmid & Henningson (2001). This modern approach to stability has converged to the formulation of the stability problem as an optimization problem, which may be solved either by singular value decomposition of the evolution operator  $\exp(At)$ , or by time-marching methods involving the adjoint system (Schmid 2007). As modern hydrodynamical stability trust less in single eigenvalues, an eigenvalue decomposition of the problem is still relevant, since it diagonalizes the system matrix  $A$ , making the expression for the evolution operator especially simple.

Spatially evolving flows display the particular feature that the instability characteristics may change throughout the domain. There can be regions where the flow is stable, convectively unstable or absolutely unstable. In a convectively unstable region the disturbances are swept downstream with the flow while growing. In this case the disturbances disappear in absence of external forcing so that the flow might be seen as a noise amplifier. The boundary layer flows studied in Paper 1 and 4 are typical examples of convectively unstable configurations. Whenever the base flow satisfies certain conditions, for example if there is a sufficiently large reverse flow in a separation bubble, the flow may become absolutely unstable, characterized by disturbances growing both upstream and downstream of the origin of generation, so that the flow itself will

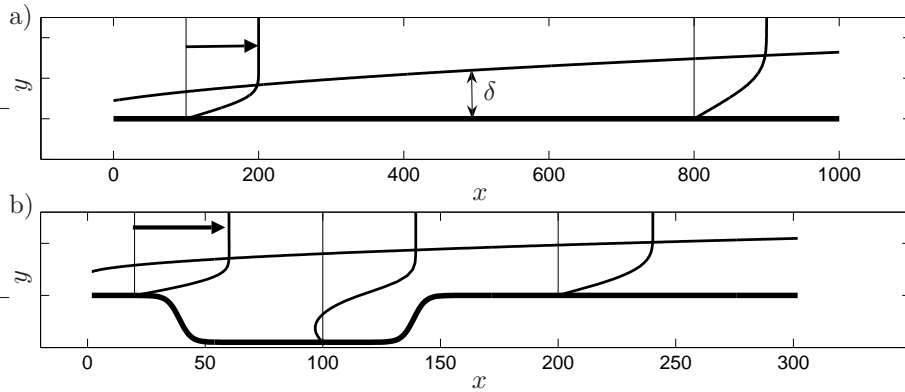


FIGURE 2.1. Sketches of spatially developing flows, with inflow at the left. a) Flat plate boundary layer flow; the flow is slowly evolving with the boundary layer thickness  $\delta$  increasing downstream. b) The cavity flow; in the front and back of the cavity there is boundary layer flow, whereas in the cavity there is reversed flow.

sustain the instability growth. Examples of globally unstable configurations are presented in Paper 2 and 3.

In the framework of local stability theory the procedure to judge if a spatially evolving flow is convectively or absolutely unstable is quite intricate and involves integration in the complex frequency- and wave-number space and the use of the pinching criterion (Huerre & Monkewitz 1990). However by considering the full equation, i.e. by computing global eigenmodes, the two regimes are easily distinguished; if any eigenvalues have positive imaginary part the flow is absolutely unstable, otherwise the flow is either stable or convectively unstable. If the transient growth analysis yields energy growth for any times the flow is convectively unstable, otherwise it is stable. The convectively unstable behaviour is in other words connected to the non-normality of the operator, more specifically the streamwise non-normality (Cossu & Chomaz 1997; Schmid & Henningson 2002; Ehrenstein & Gallaire 2005).

### 2.1. An example on convective and absolute instability

As an example on how convectively unstable and absolutely unstable flows are distinguished by the use of two-dimensional global eigenmodes we consider the flat plate boundary layer flow with inflow Reynolds number  $Re = 1000$  based on the inflow displacement thickness (sketched in figure 2.1a)) and a cavity flow with inflow Reynolds number  $Re = 350$ . In both cases the flow is from left to right. From figure 2.1b) one can see that the cavity creates a region of reversed flow. Computed global eigenvalues and the result of optimal growth analysis

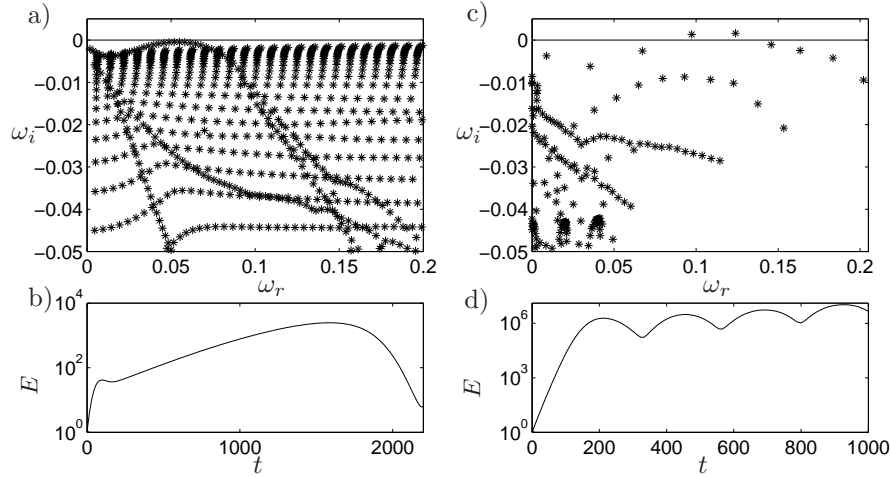


FIGURE 2.2. a) and c) Global eigenvalues. b) and d) Potential for energy growth due to optimal initial condition. a) The convectively unstable flat plate boundary layer flow has stable eigenvalues, but the non-normality leads to transient energy growth as shown in b), indicating convective instability. c) Spectra of the absolutely unstable cavity flow, where there are two unstable eigenvalues indicating absolute instability. d) There is possibility for large growth initially followed by an oscillating cycle.

for both cases are shown in figure 2.2. The global eigenvalues obtained for the flat plate boundary displayed in figure 2.2a) are all stable, but the energy evolution from transient growth analysis (see figure 2.2b)) shows that there is possibility for growth. This means that the flow is convectively unstable, i.e. disturbances are swept downstream while growing, eventually leaving the computational domain. For a more detailed description on this flow case we refer to Paper 4 in this thesis. On the other hand, in figure 2.2c) the global eigenvalues for the cavity flow show that there are two unstable eigenvalues, hence the flow is globally unstable. Following the modern approach to stability, we still compute the optimal growth associated with the operator. Indeed, as seen in figure 2.2d), the possibility for short time growth is large, and the asymptotic behaviour of the system is associated with the competition of the two unstable eigenmodes. A thorough description of this flow case and its non-normal behaviour is given in Paper 3.

## CHAPTER 3

# Feedback Control of Flows

Flow control in its widest sense refers to any mechanism that modifies the behaviour of the flow, but in the present context we only consider measurement feedback control in the framework of the Linear-Quadratic-Gaussian (LQG) synthesis.

### 3.1. Selected references

Regarding previous work on feedback control of flow systems extensive reviews are given in Gad-el-Hak (1996); Bewley (2001); Kim (2003). In the recent review by Kim & Bewley (2007) the authors summarize the ingredients of the linear systems approach to controlling fluid mechanics problems. A selected list of publications on linear feedback control applied to parallel laminar and turbulent flows includes Joshi *et al.* (1997); Bewley & Liu (1998); Keun *et al.* (2001); Högberg *et al.* (2003). Linear feedback control has also been applied to spatially developing flows in Högberg & Henningson (2002); Cathalifaud & Bewley (2004*a,b*). The justification of applying linear feedback control to inherently non-linear processes such as the evolution of fluid flows is threefold; first of all the transition process consists of a linear stage, where small disturbances grow until non-linear breakdown occurs (Schmid & Henningson 2001), secondly linear processes are important to sustain turbulence in wall-bounded turbulent flows (Kim & Lim 2000), thirdly stochastic disturbance models can be introduced in the linearized Navier–Stokes equations mimicking flow statistics of full DNS (Jovanović & Bamieh 2001).

### 3.2. LQG control of the Navier–Stokes equations

Assume that the state equation is the non-linear Navier–Stokes equations

$$\begin{aligned} \dot{q} &= NS(q) + B_2 u \\ y &= Cq, \end{aligned} \tag{3.2}$$

where  $q$  is the state, i.e. velocities and pressure,  $NS$  is the right hand side of the non-linear Navier–Stokes operator and  $u$  are the inputs, or actuator signals, which allow us to manipulate the state through the operator  $B_2$ . Assume that from the above system only outputs, or measurements,  $y$  extracted through the operator  $C$  are available. In order to construct a controller for the above

system we will linearize it, so that the dynamics is similar to (2.1), but with the possibility to alter its dynamics. Our concern is now to find an optimal mapping from the output to the input so that kinetic energy of disturbances are minimized. A direct formulation of that problem results in a sequence of coupled non-linear equations, and there are no robustness guaranties to the resulting controller (see e.g. Lewis & Syrmos 1995). On the other hand by splitting the problem in two, where an optimal controller is built using full knowledge of the state (Linear Quadratic Regulator), but replacing that state with an estimated state reconstructed from the measurements based on a Kalman filter results in a controller with certain desirable properties. For instance if the full information controller and the Kalman filter are both stable, then the resulting controller is also stable, as guaranteed by the separation principle. This is at the heart of the LQG controller.

To this end let the first step be to reconstruct the state from the measurements. A linearization of (3.2) and the introduction of random Gaussian distributed disturbances to account for modelling uncertainties and measurement noise yields the following system

$$\begin{cases} \dot{q} = Aq + B_1w + B_2u, & q(0) = q_0 \\ y = Cq + g, \end{cases} \quad (3.3)$$

where  $w$ ,  $g$  and  $q_0$  are uncorrelated and known through their covariances. This implies that the state also becomes stochastic and known through its covariance  $P = E\{q^*q\}$ , the evolution of which being governed by a Lyapunov equation. The process of estimating a linear system with noisy and limited amount of information is an optimal filtering problem (Kailath *et al.* 1999). Now let the state equation itself serve as a time-domain filter (this is the Kalman filter)

$$\begin{cases} \dot{\hat{q}} = A\hat{q} + B_2u + L(y - \hat{y}), & \hat{q}(0) = 0 \\ \hat{y} = C\hat{q}, \end{cases} \quad (3.4)$$

where  $\hat{q}$  is the estimated state. Note the absence of disturbances and the presence of a forcing term  $L(y - \hat{y})$  which disappears when the difference in the measurements are zero. The error involved in the process is defined as  $\tilde{q} = q - \hat{q}$  with corresponding covariance  $\tilde{P}$ . The task is now to find the optimal forcing gain  $L$  that minimizes the quadratic measure  $\mathcal{J}_e = \text{trace}(\tilde{P})$  in the infinite horizon subject to the Lyapunov equation for the estimation error covariance  $\tilde{P}$ . This optimization problem can be solved by a Lagrange multiplier technique leading to an algebraic Riccati equation for  $\tilde{P}$  from which the optimal gain  $L$  can be extracted. The optimal gain  $L$  is now designed such as to drive the estimated state  $\hat{q}$  towards the unknown state  $q$  based on the measurement difference  $y - \hat{y}$ . A discussion on how to model the stochastic disturbances for fluid flows can be found in Høpfner *et al.* (2005); Chevalier *et al.* (2005).

When designing an optimal full information controller we take a deterministic approach, where we assume that full state information is available and

given by the equation  $\dot{q} = (A - B_2K)q$ . The optimal control gain  $K$  is designed such that  $u = Kq$  minimizes the quadratic measure of a weighted sum of the control effort and the flow kinetic energy in the infinite horizon

$$\mathcal{J}_c = \int_0^\infty q^H Q q + u^H R u \, dt, \quad Q, R > 0. \quad (3.5)$$

Minimization of this expression can also be achieved through a Lagrange multiplier technique where the constraint is the state equation  $\dot{q} = (A - B_2K)q$  and the optimal gain is obtained through the solution of an algebraic Riccati equation. As stated earlier the separation principle guarantees that the optimal measurement feedback control is given by

$$u(t) = K\hat{q}(t), \quad (3.6)$$

where  $\hat{q}$  is indeed the state estimate provided by the Kalman filter. Note that in general the cost functions  $\mathcal{J}_c$  and  $\mathcal{J}_e$  can be time varying functions and in this case the gains  $K$  and  $L$  become time dependent and their solution is governed by differential Riccati equations (see e.g. Kailath *et al.* 1999).

Applying the optimal controller to the Navier-Stokes equations amounts to solving the system

$$\begin{aligned} \dot{q} &= NS(q) + B_2u, & y &= Cq, \\ \dot{\hat{q}} &= (A + B_2K + LC)\hat{q} - Ly, & u &= K\hat{q}. \end{aligned} \quad (3.7)$$

The evolution of the flow state  $q$  is updated for example by means of DNS. At every time step measurements  $y$  are extracted, driving the estimated state  $\hat{q}$ . The estimated state is updated online by any suitable time-integration procedure, feeding back at every time step control signals  $u$  to the DNS. In general the dimension of the state  $\hat{q}$  is as large as the original state, and has to be solved by means of DNS, so that memory and time requirements are doubled. This of course has implications when it comes to realizability of the controller for example in experiments.

A reduced model can be built by projection of (3.3) on a suitable set of vectors followed by truncation based on certain criteria. These criteria are commonly given by the controllability and observability grammians. The observability grammian can loosely be said to describe to what extent a state can be observed by the sensor  $C$  and likewise the controllability grammian states to what extent a state can be reached by the actuator  $B_2$ .

The global eigenmodes  $\phi_l$  of the linearized Navier-Stokes equations form such a suitable basis for projection. We will here briefly show to how perform the projection. Let the state be expanded in terms of the sum of the eigenmodes  $q = \sum_l \kappa_l \phi_l$ , where  $\kappa_l$  are the expansion coefficients of the sum. Properly normalized adjoint eigenfunctions  $\phi_k^+$  satisfy the bi-orthogonality condition  $\langle \phi_l, \phi_k^+ \rangle = \delta_{lk}$ . The inner product can be with respect to any relevant norm, for example the energy norm or the  $\mathbf{L}_2$  norm. Now expand the state

in terms of the eigenmodes and perform the inner product with the adjoint eigenfunctions

$$\begin{aligned} \langle \sum_l \phi_l \kappa_l, \phi_k^+ \rangle &= \langle A \sum_l \phi_l \kappa_l, \phi_k^+ \rangle + \langle B u, \phi_k^+ \rangle \\ \Rightarrow \sum_l \underbrace{\langle \phi_l, \phi_k^+ \rangle}_{\delta_{lk}} \kappa_l &= \sum_l \underbrace{\langle A \phi_l, \phi_k^+ \rangle}_{\delta_{lk} \lambda_k} \kappa_l + \underbrace{\langle B, \phi_k^+ \rangle}_{B_k^M} u. \end{aligned} \quad (3.8)$$

For the output the adjoint modes are not needed, instead only an expansion is performed

$$y = C \sum_l \phi_l \kappa_l = \sum_l \underbrace{C \phi_l}_{C_l^M} \kappa_l. \quad (3.9)$$

Gathering all the components yields the following system

$$\begin{aligned} \dot{k} &= A^M k + B^M u \\ y &= C^M k, \end{aligned} \quad (3.10)$$

where  $k = [\kappa_1, \kappa_2, \dots, \kappa_m]^T$  is the vector of expansion coefficients. A truncation can now be done based on the magnitude of the projected input operator  $B_2^M$ , output operator  $C^M$  and the damping rate  $\lambda_{l,i}$ . The projection of the term  $B_1$  in (3.3) follows the same procedure as for  $B_2$ .

Another possible basis for projection is the Balanced Truncation modes (Moore 1981) which are constructed so as to make the observability and controllability grammians equal and diagonal in the projected basis. A truncation can in this case be done based on the magnitude of any of the two projected grammians. The drawback of such an approach is that the balancing vectors are obtained through the solution of two Lyapunov equations, a task which becomes computationally heavy even for moderate dimensions of the discretized Navier–Stokes operators. Rowley (2005) discussed a computationally tractable approach to obtaining the balancing vectors, based on time-marching algorithms.

### 3.3. Examples

In paper 1 we compute control and estimation gains based on the locally parallel assumption. Here we consider the control of the two-dimensional forced TS-waves. This means that the online system which is updated is the full system with dimensions  $\approx 10^5$ , i.e. the OSS equations for every wave-number present in the DNS. The thin line in figure 3.1 shows the streamwise energy evolution of the TS wave in the convectively unstable flat plate boundary layer flow with inflow Reynolds number  $Re = 1150$  taken from DNS. A sketch of a similar set up is given in figure 2.1a). The skin-friction and pressure is measured in the region  $x \in [0, 100]$  and wall blowing and suction is applied continuously in  $x \in [100, 250]$ . The thick line in figure 3.1 shows that the controller diminishes

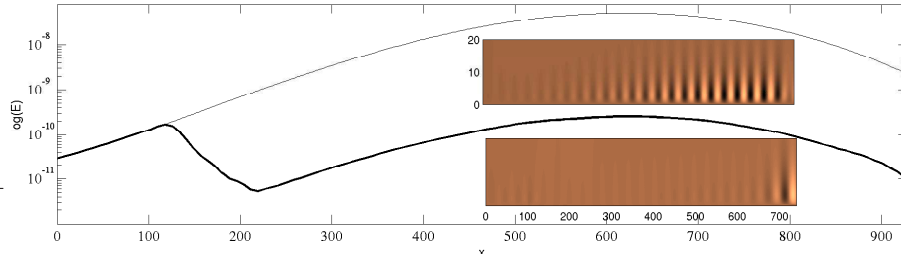


FIGURE 3.1. Streamwise energy evolution of TS waves for the convectively unstable flat plate boundary layer flow, thin line shows uncontrolled whereas thick shows controlled. Control is applied continuously in a strip in  $x \in [100, 250]$ . Inserted are snapshots of the wall normal velocity. The top frame shows a fully developed TS wave and bottom shows that the controller have diminished the disturbances so that the TS wave is left to propagate out of the domain.

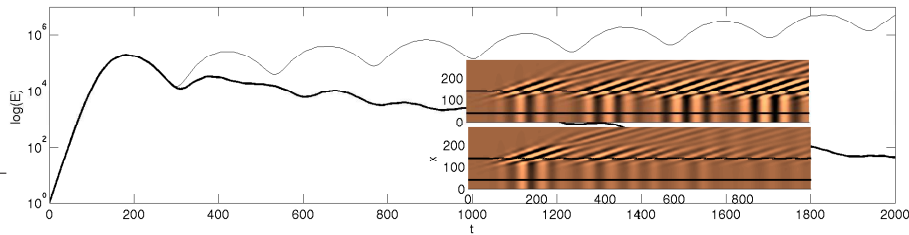


FIGURE 3.2. Time evolution of total energy in a cavity flow subject to self-sustained oscillations. Thick line shows uncontrolled whereas thin line shows controlled. Inserted frames show the  $x/t$  evolution of the pressure at  $y = 10$  for the uncontrolled case (top) and controlled case (bottom). The controller counteracts the regeneration of the disturbances after reflection.

the TS wave. The inserted frames show snapshots of the vertical velocity component of the fully developed TS wave (top) and at a later time when the controller has diminished the disturbances so that the TS wave is left to propagate out of the computational box (bottom).

In paper 2 we use a reduced model obtained by projection on the two-dimensional global eigenmodes of the linearized Navier–Stokes equations, and in this case the online system to be updated consists only of the expansion coefficients of the eigenmode expansion. We found that by using a reduced

system consisting only of 4 expansion coefficients we were able to control the system satisfactorily. For comparison the full DNS system has  $\approx 10^6$  degrees of freedom. Figure 3.2 shows the time history of the energy taken from DNS of the cavity flow, where the thin line shows the uncontrolled case and the thick shows the controlled. A sketch of the geometry is given in figure 2.1b). The inserted frames trace the pressure at  $y = 10$  in time and in streamwise direction. From the upper frame one can see that initially there is a wavepacket propagating across the cavity followed by pressure reflection and regeneration at the start of the cavity. The global instability mechanism consists of the wavepacket gaining more energy while propagating across the cavity than what is lost in the reflection and regeneration. The result is an oscillating cycle. A sensor measures skin friction at the downstream cavity lip and a volume forcing actuator (acting on the wall normal velocity) is placed at the upstream cavity lip. The thick line shows that the exponential growth is turned into exponential decay. The lower inserted frame shows that regeneration is counteracted and the pressure oscillations decay.

## CHAPTER 4

### Conclusions and outlook

This thesis builds on the work started by Markus Högberg, and continued by Mattias Chevalier and Jérôme Høpffner. During their studies several problems related to active flow control were solved. First the full information control required a formulation of the fluid problem in a form that was compatible with the state space representation common to control theory. Also applications of the full information controller to spatially evolving flows were performed. In addition appropriate stochastic models for external disturbances and sensor noise were developed, resulting in a well performing estimator.

In Paper 1 the LQG controller was successfully applied to a range of spatially evolving flows with optimal control and estimation gains computed based on the OSS equations, i.e. under the locally parallel assumption. There are some drawbacks within this approach. First the actuators and sensors are assumed to be continuously distributed along the walls so that a spatial cut-off filter has to be applied to both the measurement and actuation. Secondly the size of the online controller becomes as large as the original problem (in the sense of DNS discretization). Thirdly it can only be applied when the base flow under consideration is slowly varying.

By using global eigenmodes as building blocks for a reduced model all of these problems are circumvented. The computation of the global eigenmodes is a computationally challenging task, but once the modes are computed for a given flow configuration they serve as a projection basis for building a reduced order model both in view of stability investigation and control. The cavity geometry in Paper 3 can be seen as a model problem where self-sustained oscillations occur and where it is not possible to use local analysis due to the strongly non-parallel base flow. An issue related to the computation of eigenmodes was how to obtain a steady state base flow in which to linearize about. Since self-sustained oscillations are present, any numerical noise will grow from background making it impossible to compute a steady state with standard time marching methods. A solution to this problem is dealt with in Paper 2, where a filtering technique is introduced. In Paper 3 the focus is partly on building a controller, partly on showing that global eigenmodes can describe the relevant dynamics of the flow. Due to the non-normality of the underlying operator, the computed eigenmodes were sensitive to numerical

errors and required high resolution. This sensitivity was however mostly seen in loss of accuracy for the location of eigenvalues in the complex plane; the mechanism of wavepacket propagation followed by pressure reflections obtained through optimally summing the non-normal modes proved robust and in close agreement with DNS, even at lower resolution. We also learned that many more degrees of freedom were needed in fully describing the dynamics of the flow than in controlling it.

The use of global eigenmodes for highly non-parallel flows has been established, but there are issues concerning the high degree of non-normality inherent in the operator. Therefore it is also interesting to establish their relevance for slightly non-parallel configurations, where in fact streamwise non-normality increases. In Paper 4 an almost parallel flat plate boundary layer flow is studied. It is here shown that the optimal sum of global eigenmodes can bring out the important dynamics of the flow, however a large number of eigenmodes are needed for converged results. The optimal initial condition in this configuration turned out to be a localized upstream tilted structure that through the Orr mechanism gains energy before starting a Tollmien-Schlichting type of wavepacket. The ability of the eigenmodes to describe the relevant dynamics of the flow is confirmed by the close match between the eigenmode system and the DNS in terms of time integration.

We thus see promising perspectives of using global eigenmodes as a projection basis for model reduction. The natural extension of the work presented in this thesis is to construct a reduced order controller for a range of flows, capable of controlling both two and three-dimensional disturbances. The first in line is the slightly non-parallel flat plate boundary-layer flow which might serve as a lower limit in geometrical complexity but which has a wide range of frequencies and instability mechanisms. Open questions related to building reduced models for control by global eigenmodes are; how many actuators do we need? How well can we measure the flow using localized sensors? Can the eigenmodes handle three dimensional disturbances related to the lift-up mechanism? Can one represent wall blowing and suction with the eigenmodes based on homogeneous boundary conditions?

Balanced truncation modes, which are constructed based on a certain set of actuators and sensor, may turn out to be robust when it comes to the latter question. The drawback of balanced truncation is that their computation is based on the solution of Lyapunov equations. The direct computation of these equations are computationally heavy, but time-marching algorithms may turn out to yield it a computationally attractive alternative. The design of reduced models for control in fluid mechanics applications are at an early stage, but by laying the bricks thoroughly a lot can be achieved in the years to come.

## CHAPTER 5

### Summary of Papers

#### **Paper 1**

*Linear feedback control and estimation applied to instabilities in spatially developing boundary layers.*

MATTIAS CHEVALIER, JÉRÔME HËPFFNER, ESPEN ÅKERVIK, DAN HENNINGSON.

The method to build covariance of the stochastic sources of excitation is applied to control and estimation in spatially developing boundary layer flow. Several cases of fundamental interest are considered: unstable Tollmien–Schlichting waves, unstable cross-flow vortices, transient growth and streaks. This paper is the follow up of Högberg & Henningson (2002) that focused on the control part.

The writing of the paper was done by MC, with feedback from JH, EÅ and DH. The computation of the control and estimation gains were performed by MC and EÅ with a computer program developed by JH and Marcus Högberg. The direct numerical simulation was performed by MC and EÅ using a code originally developed at the Department of Mechanics.

*J. Fluid Mech., submitted.*

#### **Paper 2**

*Steady solutions of the Navier–Stokes equations by selective frequency damping.*

ESPEN ÅKERVIK, LUCA BRANDT, DAN HENNINGSON, JÉRÔME HËPFFNER, OLAF MARXEN, PHILIP SCHLATTER.

A highly accurate numerical description of the base flow is necessary for stability analysis. Previously, for cases without symmetries, the Newton method was used to solve for steady solutions of the Navier–Stokes equations. We propose a method based on selective frequency damping, easy to implement in existing direct numerical simulation codes to stabilize steady states solution, and thus reach them by time marching. The method was used in paper 4 for the computation of the globally unstable base flow in the separated boundary layer flow.

The writing of the paper was done by LB and PS, with feedback from all authors. The computations of the cavity flow was done by EÅ, and by OM

for the recirculation bubble. The analysis of the stabilization and choice of the design parameters was done by JH.

*Phys. Fluids* **18**, 068102 (2006).

### Paper 3

*Optimal growth, model reduction and control in a separated boundary-layer flow using global eigenmodes* ESPEN ÅKERVIK, JÉRÔME HEPPFNER, UWE EHRENSTEIN, DAN HENNINGSON.

This paper deals with optimal growth and control of a globally unstable cavity flow. Optimal growth analysis yields an upstream located initial wavepacket. This wavepacket propagates through the shear layer in the cavity and pressure reflections regenerate the disturbances upstream. A reduced order model for control based on as few as 4 eigenmodes is built, and the LQG controller is run in parallel to the DNS at a low computational cost. The satisfactory performance of the controller, combined with the low online computational effort provides promising perspectives of using reduced order models based on global eigenmodes for fluid flows.

The writing of the paper was done by in collaboration by JH, UE and EÅ, with feedback from DH. The controller optimizations were done by JH and EÅ with a code developed by JH. The eigenmode computations were performed by EÅ with a code developed by UE. Implementations and computations of the steady baseflow and the controller was done by EÅ with a direct numerical simulation code developed by Matthieu Marquillie and UE.

*J. Fluid Mech.*, accepted for publication.

### Paper 4.

*Two-dimensional optimal growth in the flat plate boundary-layer flow.*

ESPEN ÅKERVIK, UWE EHRENSTEIN, FRANÇOIS GALLAIRE AND DAN S. HENNINGSON

This paper deals with the use of global eigenmodes to compute optimal growth and optimal forcing in the flat plate boundary layer flow. A convergence in the number of eigenmodes needed in describing the optimal initial condition is obtained. The Orr mechanism is revisited and it is shown that this mechanism is not separated from the Tollmien–Schlichting mechanism, in fact they cooperate. The optimal forcing structures are similar to the optimal initial condition but at the same time following the neutral curve.

The writing of the paper was done by EÅ in collaboration with UE and FG with feedback from DH. The computation of the eigenmodes were done by EÅ and UE. The computation of the optimal initial condition was done by EÅ and the optimal forcing by EÅ and UE. Direct numerical simulations were performed by UE using a code developed by Matthieu Marquillie and UE.

*To be submitted.*

## Acknowledgements

I would like to thank my supervisors Dan S. Henningson and Luca Brandt for their persistent patience and enthusiasm. Many thanks also to professor Uwe Ehrenstein for the close cooperation and social input during the last two years in Stockholm, Nice and Marseilles. Thanks to Jérôme Hœpffner and to Mattias Chevalier for the collaboration that has enabled me to write this thesis. Thanks to Philipp Schlatter and François Gallaire for sharing their knowledge with me. Others to thank are group members and collaborators Ori Levin, Erik Stålberg, Astrid Herbst, Carl-Gustav Unckel, Martin Byström, Shervin Bagheri, Lars-Uve Schrader, Olaf Marxen and Ardeshir Hanifi. Thanks to Daniel Ahlman, Gunnar Tibert, Carl-Ola Danielsson, Linus Marstorp, Olof Grundestam, Hanno Essén and all the others at Mechanics for making for making social life here at the department enjoyable.

I gratefully acknowledge the financial support from The Swedish Research Council (VR).

*Takk Ragna min elskede for at du forstår meg som person*

## References

- BERTOLOTTI, F. P., HERBERT, T. & SPALART, P. R. 1992 Linear and nonlinear stability of the Blasius boundary layer. *J. Fluid Mech.* **242**, 441–474.
- BEWLEY, T. R. 2001 Flow control: new challenges for a new renaissance. *Progress in Aerospace Sciences* **37**, 21–58.
- BEWLEY, T. R. & LIU, S. 1998 Optimal and robust control and estimation of linear paths to transition. *J. Fluid Mech.* **365**, 305–349.
- BUTLER, K. M. & FARRELL, B. F. 1992 Three-dimensional optimal perturbations in viscous shear flow. *Phys. Fluids A* **4**, 1637–1650.
- CATHALIFAUD, P. & BEWLEY, T. 2004a A noncausal framework for model-based feedback control of spatially-developing perturbations in boundary-layer flow systems. part 1: Formulation. *Systems and Control Letters* **51**, 1–13.
- CATHALIFAUD, P. & BEWLEY, T. 2004b A noncausal framework for model-based feedback control of spatially-developing perturbations in boundary-layer flow systems. part 2: Numerical simulations using state feedback. *Systems and Control Letters* **51**, 15–22.
- CHEVALIER, M., HEPFFNER, J., BEWLEY, T. R. & HENNINGSON, D. S. 2006 State estimation in wall-bounded flow systems. Part II: Turbulent flows. *J. Fluid Mech.* **552**, 167–187.
- COSSU, C. & CHOMAZ, J. 1997 Global measures of local convective instability. *Phys. Rev. Lett.* **77**, 4387–90.
- EHRENSTEIN, U. & GALLAIRE, F. 2005 On two-dimensional temporal modes in spatially evolving open flows: the flat-plate boundary layer. *J. Fluid Mech.* **536**, 209–218.
- GAD-EL-HAK, M. 1996 Modern developments in flow control. *Appl. Mech. Rev.* **49**, 364–379.
- GASTER, M. 1965 On the generation of spatially growing waves in a boundary layer. *J. Fluid Mech.* **22**, 433–441.
- HEPFFNER, J., CHEVALIER, M., BEWLEY, T. R. & HENNINGSON, D. S. 2005 State estimation in wall-bounded flow systems. Part I: Laminar flows. *J. Fluid Mech.* **543**, 263–294.
- HÖGBERG, M., BEWLEY, T. R. & HENNINGSON, D. S. 2003 Linear feedback control and estimation of transition in plane channel flow. *J. Fluid Mech.* **481**, 149–175.

- HÖGBERG, M. & HENNINGSON, D. S. 2002 Linear optimal control applied to instabilities in spatially developing boundary layers. *J. Fluid Mech.* **470**, 151–179.
- HUERRE, P. & MONKEWITZ, P. 1990 Local and global instabilities in spatially developing flows. *Annu. Rev. Fluid Mech.* **22**, 473–537.
- JOSHI, S. S., SPEYER, J. L. & KIM, J. 1997 A systems theory approach to the feedback stabilization of infinitesimal and finite-amplitude disturbances in plane Poiseuille flow. *J. Fluid Mech.* **332**, 157–184.
- JOVANOVIĆ, M. & BAMIEH, B. 2001 Modeling flow statistics using the linearized Navier–Stokes equations. *Proc. 40'th IEEE Conference on decision and control, FL*.
- KAILATH, T., SAYED, A. H. & HASSIBI, B. 1999 *Linear Estimation*. Prentice-Hall, Inc.
- KEUN, L. H., CORTELEZZI, L., SPEYER, J. L. & KIM, J. 2001 Application of reduced-order controller to turbulent flows for drag reduction. *Phys. Fluids* **13** (5), 1321–1330.
- KIM, J. 2003 Control of turbulent boundary layers. *Phys. Fluids* **15**, 1093–1105.
- KIM, J. & BEWLEY, T. R. 2007 A linear systems approach to flow control. *Annu. Rev. Fluid Mech.* **39**, 383–417.
- KIM, J. & LIM, J. 2000 A linear process in wall-bounded turbulent shear flows. *Phys. Fluids* **12** (8), 1885–1888.
- LANDAHL, M. T. 1980 A note on an algebraic instability of inviscid parallel shear flows. *J. Fluid Mech.* **98**, 1–34.
- LEWIS, F. L. & SYRMOS, V. L. 1995 *Optimal control*. Wiley-Interscience.
- MOORE, B. C. 1981 Principal component analysis in linear systems: controllability, observability and model reduction. *IEEE trans. on automatic control* **AC-26**, 17.
- NAYAR, M. & ORTEGA, U. 1993 Computation of selected eigenvalues of generalized eigenvalue problems. *J. Comput. Phys.* **108**, 8–14.
- ORR, W. M. F. 1907 The stability or instability of the steady motions of a perfect liquid and of a viscous liquid. Part I: A perfect liquid. Part II: A viscous liquid. *Proc. R. Irish Acad. A* **27**, 9–138.
- REDDY, S. C. & HENNINGSON, D. S. 1993 Energy growth in viscous channel flows. *J. Fluid Mech.* **252**, 209–238.
- ROWLEY, C. R. 2005 Model reduction for fluids, using balanced proper orthogonal decomposition. *Int. J. Bifurcation and Chaos* **15**, 997–1013.
- SCHLICHTING, H. 1933 Berechnung der Anfachung kleiner Störungen bei der Plattenströmung. *ZAMM* **13**, 171–174.
- SCHMID, P. J. 2007 Nonmodal stability theory. *Annu. Rev. Fluid Mech.* **39**, 129–162.
- SCHMID, P. J. & HENNINGSON, D. S. 2001 *Stability and transition in shear flows*. Springer.
- SCHMID, P. J. & HENNINGSON, D. S. 2002 On the stability of a falling liquid curtain. *J. Fluid Mech.* **463**, 163–171.
- SOMMERFELD, A. 1908 Ein Beitrag zur hydrodynamischen Erklärung der turbulenten Flüssigkeitsbewegungen. In *Atti del 4 Congr. Internat. dei Mat. III*, pp. 116–124. Roma.

22 REFERENCES

- SQUIRE, H. B. 1933 On the stability for three-dimensional disturbances of viscous fluid flow between parallel walls. *Proc. Roy. Soc. Lond. Ser. A* **142**, 621–628.
- TOLLMIEH, W. 1929 Über die entstehung der turbulenz. In *Nachr. Ges. Wiss. Göttingen*. Nachr. Ges. Wiss Göttingen, 21–44, (English translation NACA TM 609, 1931).
- TREFETHEN, L. N., TREFETHEN, A. E., REDDY, S. C. & DRISCILL, T. A. 1993 Hydrodynamic stability without eigenvalues. *Science* **261**, 578–584.

**Part 2**

**Papers**



# Paper 1



# Linear feedback control and estimation applied to instabilities in spatially developing boundary layers

By **Mattias Chevalier**<sup>1,2</sup>, **Jérôme Hoëpfner**<sup>3</sup>, **Espen Åkervik**<sup>2</sup>  
and **Dan S. Henningson**<sup>2</sup>

<sup>1</sup>The Swedish Defence Research Agency (FOI), SE-164 90, Stockholm, Sweden

<sup>2</sup>Linné Flow Centre, KTH Mechanics, SE-100 44, Stockholm, Sweden

<sup>3</sup>IRPHÉ, Université de Provence, F-13384 Marseille Cedex 13, France

This paper presents the application of feedback control to spatially developing boundary layers. It is the natural follow-up of Högberg & Henningson (2002), where exact knowledge of the entire flow state was assumed for the control. We apply recent developments of stochastic models for the external sources of disturbances that allow the efficient use of several wall measurement for estimation of the flow evolution: the two components of the skin-friction and the pressure fluctuation at the wall. Perturbations to base flow profiles of the family of Falkner–Skan–Cooke boundary layers are estimated by use of wall measurements. The estimated state is in turn fed back for control in order to reduce the kinetic energy of the perturbations. The control actuation is achieved by means of unsteady blowing and suction at the wall. Flow perturbations are generated at the upstream region in the computational box and are propagating in the boundary layer. Measurements are extracted downstream over a thin strip, followed by a second thin strip where the actuation is performed. It is shown that flow disturbances can be efficiently estimated and controlled in spatially evolving boundary layers for a wide range of base flows and disturbances.

---

## 1. Introduction

There is much to be gained in the application of control to fluid mechanical systems, the most widely recognized and targeted aim being the reduction of skin friction drag on airplane wings. Flow control is a growing field and much research effort is spent in both fundamental understanding and direct application of control methods. For a review see e.g. Bewley (2001) and Högberg & Henningson (2002).

Linear control theory gives powerful model-based tools for application of control to fluid systems provided the system at hand can be well described

by a linear dynamic model. The theory of Linear–Quadratic–Gaussian control (LQG) is one of the major achievements in the field of control theory. It gives a methodology to compute the optimal, measurement based, control when the dynamic model is linear, the objective is quadratic, and the external sources of excitations are stochastic. This theory is applied to boundary layer control in the present work.

Feedback control design can be conceptually and technically decomposed into two subproblems. The first subproblem is to estimate the flow state from noisy wall measurements. In our case, the state is the flow perturbation about the known base flow profile. The estimator is a simulation of the dynamic system that is run in parallel to the flow. Its state is forced by a feedback of the measurements in order to converge to the real flow state. The estimated state is in turn used for feedback control of the flow which constitutes the second subproblem. The closed loop system with estimation and control is commonly referred to as measurement feedback control or compensator.

This paper is the necessary follow-up of Högberg & Henningson (2002) in which full information control was applied to spatially developing flows. The use of stochastic models for external sources of excitation was introduced in Hæpffner *et al.* (2005) and Chevalier *et al.* (2006), which allows computation of well-behaved estimation feedback kernels for three wall measurements: the two components of the skin-friction and the wall pressure. Each of these three measurements provide the estimator with additional information on the instantaneous flow state. This variety of measurements is instrumental when complex flows are targeted. This improvement of the estimation thus makes it possible to apply the full theory of feedback control to complex flow cases such as the transitional scenarios presented in this paper. For this reason, we have systematically reconsidered the flow cases of Högberg & Henningson (2002), where exact knowledge of the entire flow state was assumed, and applied measurement-feedback control, where the estimated flow state is used for control. We compared the performance between the full information control of Högberg & Henningson (2002) and the present estimation based control, and found satisfactory performance.

One of the major limitations to the application of control to spatially distributed systems (system in space and time, usually described by partial differential equations) is the realization of the sensing and actuation that would handle relatively fast events as well as small scales of fluid motion. In addition, control over physical surfaces typically requires dense arrays of sensors and actuators. Recent development in MEMS technology and related research may lead to solutions of this problem. For application of MEMS technology to flow control see e.g. Yoshino *et al.* (2003).

Several recent investigations have pursued the application of LQG-type feedback control to wall-bounded flow systems. A recent overview of this

progress is given in Kim (2003). Högberg *et al.* (2003*a*) demonstrated the localization of the feedback kernels. This property allows a local application of the control, i.e. only the local properties of the system (dynamics, disturbance sources and measurement information) are necessary for control. The efficiency of the control scheme we use here was illustrated in Högberg *et al.* (2003*b*), where relaminarization of a fully developed turbulent flow was achieved. In Hoepffner *et al.* (2005) and Chevalier *et al.* (2006), the focus was on the estimation performance. By introducing a relevant model for the external source of disturbance, it was possible to improve the estimation performance on both transitional and turbulent flows.

The procedures of control design are based on the manipulations of a linear dynamic model for the flow system, which is typically of large order. In the case of spatially invariant systems, i.e. system for which the dynamics is independent of some spatial coordinates, the problem can be decoupled in a parameterized family of smaller systems. In our case, we assume spatial homogeneity over the two horizontal directions. After Fourier transforming, this allows to design and tune the controller and estimator for individual wavenumber pairs.

In a spatially developing flow like the boundary layer, this procedure can still be used, even though the spatial invariance in the streamwise direction is lost. Indeed, the localization of the control and estimation kernels ensures that the feedback is local, so that the flow can be assumed to be locally parallel. In Högberg & Henningson (2002), the actuation was successfully applied over a strip parallel to the leading edge in Falkner–Skan–Cooke (FSC) boundary layers, and the control feedback law was computed based upon the local Reynolds number. In Högberg *et al.* (2003*c*), a measurement strip was added, and the subsequent state estimate was used for control. The present paper aims at the application of the recent development and improvement on the estimation of the complex flow cases where the full information control was shown to be successful in Högberg & Henningson (2002).

The structure of this paper is as follow. In §2, the flow system is described: dynamics, input and output. In §3, we outline the main issues for the feedback control and estimation. The numerical method is described in §4. The performance of the control in several flow cases is shown in §5, and concluding remarks are given in §6.

## 2. System description

### 2.1. Flow dynamics

The Navier–Stokes equations are linearized about solutions of the FSC boundary layer. Favourable and adverse pressure gradients can be accounted for as well as the effect of a sweep. To obtain the family of FSC similarity solutions we assume that the chordwise outer-streamline velocity obeys the power law  $U_\infty^* = U_0^*(x^*/x_0^*)^m$  and that the spanwise free-stream velocity  $W_\infty^*$  is constant.

In the expression above,  $U_0^*$  is the free-stream velocity at a fixed position  $x_0^*$ , the physical distance from the leading edge, and the asterisks (\*) denote dimensional quantities. Note that the Blasius profile is a special case of the FSC boundary layer with zero cross-flow component and no pressure gradient. If we choose the similarity variable  $\xi$  as

$$\xi(y^*) = y^* \sqrt{\frac{m+1}{2} \frac{U_\infty^*}{2\nu x^*}}$$

one can derive the following self-similar boundary layer profiles,

$$\begin{aligned} f''' + ff'' + \beta_h(1 - f'^2) &= 0, \\ g'' + fg' &= 0, \end{aligned}$$

where the Hartree parameter  $\beta_h$  relates to the power law exponent  $m$  as  $\beta_h = 2m/(m+1)$ . The accompanying boundary conditions are

$$\begin{aligned} f = f' = g &= 0, \quad \text{for } \xi = 0, \\ f' \rightarrow 1, \quad g \rightarrow 1, &\quad \text{as } \xi \rightarrow \infty. \end{aligned}$$

The complete derivation can be found in e.g. Schlichting (1979) and Cooke (1950). From the FSC similarity solutions  $f$  and  $g$ , we construct the nondimensional velocity profiles

$$U(y) = f'(\xi(y)), \tag{1a}$$

$$W(y) = \frac{W_\infty^*}{U_\infty^*} g(\xi(y)), \tag{1b}$$

for a fixed  $x = (x^* - x_0^*)/\delta_0^*$  and where  $y = y^*/\delta_0^*$ . The symbol  $\delta_0^*$  denotes the displacement thickness at position  $x^* = x_0^*$ . The velocity profiles (1a) and (1b) are then used as base flow when constructing the linear dynamic model for the flow disturbance and the initial conditions for the direct numerical simulations (DNS).

Once linearized, the system can be transformed to Fourier space by assuming local spatial invariance. This implies that the non-parallel effects are small, i.e. the base flow is slowly developing in the streamwise direction. After transformation to the velocity–vorticity ( $v - \eta$ ) formulation, we obtain the Orr–Sommerfeld/Squire equations (see e.g. Schmid & Henningson 2001)

$$\begin{pmatrix} \dot{v} \\ \dot{\eta} \end{pmatrix} = \begin{pmatrix} \mathcal{L}_{OS} & 0 \\ \mathcal{L}_C & \mathcal{L}_{SQ} \end{pmatrix} \begin{pmatrix} v \\ \eta \end{pmatrix}, \tag{2}$$

where

$$\begin{aligned} \mathcal{L}_{OS} &= \Delta^{-1}[-i(k_x U + k_z W)\Delta + ik_x U'' + ik_z W'' + \Delta^2/Re], \\ \mathcal{L}_{SQ} &= -i(k_x U + k_z W) + \Delta/Re, \\ \mathcal{L}_C &= i(k_x W' - k_z U'), \end{aligned} \tag{3}$$

and where the Laplacian operator is denoted  $\Delta = D^2 - k^2$  and  $D$  is the wall-normal derivative and  $k^2 = k_x^2 + k_z^2$ . The boundary conditions are defined as

$$\begin{aligned} v(0, t) = \varphi, \quad Dv(0, t) &= 0, \quad \eta(0, t) = 0, \\ v(y, t) = 0, \quad Dv(y, t) &= 0, \quad \eta(y, t) = 0, \quad \text{as } y \rightarrow \infty. \end{aligned} \quad (4)$$

The control actuation affects the system through a non-homogeneous boundary condition on the wall-normal velocity  $\varphi(t)$  (time varying wall blowing and suction). The Reynolds number  $Re$  is based on the free-stream velocity and displacement thickness.

In order to apply tools from control theory, see for example Lewis & Syrmos (1995), it is convenient to write the linearized fluid system in the general state-space form

$$\begin{aligned} \dot{q} &= Aq + B_2 u_c + B_1 f, \quad q(0) = q_0, \\ y &= Cq + g, \end{aligned} \quad (5)$$

where  $q$  is the state,  $A$  is the linear operator representing the dynamics of the system. The external disturbances, denoted by  $f$ , force the state through the input operator  $B_1$ , and  $q_0$  is the initial condition. The operator  $B_1$  transforms a forcing on  $(u, v, w)$  to a forcing on  $(v, \eta)$ , since the flow state is expressed in this formulation. The control signal  $u_c$  affects the system through the input operator  $B_2$ . Operator  $C$  extracts the measurements from the state variable, and  $g$  adds a stochastic measurement noise with given statistical properties. The noisy measurement is then denoted by  $y$ .

The controlled Orr–Sommerfeld/Squire system can be cast into the formalism of (5) by means of a lifting procedure (see e.g. Högberg *et al.* 2003a) where the control at the wall now enters the flow through a volume forcing term instead of as an inhomogeneous boundary condition at the wall. This is done by decomposing the flow state into a time varying homogeneous component (subscript  $h$ ) and a steady particular (subscript  $p$ ) component

$$\begin{pmatrix} v(t) \\ \eta(t) \end{pmatrix} = \begin{pmatrix} v_h(t) \\ \eta_h(t) \end{pmatrix} + \begin{pmatrix} v_p \\ \eta_p \end{pmatrix} \varphi(t). \quad (6)$$

The augmented state  $q$ , incorporating the actuation variable, thus reads

$$q = \begin{pmatrix} v_h(y, t) \\ \eta_h(y, t) \\ \varphi(t) \end{pmatrix}, \quad (7)$$

and augmented operator  $A$  and operator  $B$  (see §3) can be written

$$A = \begin{pmatrix} \mathcal{L}_{OSS} & \mathcal{L}_{OSS} q_p \\ 0 & 0 \end{pmatrix}, \quad B = \begin{pmatrix} -q_p \\ 1 \end{pmatrix}, \quad (8)$$

with

$$\mathcal{L}_{OSS} = \begin{pmatrix} \mathcal{L}_{OS} & 0 \\ \mathcal{L}_C & \mathcal{L}_{SQ} \end{pmatrix}, \quad (9)$$

and where the particular solution  $q_p$  is chosen to satisfy the numerically convenient equation  $\mathcal{L}_{OSS} q_p = 0$  with a unity boundary condition on the wall-normal velocity at the wall. With this formulation the control signal becomes  $u_c = \dot{\varphi}$ .

## 2.2. Stochastic disturbances

2.2a. *Modeling of the external disturbances.* The description of a dynamical system can also include a description of its input (external sources of excitations) and its output (measurements, possibly corrupted by noise). The performance of the state estimation relies on the construction of a proper model for the flow disturbances. Indeed, if the external sources of perturbations in the flow are well identified, it becomes an easy task to estimate the flow evolution using a dynamic model of the system.

The external sources of perturbations in typical aeronautical applications can be wall roughness, acoustic waves, and free-stream turbulence. In the case where the sensors are distributed over a strip in the boundary layer, upstream instabilities can generate waves that are to be considered as disturbances to the estimator.

We will assume the external disturbance forcing  $f = (f_1, f_2, f_3)$  in (5) to be a zero-mean stationary white Gaussian process with auto-correlation

$$E[f_j(x, y, z, t)f_k(x + r_x, y', z + r_z, t')] = \underbrace{\delta(t - t')}_{\text{Temporal}} \underbrace{Q_{f_j f_k}(y, y', r_x, r_z)}_{\text{Spatial}},$$

where  $\delta(\cdot)$  denotes the Dirac  $\delta$ -function.

The remaining property to be described is the spatial extent of the two-point, one-time, auto-correlation of  $f$  over the whole domain

$$Q_{f_j f_k}(y, y', r_x, r_z) = E[f_j(x, y, z, t)f_k(x + r_x, y', z + r_z, t)].$$

The corresponding quantity in Fourier space is a covariance operator, obtained for any wavenumber pair  $\{k_x, k_z\}$  via the following integration over the homogeneous directions

$$R_{f_j f_k}(y, y', k_x, k_z) = \int \int Q_{f_j f_k}(y, y', r_x, r_z) e^{-i(k_x r_x + k_z r_z)} dr_x dr_z.$$

Our model for the covariance of  $f$  assumes that the disturbance has a localized structure in space (i.e., the two-point correlation of the disturbance decays exponentially with distance) and that the correlations between forcing terms on different velocity components are zero. We assume a model for the covariance of the external forcing  $f$  of the form

$$R_{f_j f_k}(y, y', k_x, k_z) = d(k_x, k_z) \delta_{jk} \mathcal{M}^y(y, y'), \quad (10)$$

where

$$d(k_x, k_z) = \exp \left[ - \left( \frac{k_x - k_x^0}{d_x} \right)^2 - \left( \frac{k_z - k_z^0}{d_z} \right)^2 \right]. \quad (11)$$

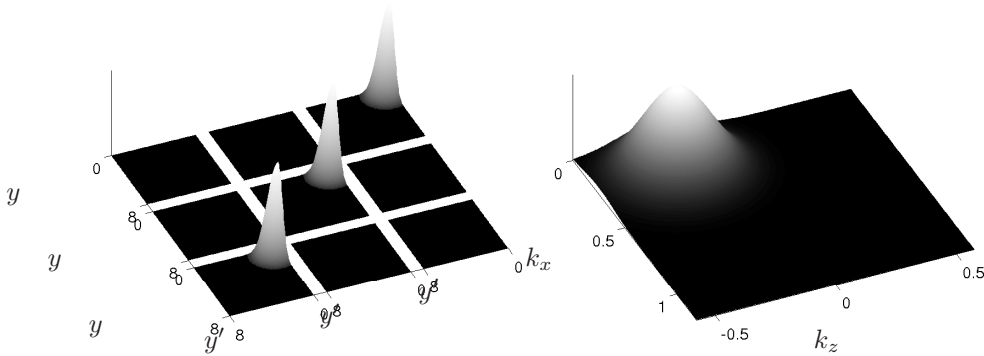


FIGURE 1. The covariance of  $f$ , for the FSC problem (cases 12–13 in table 1), is depicted in (a). The covariance is focused to the interior of the boundary layer. From top to bottom and right to left each square represent the covariance for  $f_1$ ,  $f_2$ , and  $f_3$ . The wavenumber space amplitude function is shown in (b). The peak is set at  $\{0.25, -0.25\}$ , about the mode that is triggered in the FSC simulations.

The model parameters  $k_x^0$  and  $k_z^0$  can be used to locate the peak energy of the disturbances in Fourier space, and  $d_x$  and  $d_z$  to tune the width of this peak. These parameters are specific for each flow case, e.g. for a typical TS-wave the peak energy will be at  $k_x^0 = 0.3$  and  $k_z^0 = 0$ , or for a typical streamwise streak, the choice will be  $k_x^0 = 0$  and  $k_z^0 = 0.5$ .

The  $y$ -variation of  $R_{f_j f_k}$  is given by the function

$$\mathcal{M}^y(y, y') = w((y + y')/2) \exp\left[-\frac{(y - y')^2}{2d_y}\right], \quad (12)$$

where the design parameter  $d_y$  governs the width of the two-point correlation of the disturbance in the wall-normal direction. The function  $w(\xi)$  describes the variances at different distances from the wall. In the present paper, the estimator will be applied to disturbances inside the boundary layer, we thus use the wall-normal derivative of the base flow,

$$w(\xi) = \frac{U'(\xi)}{U'(0)}, \quad (13)$$

so that the variance of the disturbance varies as the mean shear: greatest close to the wall and vanishing in the free-stream. The model parameters for all flow cases presented are given in table 2.

Other forms for  $d(k_x, k_z)$  are also possible, and may be experimented with in future work. Note that we will denote  $R = R_{ff} = \text{diag}(R_{f_1 f_1}, R_{f_2 f_2}, R_{f_3 f_3})$  in the sections that follow.

2.2b. *Sensors and sensor noise.* The measurements used in this study are the streamwise and spanwise shear stresses and the wall pressure fluctuations.

$$\begin{cases} \tau_x = \tau_{xy}|_{\text{wall}} = \frac{1}{Re} \frac{\partial u}{\partial y} \Big|_{\text{wall}} = \frac{1}{Re} \frac{i}{k^2} (k_x D^2 v - k_z D \eta) \Big|_{\text{wall}}, \\ \tau_z = \tau_{zy}|_{\text{wall}} = \frac{1}{Re} \frac{\partial w}{\partial y} \Big|_{\text{wall}} = \frac{1}{Re} \frac{i}{k^2} (k_z D^2 v + k_x D \eta) \Big|_{\text{wall}}, \\ p = p|_{\text{wall}} = \frac{1}{Re} \frac{1}{k^2} D^3 v \Big|_{\text{wall}}. \end{cases}$$

which yields the following measurement matrix  $C$

$$C = \frac{1}{Re} \frac{1}{k^2} \begin{pmatrix} ik_x D^2 \Big|_{\text{wall}} & -ik_z D \Big|_{\text{wall}} \\ ik_z D^2 \Big|_{\text{wall}} & ik_x D \Big|_{\text{wall}} \\ D^3 \Big|_{\text{wall}} & 0 \end{pmatrix}.$$

Each of the three measurements is assumed to be corrupted by random sensor noise processes, the amplitude of which is determined by the assumed quality of the sensors. The covariance of the sensor noise vector  $g$  can thus be described in Fourier space by a  $3 \times 3$  matrix  $G$  where the diagonal elements  $\alpha_l^2$  are the variances of the sensor noise assumed to be associated with each individual sensor. The covariance for each sensor can be written on the following form

$$R_{g_l(t), g_\kappa(t')} = \delta_{l\kappa} \delta(t - t') \alpha_l^2, \quad (14)$$

where  $\delta_{l\kappa}$  denotes the Kronecker delta. Thus, in the present work, we assume that the sensor noise is uncorrelated in both space and time.

When the signal-to-noise ratio is low, the measured signal must be fed back only gently into the estimator, lest the sensor noise disrupt the estimator. When the signal-to-noise ratio is high, the measured signal may be fed back more aggressively into the estimator, as the fidelity of the measurements can be better trusted. For a given covariance of the external disturbances, the tuning of the assumed overall magnitude of the sensor noise in the Kalman filter design thus provides a natural “knob” to regulate the magnitude of the feedback into the estimator.

### 3. Compensation

The system is now described: its dynamics is governed by (2), it is excited by external sources of disturbance as in (11) and the sensor information is corrupted by noise as in (14). We can now apply the procedure of LQG control and estimation governed by system 5.

#### 3.1. Controller

To construct an optimization problem we need to define an objective function. The performance measure for optimality is chosen as a weighted sum of the

flow kinetic energy and the control effort. We thus aim at preventing small disturbances from growing, and achieve this goal with the minimum possible actuation energy. The objective functional thus reads

$$J = \int_0^\infty (q^* \mathcal{Q}q + l^2 u_c^* u_c) dt \tag{15}$$

where  $l^2$  is included to penalize the time derivative of the control  $u_c = \dot{\varphi}$ , and

$$\mathcal{Q} = \begin{pmatrix} Q & Qq_p \\ q_p^* Q & (1+r^2)q_p^* Qq_p \end{pmatrix} \tag{16}$$

where the term  $r^2$  is an extra penalty on the control signal itself. The operator  $Q$  represents the energy inner-product in the  $(v, \eta)$  space

$$(v^* \ \eta^*) Q \begin{pmatrix} v \\ \eta \end{pmatrix} = \frac{1}{8k^2} \int_0^\infty \left( k^2 |v|^2 + \left| \frac{\partial v}{\partial y} \right|^2 + |\eta|^2 \right) dy, \tag{17}$$

with  $k^2 = k_x^2 + k_z^2$ .

We now want to find the optimal  $K$  that feeds back the state to update the control  $u_c = Kq$ . It can be found as the solution of an algebraic Riccati equation (ARE)

$$A^* X + XA - \frac{1}{l^2} X B_2 B_2^* X + \mathcal{Q} = 0 \tag{18}$$

where  $X$  is the unique non-negative self-adjoint solution. Note that the linear feedback law does not depend on the disturbances present in the flow and is thus computed once and for all for a given objective function and base flow. The optimal control gain  $K$  is

$$K = -\frac{1}{l^2} B_2^* X. \tag{19}$$

A sufficient range of wavenumber pairs are computed and after Fourier transformation in both horizontal directions, we obtain physical space control convolution kernels. Examples of such control kernels are depicted in figure 2.

### 3.2. Estimator

We build an estimator analogous to the dynamical system (5) as

$$\begin{aligned} \dot{\hat{q}} &= A\hat{q} + B_2 u_c - L(y - \hat{y}), \quad \hat{q}(0) = \hat{q}_0, \\ \hat{y} &= C\hat{q}, \end{aligned} \tag{20}$$

where  $\hat{q}$  is the estimated state and  $\hat{y}$  represents the measurements in the estimated flow.

Kalman filter theory, combined with the models outlined in §2.2a and §2.2b for the statistics of the unknown external forcing  $f$  and the unknown sensor noise  $g$  respectively, provides a convenient and mathematically-rigorous tool for computing the feedback operator  $L$  in the estimator described above such that  $\hat{q}(t)$  converges to an accurate approximation of  $q(t)$  (see e.g. Lewis & Syrmos

1995, p. 463–470). Note that the volume forcing  $v_e = L(y - \hat{y})$  used to apply corrections to the estimator trajectory is proportional to the measurement difference in the flow and in the estimator  $\tilde{y} = y - \hat{y}$ .

The problem reduces to solving an algebraic Riccati equation similar to equation (18)

$$0 = AP + PA^* - PC^*G^{-1}CP + B_1RB_1^*, \quad (21)$$

where  $P$  is the unique non-negative self-adjoint solution. The optimal gain  $L$  that minimizes the expected energy of the state estimation error at steady state is

$$L = -PC^*G^{-1}. \quad (22)$$

Estimation convolution kernels are exemplified in figure 3.

### 3.3. *Extension to spatially developing flows*

When solving the linear control problem and computing optimal control and estimation gains we have linearized about a base flow profile at a specific streamwise position, hence assuming a parallel base flow. However, due to the non-parallel base flows in the DNS, errors will be introduced when the control signal and estimation forcing are computed. Based on findings in Högberg & Henningson (2002), Högberg *et al.* (2003*b*), Högberg *et al.* (2003*c*), and Chevalier *et al.* (2006) it was expected that the controller and the estimator had some robustness properties with respect to changes in the base flow profile. Due to the fact that the convolution kernels themselves, for proper choices of parameters, are localized indicates that only local information is needed which relaxes the requirement of constant base flow profile. For almost all control and estimation gains, the base flow profile in the centre of the control and measurement regions have been used. For the longer control interval in the optimal perturbation flow case, the same gains were used as for the shorter interval.

The control and estimation convolution kernels for the Falkner–Skan–Cooke boundary layer flow, corresponding to cases 12–13 in table 1, are depicted in figures 2 and 3. Both the control and estimation kernels were computed with a physical box size of  $100 \times 10 \times 125.7$  with  $192 \times 65 \times 125.7$  Fourier, Chebyshev, Fourier modes. Furthermore, the kernels were based on the mean-flow at  $x = 95$  and  $x = 200$  for the estimation and control respectively. For all cases studied the general behaviour of the control kernels are the same in the sense that they all reach upstream in order to get information about the perturbations present in the flow. Correspondingly the estimation kernels reach downstream from the point of sensing yielding information on how each measurement should force the estimator. However, due to the differing base flows and their inherent instabilities the kernels will differ in shape and extent. The streamwise length of the sensing/actuation strip is limited above due to the non-parallel base flow, and below by the physical extent of the convolution kernels. The control and estimation region lengths used in this paper for the

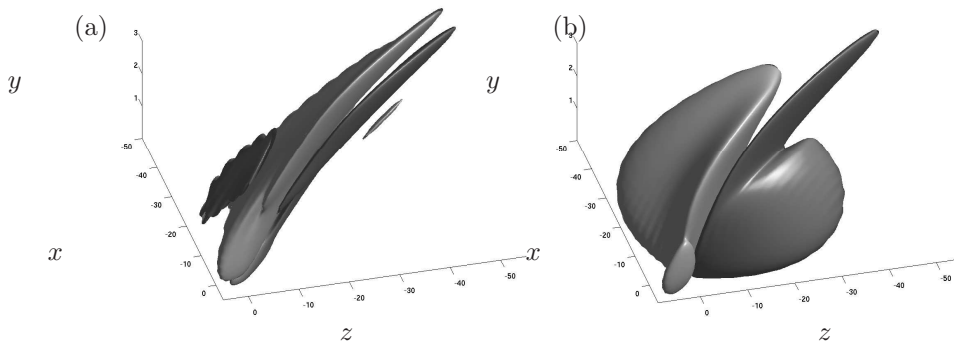


FIGURE 2. Steady-state control convolution kernels relating the flow state  $\hat{v}$  (a) and  $\hat{\eta}$  (b) to the control at  $\{x = 0, y = 0, z = 0\}$  on the wall. Positive (dark) and negative (light) isosurfaces with isovalues of  $\pm 20\%$  of the maximum amplitude for each kernel are illustrated. The kernels correspond to cases 12–13 in table 1 and 3.

spatial flow cases were chosen in this range. Note that the performance of the controller/estimator degrades with “out of limit” parameters but will generally still produce reasonable results.

## 4. Numerical issues

### 4.1. Direct numerical simulations

All direct numerical simulations have been performed with the code reported in Lundbladh *et al.* (1992) and Lundbladh *et al.* (1999), which solves the incompressible Navier–Stokes equations

$$\begin{aligned} \frac{\partial \mathbf{u}}{\partial t} &= NS(\mathbf{u}) + \lambda(x)(\mathbf{u} - \mathbf{u}_\lambda) + \mathbf{F}, \\ \nabla \cdot \mathbf{u} &= 0, \end{aligned} \quad (23)$$

by a pseudo-spectral approach. The velocity vector  $\mathbf{u}$  is defined as  $\mathbf{u} = (u, v, w)$ . In the subsequent we will divide the velocity field into a base flow  $\mathbf{U} = (U, V, W)$  and a disturbance part  $\mathbf{u}' = (u', v', w')$  so that  $\mathbf{u} = \mathbf{U} + \mathbf{u}'$ . In order to allow spatially developing flows, a fringe region technique as described in e.g. Nordström *et al.* (1999) has been applied. This forcing is implemented in the term  $\lambda(x)(\mathbf{u} - \mathbf{u}_\lambda)$ , where  $\lambda(x)$  is a non-negative function which is nonzero only in the fringe region located in the downstream end of the computational box. The outflow and inflow conditions are determined by the desired velocity distribution  $\mathbf{u}_\lambda$ . The other additional forcing term  $\mathbf{F} = (F_1, F_2, F_3)$  is used e.g. to enforce a parallel base flow in temporal simulations, or to introduce perturbations in the spatial simulations.

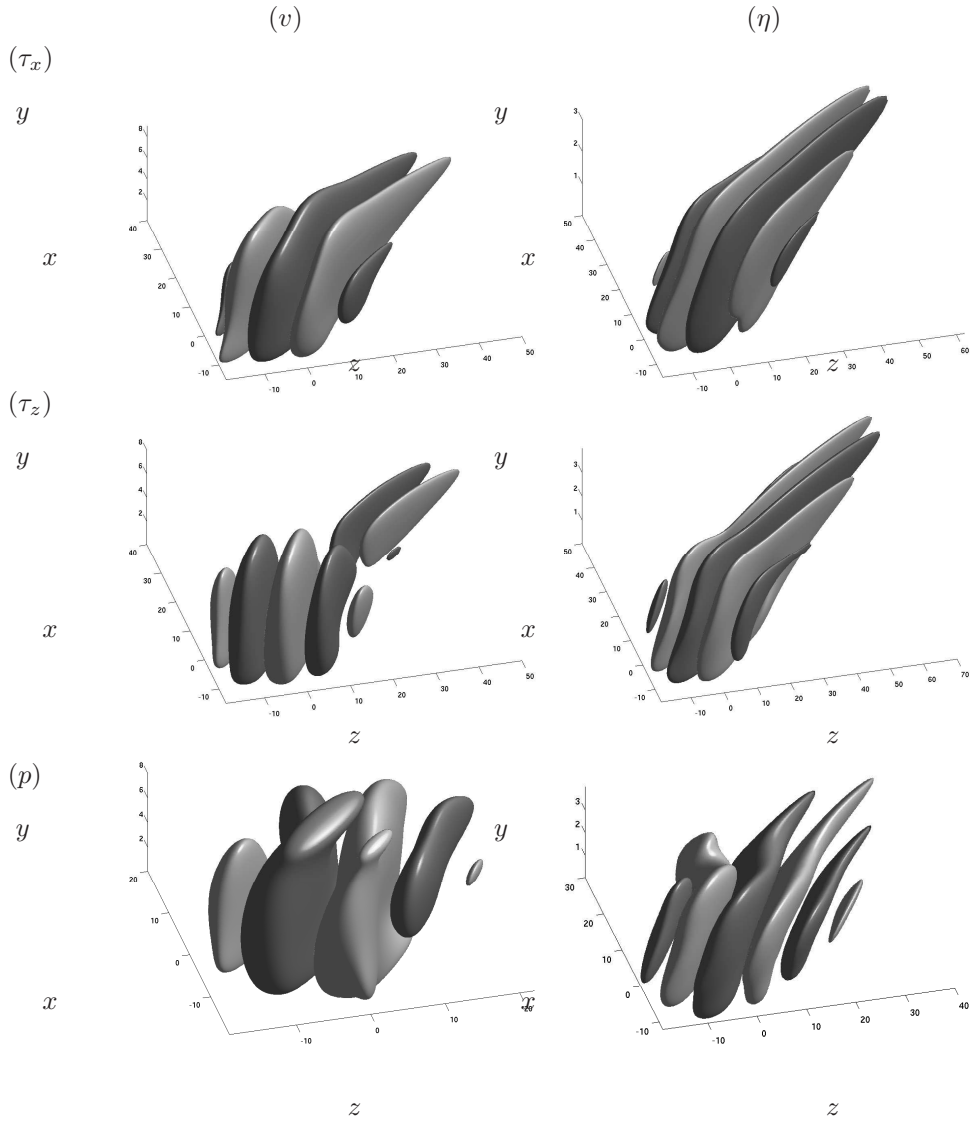


FIGURE 3. Steady-state estimation convolution kernels relating the measurements  $\tau_x$ ,  $\tau_z$ , and  $p$  at the point  $\{x = 0, y = 0, z = 0\}$  on the wall to the estimator forcing on the interior of the domain for the evolution equation for the estimate of (left)  $\hat{v}$  and (right)  $\hat{\eta}$ . Positive (dark) and negative (light) iso-surfaces with isovalues of  $\pm 10\%$  of the maximum amplitude for all kernels illustrated. The kernels correspond to case 13 in tables 1 and 3.

At the lower wall a no-slip boundary condition is applied where it is also possible to apply zero mass-flux blowing and suction. An asymptotic free-stream boundary condition is used to limit the computational box in the wall-normal direction, at a constant height from the lower wall (see e.g. Malik *et al.* 1985).

The computational domain is discretized in space by Fourier series in both horizontal directions and with Chebyshev polynomials in the wall-normal direction. The time integration uses a four-step low-storage third-order Runge–Kutta method for the advective and forcing terms whereas the viscous terms are treated by a Crank–Nicolson method. The incompressibility condition is enforced implicitly by expressing the flow state in the wall-normal velocity and wall-normal vorticity state space.

#### 4.2. Temporal simulations

When needed, we add a volume forcing vector  $\mathbf{F} = (F_1, F_2, F_3)$  to enforce a parallel base flow, defined as

$$\begin{aligned} F_1 &= -\frac{\partial U(y, t)}{\partial t} - \frac{1}{Re} \frac{\partial^2 U(y, t)}{\partial y^2}, \\ F_2 &= 0, \\ F_3 &= -\frac{1}{Re} \frac{\partial^2 W(y, t)}{\partial y^2}. \end{aligned} \tag{24}$$

The velocity profiles  $U(y, t)$  and  $W(y, t)$  are given for a spatial position  $x_r$ . To further allow for a moving frame we make the following variable transformation  $x_r = x_0 + ct$  where  $c$  is the reference frame speed and let  $U(x_r, y) = U(x_0 + ct, y) = U(t, y)$ .

#### 4.3. Spatial simulations

4.3a. *Fringe region.* By adding the fringe forcing mentioned in §4.1 we can enforce flow periodicity and thus apply spectral methods allowing us to solve spatially developing flows. The fringe function is defined as

$$\lambda(x) = \lambda_{\max} \left[ S \left( \frac{x - x_{\text{start}}}{\Delta_{\text{rise}}} \right) - S \left( \frac{x - x_{\text{end}}}{\Delta_{\text{fall}}} \right) \right] \tag{25}$$

where the ramping function  $S$  is defined as

$$S(x) = \begin{cases} 0, & x \leq 0, \\ 1 / \left[ 1 + \exp \left( \frac{1}{x-1} + \frac{1}{x} \right) \right], & 0 < x < 1, \\ 1, & x \geq 1. \end{cases} \tag{26}$$

The parameters  $x_{\text{start}}$  and  $x_{\text{end}}$  define the start and end location of the fringe domain, whereas the parameters  $\Delta_{\text{rise}}$  and  $\Delta_{\text{fall}}$  define the rise and fall distance of the fringe function.

Case	Flow	Perturbation	Estimation		Control	
			$x_m \in$	$r^2$	$l$	$x_c \in$
0	A	Eigenmode				
1	A	Eigenmode		0	$10^2$	[0, 25.14]
2	A	Eigenmode	[0, 25.14]	0	$10^2$	[0, 25.14]
3	B	TS-wave				
4	B	TS-wave		0	$10^2$	[100, 250]
5	B	TS-wave	[0, 100]	0	$10^2$	[100, 250]
6	C	Optimal				
7	C	Optimal		0	$10^2$	[300, 450]
8	C	Optimal	[0, 300]	0	$10^2$	[300, 450]
9	C	Optimal		0	$10^2$	[300, 750]
10	C	Optimal	[0, 300]	0	$10^2$	[300, 750]
11	D	Random				
12	D	Random		0	$10^2$	[175, 325]
13	D	Random	[40, 150]	0	$10^2$	[175, 325]
14	E	Stationary				
15	E	Stationary		0	$10^2$	[150, 300]
16	E	Stationary	[40, 150]	0	$10^2$	[150, 300]

	Flow	Resolution	Box
A	Temporal FSC	$4 \times 129 \times 4$	$25.14 \times 20 \times 25.14$
B	Spatial Blasius	$576 \times 65 \times 4$	$1128 \times 20 \times 12.83$
C	Spatial Blasius	$576 \times 65 \times 4$	$1128 \times 20 \times 12.83$
D	Spatial FSC	$192 \times 49 \times 48$	$500 \times 8 \times 251.4$
E	Spatial FSC	$768 \times 65 \times 24$	$500 \times 8 \times 25.14$

	Flow	Fringe				
		$x_{\text{start}}$	$x_{\text{mix}}$	$\Delta_{\text{mix}}$	$\Delta_{\text{rise}}$	$\Delta_{\text{fall}}$
B	Spatial Blasius	928	928	50	30	15
C	Spatial Blasius	1028	1028	40	100	20
D	Spatial FSC	350	400	40	100	20
E	Spatial FSC	350	400	40	100	20

TABLE 1. The tables contain detailed information about the simulations performed in this study. Both the control and estimation kernels are computed based on a velocity profile from the centre of each domain except for cases 9–10 where the same control kernels were used as for cases 7–8. The rise and fall distance of the control region and the measurement regions are always  $\Delta x = 5$ . The domain  $x_m$  denotes the measurement region used in the estimator and the domain  $x_c$  denotes the region where blowing and suction is applied in the control part of the simulations. The estimator model parameters for the different cases are given in table 3.

Parameter	Cases		Parameter	Cases	
	3–5	6–10		11–13	14–16
$x_f$	-201.06	-158.16	$x_0$	20.95	20.95
$\omega$	0.06875	0	$a_t$	0.001	
$k_z$	0	0.4897	$a_s$		0.0036
$a_s$	$10^{-5}$		$x_{\text{scale}}$	10	10
$t_s$	0		$y_{\text{scale}}$	1	1
$t_r$	20		$z_{\text{scale}}$		-25.14
			$z_{\text{center}}$	0	0
			$l_{\text{skew}}$		1
			$n_{\text{modes}}$	21	
			$t_{dt}$	1	

TABLE 2. Volume forcing parameters for the spatial simulations. Note that negative coordinates indicate positions upstream of the inflow boundary.

In order to enforce the inflow boundary condition at the downstream end of the domain we construct the following blending function which gives a smooth interpolation between two velocity profiles. Let the velocity components be defined as

$$\begin{aligned}
 u_\lambda &= U(x, y) + [U(x - l_x, y) - U(x, y)] S\left(\frac{x - x_{\text{mix}}}{\Delta_{\text{mix}}}\right) + u'_f(x - l_x, y, z, t), \\
 w_\lambda &= W(x, y) + [W(x - l_x, y) - W(x, y)] S\left(\frac{x - x_{\text{mix}}}{\Delta_{\text{mix}}}\right) + w'_f(x - l_x, y, z, t),
 \end{aligned} \tag{27}$$

where  $l_x$  is the box length in the streamwise direction. The parameters  $x_{\text{mix}}$  and  $\Delta_{\text{mix}}$  are both blending parameters. The former is the start of the blending region and the latter is the rise distance of the blending. Additional forcing to add streaks or different wave forms can be added through the velocity components ( $u'_f, v'_f, w'_f$ ) directly in the fringe.

4.3b. *Perturbations.* To introduce perturbations into the spatially evolving flow an external volume force can be applied locally in the computational domain. This forcing can either be applied in the fringe region, as for the optimal disturbance and the TS-wave case, or in the physical flow domain.

In order to introduce unsteady perturbations in the physical computational domain, we use a random forcing, acting only on the wall-normal component of the momentum equations

$$F_2^{\text{rand}} = a_t \exp[-((x - x_{\text{center}})/x_{\text{scale}})^2 - (y/y_{\text{scale}})^2] f(z, t), \tag{28}$$

where

$$f(z, t) = [(1 - b(t))h^k(z) + b(t)h^{k+1}(z)] \quad (29)$$

and

$$\begin{aligned} k &= \text{floor}(t/t_{dt}), \\ b(t) &= 3p^2 - 2p^3, \\ p &= t/t_{dt} - k, \end{aligned} \quad (30)$$

where floor denote rounding to the next smaller integer, and  $h^k(z)$  is a Fourier series of unit amplitude functions with random phase generated at every time interval  $k$ . Within each time interval  $t_{dt}$ , the function  $b(t)$  ramps the forcing smoothly in time. The maximum amplitude is determined by  $a_t$  and the forcing is exponentially decaying in both the streamwise and wall-normal directions centred at  $x_{\text{center}}$ . The number of modes with non-zero amplitude is determined by the parameter  $n_{\text{modes}}$ . This forcing has been used to generate the travelling cross-flow vortices described as cases 11–13 in table 1 with the corresponding parameters given in table 2.

Generating disturbances in the fringe region is done through prescribing the components  $(u'_f, v'_f, w'_f)$  in equation (27). Since we are looking at the evolution of linear disturbances, these components can be taken as the eigenfunctions of the parabolized stability equations, known as the PSE (Bertolotti *et al.* 1992; Herbert 1997). Input to the eigenvalue problem is a given real frequency  $\omega$ , an appropriate Reynolds number  $Re$  and a real spanwise wavenumber  $k_z^f$ . A set of equations valid for both algebraically and exponentially growing disturbances was derived in Levin (2003), capturing the different scales associated with the two growth scenarios. Having obtained the complex eigenvalues  $k_x^f(x)$  and the eigenfunctions  $\hat{q} = (\hat{u}(x, y), \hat{v}(x, y), \hat{w}(x, y))$  from the solution of the PSE, one can readily formulate the forcing applied in the fringe as the real part of

$$q'_f = a_s \hat{q}(x, y) \exp\left(iRe \int_{x_f}^x k_x^f(\xi) d\xi + ik_z^f z - i\omega t\right) S\left(\frac{t - t_s}{t_r}\right) \quad (31)$$

where  $x_f$  is typically the start of the fringe region and  $a_s$  is the amplitude of the disturbance. The ramping function  $S$  is given by equation (26) and  $t_s$  and  $t_r$  are used as time ramping parameters.

4.3c. *Zero mass-flux actuation.* The numerical model in the DNS does not allow for net inflow or outflow, we thus have to enforce a zero-mass flux through the actuation strip by the transformation

$$\hat{\varphi}(x, z) = (\varphi(x, z) + c)H(x), \quad (32)$$

where

$$c = -\frac{\int_z \int_x \varphi(x, z) H(x) dx dz}{z_l \int_x H(x) dx} \quad (33)$$

and

$$H(x) = S\left(\frac{x - (x_c - l_x^c)}{\Delta x}\right) - S\left(\frac{x - (x_c + l_x^c)}{\Delta x}\right). \quad (34)$$

The parameter  $S(x)$  is defined as in equation (26) and  $x_c$  denotes the centre of the control interval. Parameters  $l_x^c$  and  $l_z^c$  are respectively the length and width of the control domain and  $\Delta x$  is the rise and fall distance of the actuation.

#### 4.4. Compensator algorithm

The compensator algorithm is depicted in figure 4. The “real” flow could be an experimental setup where only wall information is extracted. In our studies the “real” flow is represented by a DNS. The estimator is another DNS, which is used to recover the state from sensor information. The compensation algorithm can be sketched in the following steps

1. Take wall measurements in both real and estimated flows
2. Compute the estimator volume forcing based on precomputed estimation gains and the difference of the wall measurements from the real and estimated flows
3. Apply the volume forcing to the estimator flow to make it converge to the real flow
4. Compute the control signal as a feedback of the reconstructed state in the estimator
5. Apply the control signal in both the real and estimated flows

## 5. Flow cases

In order to evaluate the compensator performance in transitional flows we test a range of different flow cases. To ease the comparison with the full information controller results reported in Högberg & Henningson (2002) we study partly the same flow cases and the same control parameter  $l^2 = 100$  has been used. However, some control regions have been moved further downstream to fit also a measurement region into the computational domain. Note that in principle we could have overlapping control and measurement regions. The computational parameters for each flow type are listed in table 1, 2 and 3.

### 5.1. Single eigenmode

To validate the numerical implementation of the control and the estimator forcing we studied a temporal FSC boundary layer flow where the Reynolds number at the beginning of the simulation box was  $Re = 337.9$  with a free-stream cross-flow velocity component  $W_\infty = 1.44232 U_\infty(x = 0)$  and a favourable pressure gradient  $m = 0.34207$  as defined in §2.1. The same flow setup is also studied in a spatial setting in §5.4. In the case of temporal flow the measurement and control regions overlap since they both extend over the complete wall.

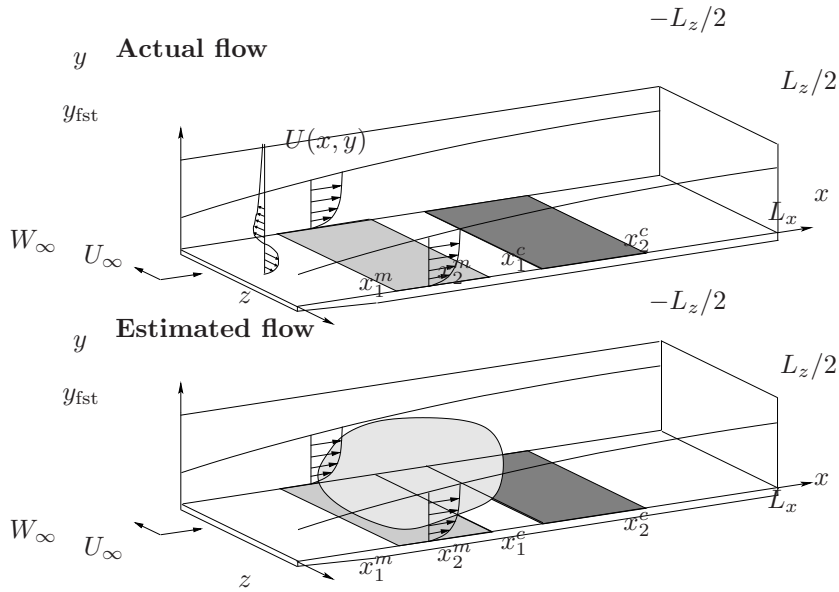


FIGURE 4. Compensator configuration. The upper box represents the “real” flow where the light grey rectangle along the wall is the measurement region ( $x \in [x_1^m, x_2^m]$ ) and the corresponding dark grey rectangle is the control area ( $x \in [x_1^c, x_2^c]$ ). In the beginning of the box a perturbation is indicated as a function of the wall-normal direction. This perturbation will evolve as we integrate the system in time. The estimated flow system is depicted in the lower box. Here the volume force that is based on the wall measurements and the estimation gains is shown as a grey cloud in the computational domain.

The initial disturbance is the unstable eigenfunction associated with the eigenvalue  $c = -0.15246 + i0.0382$  that appears at  $k_x = 0.25$  and  $k_z = -0.25$ . The exponential energy growth of the uncontrolled eigenmode is depicted in figure 5 as a thick solid line. In the same figure the full information controller is plotted as a thick dashed line and the disturbance energy decays rapidly in time and levels out. All thin lines are related to the compensator simulation. The thin solid line represents the disturbance energy in the estimator and it increases initially to quickly align with the energy growth of the actual state. This can also be viewed through the estimation error plotted as a thin dash-dotted line which decays exponentially in time. The compensator control is shown as the thin dashed line. Initially when the estimated state is poor the controller is not very efficient. However as the estimated state improves the compensator control is also improving.

Parameter	Cases				
	3	5	8 & 10	13	16
$k_x^0$	0.25	0.28	0	0.25	0.25
$k_z^0$	-0.25	0.0	0.49	-0.25	-0.25
$d_x$	0.10	0.25	0.15	0.20	0.20
$d_y$	0.10	0.10	0.10	0.10	0.10
$d_z$	0.10	0.25	0.15	0.20	0.20
$\alpha_{\tau_x}$	29.56	4.0	0.20	0.20	0.20
$\alpha_{\tau_z}$	2.21	0.30	0.20	0.20	0.20
$\alpha_p$	14783	2000	300	30000	30000

TABLE 3. Estimator model parameters. The parameters  $k_x^0$ ,  $k_z^0$ ,  $d_x$ ,  $d_y$ , and  $d_z$  all relate to the covariance model of the external disturbances and the parameters  $\alpha_{\tau_x}$ ,  $\alpha_{\tau_z}$ , and  $\alpha_p$  relate to the modeling of the sensor noise.

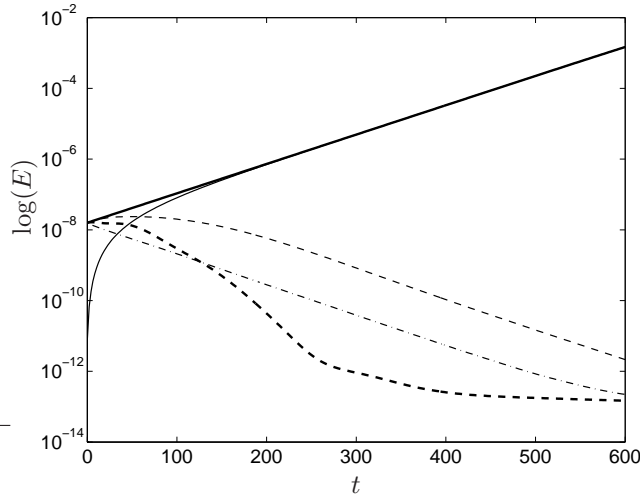


FIGURE 5. Time evolution of the perturbation energy of the uncontrolled unstable eigenmode at  $k_x = 0.25$ ,  $k_z = -0.25$  in a FSC boundary layer and the corresponding controlled system. Solid: uncontrolled energy growth (case 0). Dashed: full information control applied (case 1). Solid-thin: energy growth in the estimator when no control is applied. Dash-dotted-thin: the estimation error when no control is applied. Dashed-thin: compensator control is applied (case 2). The simulations correspond to cases 0-2 in table 1.

5.2. *TS-wave*

The TS-wave perturbation is applied in a spatially developing Blasius boundary layer with an inflow Reynolds number of  $Re = 1150$ . This base flow can be obtained as a similarity solution described in §2.1 with  $m = 0$ . The perturbations are introduced by means of forcing in the fringe region as described in §4.3b. Since the TS-wave is a pure two-dimensional instability, the spanwise wavenumber in (31) is  $k_z^f = 0$ . These waves are forced at the dimensionless oscillating frequency  $F = 59$ , relating to the physical frequency  $\omega$  as  $F = 10^6 2\pi\omega\nu/U_\infty^2$ . This value is chosen according to Levin (2003) where it was found to be the most unstable. The unstable area for this wave extends from Branch I at  $x = -124$  ( $Re \approx 949$ ) to branch II at  $x = 621$  ( $Re \approx 1854$ ). The measurement region is  $x \in [0, 100]$  and the control region is  $x \in [100, 250]$  so that they are both located in the exponential growth region. The simulation parameters correspond to cases 3–5 in table 1 and the parameters defining the fringe forcing are given in table 2.

Figure 6 shows the uncontrolled energy growth and decay as the solid thick line. Full information control, displayed as the thick dash-dotted line, performs perfectly, lowering the amplitude of the energy by approximately five decades. The estimator builds up energy levels throughout the whole estimation region, reaching almost the amplitude of the original flow. This is visualized as the thin solid line.

Note that the difference between the compensator control and full information control in Figure 6 is exaggerated due to the logarithmic scale. In fact this difference is of the same order of magnitude as the energy difference between the real and estimated flow. Indeed by extending the estimation region (and moving the control region further downstream) one can get a closer agreement between the compensator and the full information controller. Note however that there is an interest in controlling the TS-wave evolution as far upstream as possible. Choosing the moderate estimation region length of 100, the compensator still manages to lower the energy levels by almost three decades.

Figure 7(a) shows a snapshot of an  $x$ - $y$  plane of the wall-normal uncontrolled velocity field. The forcing has been turned on long enough to let the waves propagate throughout the whole computational box. In figure 7(b) the compensator control has been active for 926 time units, corresponding to approximately fifteen periods of the forcing. At this instance of time there are still large amplitude disturbances present far downstream, but as can be seen from figure 7(c), 30 periods later the contour-levels of the disturbances are small throughout the whole domain. It is evident that the unsteady blowing and suction has effectively diminished the disturbances, leaving the remaining TS-wave to be advected out of the domain by the base flow.

Instantaneous control signals for the full information control and the compensator control are shown in figure 8. The control signals mimic waves with

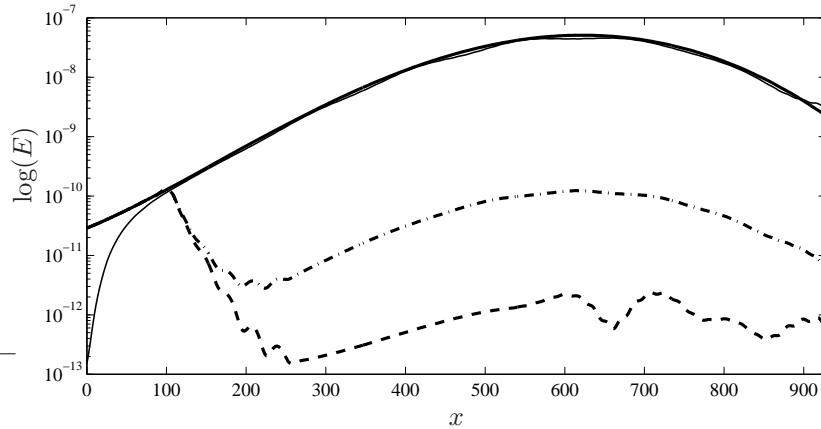


FIGURE 6. Spatial evolution of the perturbation energy of a TS-wave in a spatially growing boundary layer. Solid: uncontrolled energy growth. Solid-thin: estimated flow energy. Dashed: full information control applied. Dash-dotted: compensator control applied.

decaying amplitude in the streamwise direction. The large amplitude at the beginning of the control interval is due to the fact that the controller manages to do the job within only a few wavelengths of the TS-wave, hence leaving large amplitude control further downstream unnecessary.

### 5.3. Optimal perturbation

The compensator performance is also studied for transiently growing perturbations, also known as optimal perturbations after Butler & Farrell (1992). The spatial optimal perturbations in a Blasius boundary layer have been computed by Andersson *et al.* (1999) and Luchini (2000). The optimal perturbation is introduced at  $x = -158.16$  and then marched forward to  $x = 0$  with the technique developed in Andersson *et al.* (1999). The perturbation is introduced in the fringe region to give the proper inflow condition, as described in section §4.3 and with the choice of parameters displayed in table 2. The perturbation is optimized to peak at  $x = 237.24$ .

The base flow is essentially the same as the one described in §5.2, with the same box-size but with a smaller fringe region and a lower Reynolds number. Here the local Reynolds number at the inflow is  $Re = 468.34$  (Andersson *et al.* (2000)). The simulation parameters are given in table 1 as cases 6–10.

Figure 9 shows the energy of the uncontrolled flow, full information control and compensator control once steady state has been reached. Here the energy

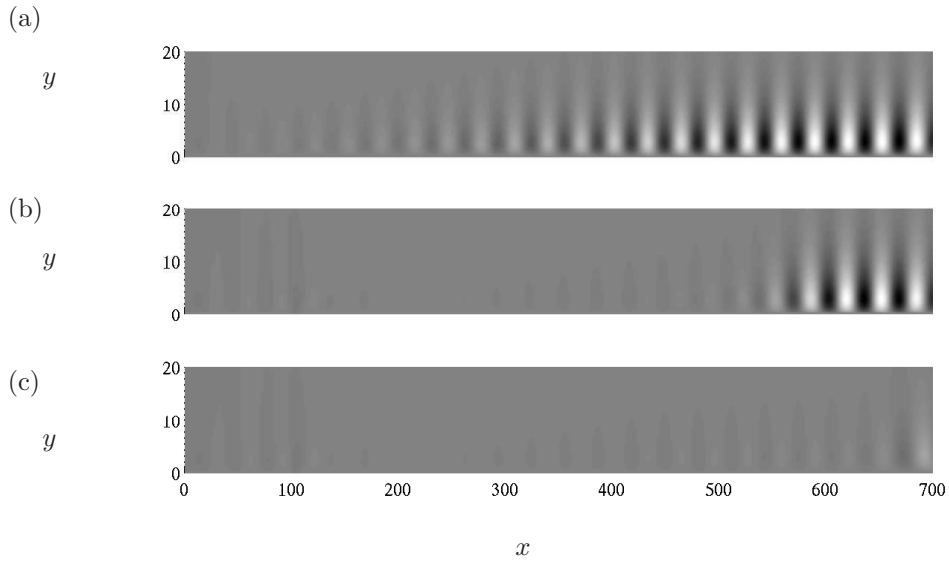


FIGURE 7. A snapshot of the wall-normal perturbation velocity for controlled and uncontrolled TS-waves. (a) The TS-wave at  $t = 3926$  with no control. (b) Compensator control applied during 15 TS-wave periods which corresponds to 926 time units. (c) Compensator control applied during 45 TS-wave periods. The unsteady wall blowing and suction effectively eliminates disturbances, with the result that the original TS-wave disturbances are advected out of the domain. The black to white scales lie within the interval  $v \in [-9.87 \cdot 10^{-5}, 8.18 \cdot 10^{-5}]$

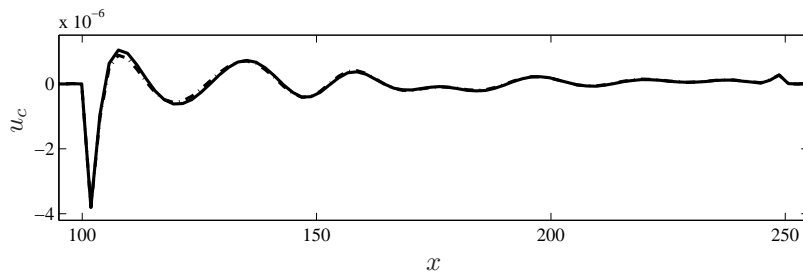


FIGURE 8. Control signal when the control has been turned on for 926 time units. Solid: Full information control. Dash-dotted: Compensator control.

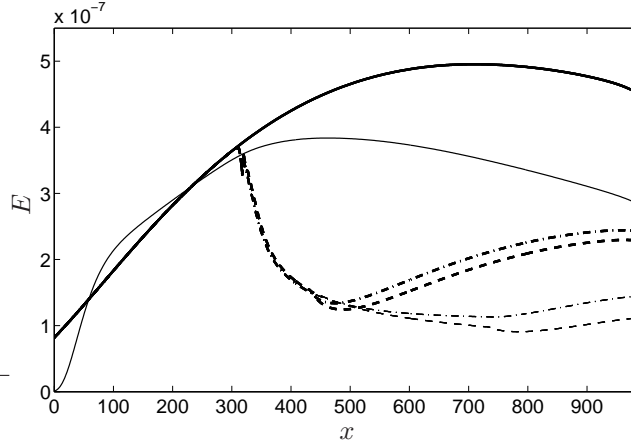


FIGURE 9. Spatial energy evolution of the optimal perturbation. Solid: no control. Dashed: full information control applied in region  $x \in [300, 450]$ . Dash-dotted: compensator control with measurement region  $x_m \in [0, 300]$  and the control region  $x_c \in [300, 450]$ . Thin-solid: estimated flow energy. Thin-dashed: full information control applied in region  $x \in [300, 725]$ . Thin dash-dotted: compensator control with the measurement region  $x_m \in [0, 300]$  and the control region  $x_c \in [300, 725]$ . The flow cases correspond to cases 6–10 in table 1.

is defined as

$$E = \int_0^{2\pi/k_z^0} \int_0^\infty (u^2 + v^2 + w^2) dy dz, \quad (35)$$

where the spanwise wave number is  $k_z^0 = 0.4897$ . Two different lengths of the control regions have been implemented. Both types of controllers for both control intervals work well at reducing the perturbation energy. In the case with a narrow control strip the perturbation energy starts to grow again since a stronger component of the growing disturbance remains. Note that the estimated flow energy does not reach the exact perturbation energy level, but in contrast to the TS-wave perturbation this does not seem to strongly affect the compensator performance.

The control signal for the full information and compensator control cases, applied in the interval  $x \in [300, 750]$ , are depicted in figure 10. The actuation presents a peak at the beginning of the control region and then a fast decay which levels out progressively. A similar feature is reported in Cathalifaud & Luchini (2000) where control is applied over the whole domain.

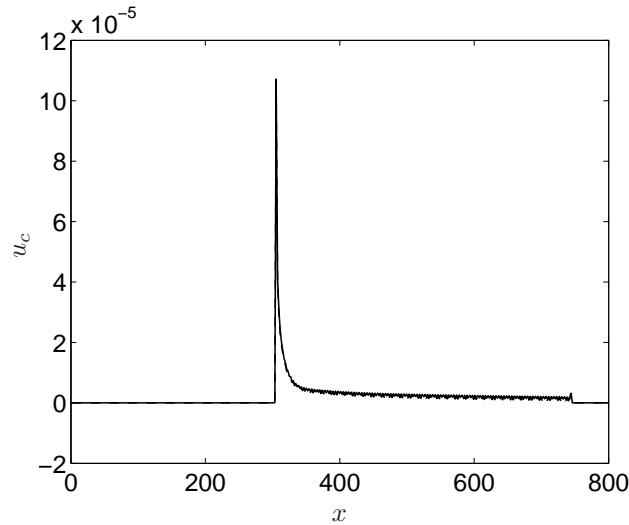


FIGURE 10. The control signal for the optimal disturbance case after the initial transient. Solid: full information control. Dashed: compensator control in domain. The simulations correspond to case 9 and 10 in table 1.

#### 5.4. *Travelling cross-flow vortices*

The FSC boundary layer flow studied in this paper is subject to several other studies, for example Högberg & Henningson (1998) and Högberg & Henningson (2002). Originally it was an attempt to reproduce experimental results where travelling cross-flow modes have been observed (see e.g. Müller & Bippes 1988). A random perturbation in space and time that generates cross-flow vortices downstream is applied, as described in §4.3b. The specific numerical details can be found under cases 11–13 in tables 1 and 2.

In case 11 we compute the time evolution of the forcing as it develops downstream and forms the cross-flow vortices. When the simulations have reached a statistically steady state the disturbance energy is sampled and averaged in time and the spanwise direction as shown in figure 13. The energy growth of the perturbation is shown as a black solid line. In case 12 we apply full information control. Exponential decay then replaces the uncontrolled exponential growth, as shown by the dashed line in figure 11. However almost adjacent to the downstream end of the control region the disturbances start to grow exponentially. Indeed, this wave is unstable over the whole box, and resumes growth behind the control strip. In the same figure the perturbation energy for the compensator is plotted as a dash-dotted line.

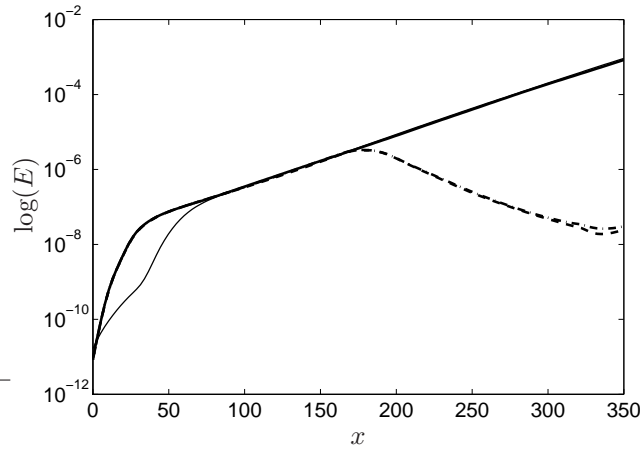


FIGURE 11. Time averaged perturbation energy for cross-flow vortices in a Falkner–Skan–Cooke boundary layer. Solid: uncontrolled. Dashed: full information control. Dash-dotted: compensator control. Thin-solid: estimator energy. The simulations correspond to cases 11–13 in table 1.

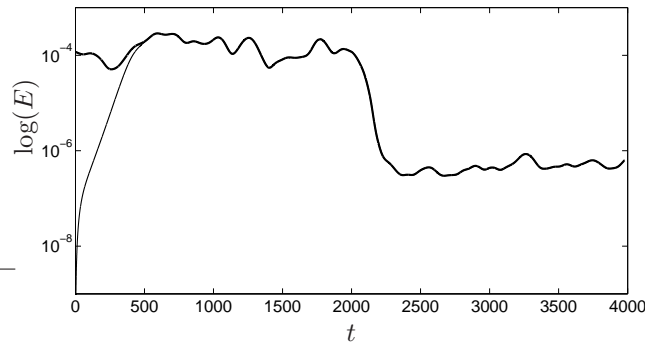


FIGURE 12. Time evolution of the disturbance energy integrated throughout the computational box. During the first 2000 time units the flow is uncontrolled. At time  $t = 2000$  the compensator is turned on. Solid: energy in the flow. Thin-solid: energy in the estimator.

In figure 12 the evolution in time of the perturbation energy, integrated throughout the computational box in space, is shown. The energy in the estimator is shown as a thin-solid line which is zero at time  $t = 0$  but as time evolves reaches the same level as the perturbation energy in the real flow. From figure

12 it is also evident that the estimator is able to adapt to the time variations of the perturbation energy.

The control gains are computed for the base flow at position  $x = 250$  which is the centre of the control domain  $x \in [175, 325]$ . The estimator gains are centred at  $x = 95$  and the measurements are taken in  $x \in [40, 150]$ . In figure 13(a) the uncontrolled flow for the wall-normal perturbation velocity is plotted at  $y = 1.0$ . The corresponding plot for the compensated flow is depicted in figure 13(b).

### 5.5. Stationary cross-flow vortices

Stationary perturbations introduced at the beginning of the computational domain, with large enough amplitudes, will generate stationary nonlinearly saturated cross-flow vortices that develop downstream.

The control is acting in the interval  $x \in [150, 300]$  and the control kernels are computed based on the mean flow at  $x = 225$  with  $l = 10^2$ . The measurement region is in the interval  $x \in [40, 150]$  and the estimation kernels are computed based on the base flow centred in that interval. The complete set of parameters for these simulations is given as cases 14–16 in table 1.

The full information control has been applied to both a flow with fully developed cross-flow vortices throughout the computational domain as well as a flow where the control is turned on at the same time as the perturbation is first introduced in the upstream region. Both approaches give the same result after the initial transients, due to the control. However the transition phase in the former case requires smaller time steps due to stronger transients. There could also be a problem in the former case if too strong wall-normal velocities are generated due to technical limitations in the spectral code that are being used.

For estimation-based control, two approaches regarding the initial state of the estimator have been attempted. First the control is applied after a well converged estimated state is obtained. This leads to full actuation strength immediately. To avoid a strong initial actuation, we turn on estimator and control at the same time. The results shown here have been produced with the latter method.

The simulation is run until a stationary state has been reached and the corresponding energy is shown in figure 14. The solid line shows the perturbation energy and the thin line shows the corresponding estimator state energy. The dashed and dash-dotted lines show the full information and compensated control cases respectively. In both cases, oscillations in the upstream part of the control region indicate that there are nonlinear interactions taking place. As reported in Högberg & Henningson (2002), the full information control turns exponential growth into exponential decay, and downstream of the control region, new cross-flow vortices appear due to the inflectional instability. The

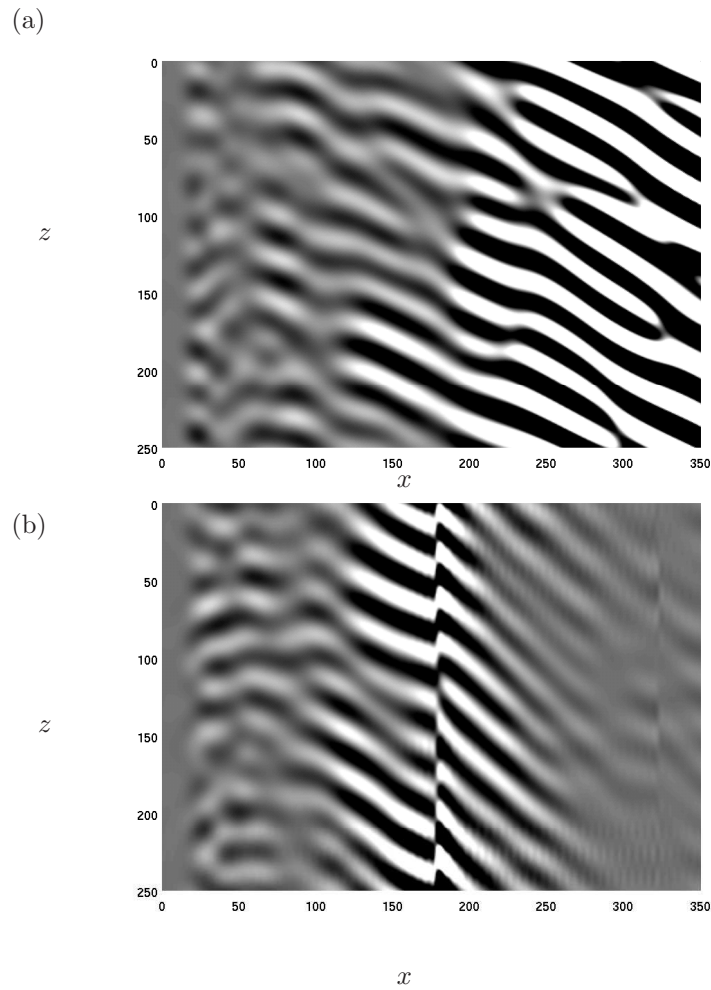


FIGURE 13. Snapshots of the wall-normal velocity component at  $y = 1.0$ . The flow state is depicted in part (a). In (b) the effect of the compensator control is shown. In the controlled flow the actuation was applied in 2000 time units. The black to white scales lie within the interval  $v \in [-0.00045, 0.00055]$ .

compensator control never reaches exponential decay but rather maintains a more or less constant perturbation energy throughout the control interval.

## 6. Conclusions

Based on findings on how to improve the performance state estimation performance, reported in Høpfner *et al.* (2005), combined with the state-feedback

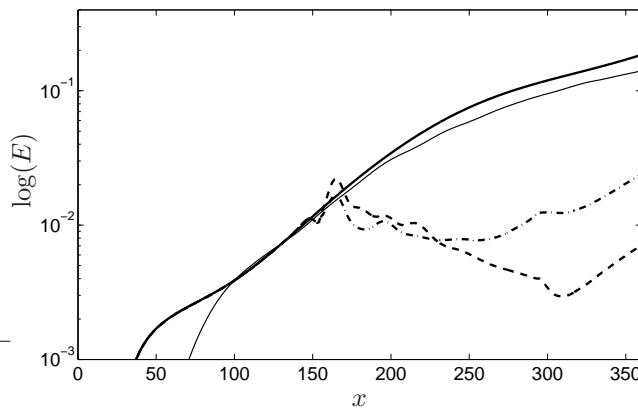


FIGURE 14. Perturbation energy growth for cross-flow vortices in a Falkner–Skan–Cooke boundary layer. Solid: uncontrolled. Dashed: full information control. Dash-dotted: compensator control. Thin-solid: estimator energy. The simulations correspond to cases 14–16 in table 1.

control used in, for example, Bewley & Liu (1998) and Högberg & Henningson (2002), viscous instabilities, non-modal transient energy growth and inflectional instabilities in spatially developing boundary layer flows are controlled based on wall measurement.

The key to the improved performance of the estimator is the design of a physically relevant stochastic model for the external sources of disturbances. For this purpose we choose a correlation length which is weighted to be stronger in the interior of the boundary layer than outside. We also choose an amplitude distribution in wavenumber space such that it represents the most dominant wavenumbers in the specific flow being studied. This procedure leads to well resolved estimation gains for the three measurements: streamwise and spanwise skin frictions and wall pressure. Both the sensor noise and the external disturbances are assumed to be white noise processes. As the estimator is switched on, there is an initial transient that propagates with the group velocity of the dominating disturbances through the computational domain. Upstream of this transient the estimate is converged. This feature makes the compensator control efficient since little extra time is needed to have a good state estimate where it is needed for control, i.e. above the actuation region.

### Acknowledgement

This work has been partially financed by the Innovation fund at the Swedish Defence Research Agency (FOI) and from the EOARD grant FA8655-04-1-3032 which is gratefully acknowledged.

## References

- ANDERSSON, P., BERGGREN, M. & HENNINGSON, D. S. 1999 Optimal disturbances and bypass transition in boundary layers. *Phys. Fluids* **11**, 134–150.
- ANDERSSON, P., BRAND, L., BOTTARO, A. & HENNINGSON, D. S. 2000 On the breakdown of boundary layer streaks. *J. Fluid Mech.* **428**, 29–60.
- BERTOLOTTI, F. P., HERBERT, T. & SPALART, P. R. 1992 Linear and nonlinear stability of the Blasius boundary layer. *J. Fluid Mech.* **242**, 441–474.
- BEWLEY, T. R. 2001 Flow control: new challenges for a new Renaissance. *Progress in Aerospace Sciences* **37**, 21–58.
- BEWLEY, T. R. & LIU, S. 1998 Optimal and robust control and estimation of linear paths to transition. *J. Fluid Mech.* **365**, 305–349.
- BUTLER, K. M. & FARRELL, B. F. 1992 Three-dimensional optimal perturbations in viscous shear flow. *Phys. Fluids A* **4**, 1637–1650.
- CATHALIFAUD, P. & LUCHINI, P. 2000 Algebraic Growth in Boundary Layers: Optimal Control by Blowing and Suction at the Wall. *Eur. J. Mech. B - Fluids* **19**, 469–490.
- CHEVALIER, M., HEPFFNER, J., BEWLEY, T. R. & HENNINGSON, D. S. 2006 State estimation of wall bounded flow systems. Part 2. Turbulent flows. *J. Fluid Mech.* Submitted.
- COOKE, J. C. 1950 The boundary layer of a class of infinite yawed cylinders. *Proc. Camb. Phil. Soc.* **46**, 645–648.
- HERBERT, T. 1997 Parabolized stability equations. *Annu. Rev. Fluid Mech.* **29**, 245–283.
- HEPFFNER, J., CHEVALIER, M., BEWLEY, T. R. & HENNINGSON, D. S. 2005 State estimation in wall-bounded flow systems, Part 1. Laminar flows. *J. Fluid Mech.* **534**, 263–294.
- HÖGBERG, M., BEWLEY, T. R. & HENNINGSON, D. S. 2003*a* Linear feedback control and estimation of transition in plane channel flow. *J. Fluid Mech.* **481**, 149–175.
- HÖGBERG, M., BEWLEY, T. R. & HENNINGSON, D. S. 2003*b* Relaminarization of  $Re_\tau=100$  turbulence using gain scheduling and linear state-feedback control. *Phys. Fluids* **15**, 3572–3575.
- HÖGBERG, M., CHEVALIER, M. & HENNINGSON, D. S. 2003*c* Linear compensator

- control of a pointsource induced perturbation in a Falkner–Skan–Cooke boundary layer. *Phys. Fluids* **15** (8), 2449–2452.
- HÖGBERG, M. & HENNINGSON, D. S. 1998 Secondary instability of cross-flow vortices in Falkner–Skan–Cooke boundary layers. *J. Fluid Mech.* **368**, 339–357.
- HÖGBERG, M. & HENNINGSON, D. S. 2002 Linear optimal control applied to instabilities in spatially developing boundary layers. *J. Fluid Mech.* **470**, 151–179.
- KIM, J. 2003 Control of turbulent boundary layers. *Phys. Fluids* **15** (5), 1093–1105.
- LEVIN, O. 2003 Stability analysis and transition prediction of wall-bounded flows. Licentiate thesis, Royal Institute of Technology, Stockholm.
- LEWIS, F. L. & SYRMOS, V. L. 1995 *Optimal control*. Wiley-Interscience.
- LUCHINI, P. 2000 Reynolds-number-independent instability of the boundary layer over a flat surface: optimal perturbations. *J. Fluid Mech.* **404**, 289–309.
- LUNDBLADH, A., BERLIN, S., SKOTE, M., HILDINGS, C., CHOI, J., KIM, J. & HENNINGSON, D. S. 1999 An Efficient Spectral Method for Simulations of Incompressible Flow over a Flat Plate. Technical Report TRITA-MEK 1999:11. Department of Mechanics, Royal Institute of Technology, KTH.
- LUNDBLADH, A., HENNINGSON, D. S. & JOHANSSON, A. 1992 An Efficient Spectral Integration Method for the Solution of the Navier–Stokes Equations. Technical Report FFA TN 1992-28. FFA, the Aeronautical Research Institute of Sweden, FFA.
- MALIK, M. R., ZANG, T. A. & HUSSAINI, M. Y. 1985 A spectral collocation method for the Navier–Stokes equations. *J. Comp. Phys.* **61**, 64–88.
- MÜLLER, B. & BIPPES, H. 1988 Experimental study of instability modes in a three-dimensional boundary layer. *AGARD-CP 438* **18**.
- NORDSTRÖM, J., NORDIN, N. & HENNINGSON, D. S. 1999 The fringe region technique and the Fourier method used in the direct numerical simulation of spatially evolving viscous flows. *SIAM J. Sci. Comp.* **20** (4), 1365–1393.
- SCHLICHTING, H. 1979 *Boundary-Layer Theory*, seventh edn. Springer.
- SCHMID, P. J. & HENNINGSON, D. S. 2001 *Stability and transition in shear flows, Applied Mathematical Sciences*, vol. 142. Springer-Verlag.
- YOSHINO, T., SUZUKI, Y. & KASAGI, N. 2003 Evaluation of GA-based feedback control system for drag reduction in wall turbulence. In *Proc. 3rd Int. Symp. on Turbulence and Shear Flow Phenomena*, pp. 179–184.

## Paper 2



# Steady solutions of the Navier-Stokes equations by selective frequency damping

By **Espen Åkervik, Luca Brandt, Dan S. Henningson, Jérôme Hoëpfner, Olaf Marxen & Philipp Schlatter**

Linné Flow Centre, KTH Mechanics, SE-100 44 Stockholm, Sweden.

A new method, enabling the computation of steady solutions of the Navier-Stokes equations in globally unstable configurations, is presented. We show that it is possible to reach a steady state by damping the unstable (temporal) frequencies. This is achieved by adding a dissipative relaxation term proportional to the high-frequency content of the velocity fluctuations. Results are presented for cavity-driven boundary-layer separation and a separation bubble induced by an external pressure gradient.

---

## 1. Introduction

The knowledge of a steady base-flow solution of the governing Navier-Stokes equations is fundamental to instability studies and flow control. In the former case it allows for both linear modal and non-modal analyses and weakly non-linear approaches, whereas in the latter case the stabilization of such a base flow can be adopted as a design target. Recent developments, for example as reviewed in Theofilis (2003), have allowed the research community to examine the stability of flows in increasingly complex configurations and to compute two- and three-dimensional eigenmodes, the so-called global modes (Chomaz 2005). Unfortunately, when the flow under consideration is globally unstable, it is virtually impossible to numerically compute a steady-state solution of the Navier-Stokes equations by time-marching methods, in particular for high-order schemes with inherently low numerical dissipation. In some limited cases solutions can be obtained by, e.g., artificially setting the velocity component in certain directions to zero or enforcing symmetries in the system, the most studied example for the latter case being the two-dimensional flow around a circular cylinder. For other cases, the only remaining possibility is the class of Newton iteration methods, which require heavy computational resources for large systems. In this article, we propose a simple numerical approach to compute steady solutions of the Navier-Stokes equations in unstable configurations. We show that it is possible to reach a steady state by damping the most dangerous frequencies and thus quenching the corresponding instability. The method is

adapted from large-eddy simulation (LES) techniques, in particular considering the work of Pruet *et al.* (2003, 2006).

## 2. Problem formulation

Consider the nonlinear system  $\dot{q} = f(q)$ , with appropriate initial and boundary conditions for the vector quantity  $q$  under the operator  $f(q)$ . (A dot is used here to denote the derivative with respect to time). For a flow problem, the above system is the Navier-Stokes equations. A steady state  $q_s$  is then given by  $\dot{q}_s = f(q_s) = 0$ . If  $f$  is unstable, any  $q \neq q_s$  will quickly depart from  $q_s$ . In order to stabilize the above system we propose to apply regularization techniques common in control theory, in this case in the form of proportional (P) feedback control. This amounts to adding to the right-hand side a linear term forcing towards a target solution  $w$ ,

$$-\chi(q - w) , \quad (1)$$

where  $\chi$  is the control coefficient. The theoretical target solution for the control is of course the steady-state solution  $q_s$ , which is however not available *a priori*. Therefore, the actual target solution is a modification of  $q$  with *reduced temporal fluctuations*, i.e. a temporally low-pass filtered solution  $w = T * q$ , defined as the convolution of  $q$  with the temporal filter kernel  $T$ . For the method to converge asymptotically in time to an exact solution of the steady equation, the filter cut-off frequency should be lower than that of the flow instabilities. Therefore, in the following, the unstable frequency will be referred to as high frequency. With these definitions, the modified system is written as

$$\dot{q} = f(q) - \chi(I - T) * q , \quad (2)$$

where  $I$  is the identity operator. As  $q$  is approaching  $q_s$ , the filtered solution  $w = T * q$  will in turn approach  $q$ , therefore reducing the control influence. If  $q$  is the actual steady solution, the time-filtered value  $w$  will be identical to  $q = q_s$ , yielding a vanishing forcing. Hence the steady solution  $q_s$  of the controlled system (2) is also a steady solution of the original problem. Note that there is no generation of new artificial steady states.

A related technique is also used in large-eddy simulation (LES) for the temporal approximate deconvolution model (TADM) (see Pruet *et al.* 2006). Working with spatial filters, a similar relaxation term has been successfully applied in the spectrally-vanishing viscosity (SVV) concept introduced by Tadmor (1989) and in the (spatially filtered) approximate deconvolution model (ADM) of Stolz *et al.* (2001) and the ADM-RT model of Schlatter *et al.* (2004). Following these modeling ideas, a different interpretation of the method can be given as follows. To attenuate unstable high-frequency temporal oscillations and thus reach a steady state we include in the momentum equations an additional linear regularization term, expression (1). This term is effectively damping the high-frequency content of  $q$ . Two parameters have to be chosen in the stabilization

procedure, the filter shape  $T$  and the control gain  $\chi$ . Time-domain filters are discussed first.

### 3. Time-domain filter

For a continuous function  $q(t)$ , a causal low-pass time filter is defined

$$\bar{q}(t) = \int_{-\infty}^t T(\tau - t; \Delta) q(\tau) d\tau, \quad (3)$$

where  $\bar{q}$  is the temporally filtered quantity,  $T$  is the parameterized filter kernel and  $\Delta$  its associated filter width (Pruett *et al.* 2003). To be admissible, the kernel  $T$  must be positive and properly normalized. Additionally, in the limit of vanishing filter width the filter (3) must approach the Dirac delta function. Probably the simplest example of such a filter is the exponential kernel,

$$T(\tau - t; \Delta) = \frac{1}{\Delta} \exp\left(\frac{\tau - t}{\Delta}\right), \quad (4)$$

with the corresponding transfer function in Fourier/Laplace space

$$H(\omega; \Delta) = \int_{-\infty}^0 T(\tau; \Delta) \exp(i\omega\tau) d\tau = \frac{1}{1 + i\omega\Delta}, \quad (5)$$

where  $\omega$  is the circular frequency and  $i = \sqrt{-1}$ . The cutoff frequency of the filter is defined as  $\Re(H(\omega_c; \Delta)) = 1/2$  and is given by  $\omega_c = 1/\Delta$ . The transfer function of the filter is represented in figure 1 for a fixed filter width  $\Delta$ . Note that the transfer function has a considerable imaginary part, which leads to a phase lag in the filtered signal relative to the original signal. For real applications, the integral formulation of the filter (3) is impractical, since it requires the storage of the complete time history of the signal  $q$ . Therefore, the equivalent differential form is adopted,

$$\dot{\bar{q}} = \frac{q - \bar{q}}{\Delta}, \quad (6)$$

which can be readily advanced in time using any integration scheme.

The order of the filter is defined as the index of the first non-vanishing derivative of  $\Re(H(\omega))$  with respect to  $\omega$  at  $\omega = 0$ , i.e. the filter (5) is of second order. Based on the exponential filter, also higher-order low-pass filters can be constructed by repeated application of the primary low-pass filter  $H$  (Pruett *et al.* 2006). The use of higher-order filters allows a better control over the separation between damped and undamped frequencies. For specific cases, i.e. if the separation between instability mode and relevant flow phenomena is small, such a filter can be beneficial, e.g. in terms of convergence rate. Figure 1 displays the transfer function of 10<sup>th</sup>-order filter (degree  $N = 4$ , i.e. four applications of the exponential filter) with adapted filter width. This is one particular case of the general formulation where the shape of the filter transfer function can be tailored for specific demands (Kailath 1980).

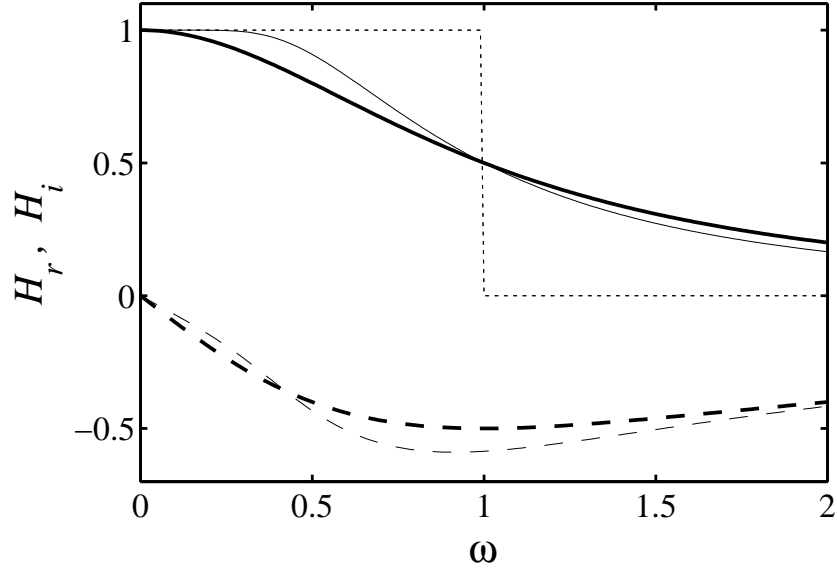


FIGURE 1. Real and imaginary part of the transfer function  $H$  of the exponential filter for degree  $N = 0$  and  $N = 4$ , filter width  $\Delta = 1$ . ———  $H_r^0$ , ———  $H_r^4$ , - - - -  $H_i^0$ , - - - -  $H_i^4$ , ..... spectral (ideal) cutoff filter.

#### 4. Stabilization of unstable steady solution

Analysis of the dynamics of the augmented system is presented in order to elucidate the stabilization procedure and quantify the effect of the control parameters. Considering system (2) with the exponential temporal filter (6), i.e.  $w = \bar{q}$ , the new system becomes

$$\left. \begin{aligned} \dot{q} &= f(q) - \chi(q - \bar{q}) \\ \dot{\bar{q}} &= (q - \bar{q})/\Delta \end{aligned} \right\}. \quad (7)$$

The effect of the regularization can be illustrated by considering the eigenvalues of system (7) linearized about the steady state. Introducing the Jacobian  $A$  of  $f$  at the steady state  $q_s$ , the linearized system is

$$\begin{pmatrix} \dot{q} \\ \dot{\bar{q}} \end{pmatrix} = \begin{pmatrix} A - \chi I & \chi I \\ I/\Delta & -I/\Delta \end{pmatrix} \begin{pmatrix} q \\ \bar{q} \end{pmatrix}. \quad (8)$$

Assume  $\mu = \mu_r + i\mu_i$  is a complex eigenvalue of  $A$  (i.e.  $-i\mu\phi = A\phi$ ) with corresponding eigenvector  $\phi$ . Observation of the structure of system (8) suggests that the eigenvectors of the new system will be  $[\phi, \alpha\phi]^T$  where  $\alpha$  is a complex number to be determined, and the corresponding eigenvalue will be

$\lambda = \lambda(\mu, \alpha, \chi)$ . Introducing this ansatz in (8),  $\alpha$  and  $\lambda$  are obtained as

$$\begin{aligned}\alpha^\pm &= \frac{-F \pm \sqrt{F^2 + 4\Delta\chi}}{2\Delta\chi}, \text{ with } F := \Delta(-i\mu - \chi) + 1, \\ \lambda^\pm &= \mu - i\chi(1 - \alpha^\pm).\end{aligned}\tag{9}$$

The two solutions  $\alpha^+$  and  $\alpha^-$  give two eigenvalues  $\lambda^+$  and  $\lambda^-$  for the modified system, originating from the same eigenvalue  $\mu$  of the original system. The eigenvalue  $\lambda^+$  can be seen as the damped original eigenmode, whereas  $\lambda^-$  is roughly associated to the filtering and corresponds to the  $1/\Delta$  term in (8). The mapping  $\mu \rightarrow \lambda^\pm$  in the complex plane is illustrated in figure 2 for parameters  $\chi = 0.02$  and  $\Delta = 15$ . Two lines are represented (indicating possible eigenvalues  $\mu$  of the original system), with imaginary parts 0.01 and  $-0.03$ , respectively. (These regions approximately correspond to the eigenvalues we are interested to damp in the cavity flow presented below). Each line is mapped into two curves, the dashed one corresponding to  $\lambda^+$ , and dash-dotted line to  $\lambda^-$ . The arrows indicate how two points of the original solid lines are mapped into the new eigenvalues. It can be seen that points with large real part (corresponding to large circular frequency) are simply damped, i.e. shifted downwards, by a constant value  $\chi$ , with virtually no shift along the real axis. Points of small real part are moved towards the origin exhibiting both a decrease in frequency and change in growth rate (imaginary part). The width of the hump forming at low frequencies is related to the filter cutoff frequency, i.e.  $1/\Delta$ . It should be noted that a stable eigenvalue  $\mu$  with low frequency will never be mapped into the unstable region.

In summary, the filter cutoff  $\omega_c$  is related to the frequency of the relevant instabilities and should be smaller than those frequencies at which perturbation growth is expected. The gain  $\chi$  is related to the growth rates of the instabilities and should be large enough to move the instability modes to the lower half plane. However, choosing a large  $\chi$  will render the system evolution slow, since the low-frequency eigenvalues associated with the filter,  $\lambda^-$ , move towards the origin of the complex plane. The system will eventually converge to a steady state, but very slowly owing to the low damping rates. In order to have  $\lambda^+$  as the least damped eigenvalue,  $\chi$  needs to satisfy  $\mu_i < \chi < \mu_i + 1/\Delta$ . Similarly, when choosing  $\Delta$  large, the additional eigenvalues, whose imaginary parts cluster around  $\omega_c = 1/\Delta$ , will make the subsystem for  $\bar{q}$  very slow. A balance has to be found for each system at hand to obtain quick convergence of all the time scales of the system. Testing several parameter pairs on the linear system (8) can be helpful. In cases where the Jacobian  $A$  cannot be approximated, like for the separation bubble presented below, the frequency of the instability can be estimated by considering the resulting unstable flow. As a guideline, the regularization parameter  $\chi$  is chosen to be twice the growth rate of the dominant disturbance. The cutoff frequency,  $\omega_c = 1/\Delta$  is chosen in such a way that the unstable disturbances are well within the damped region,

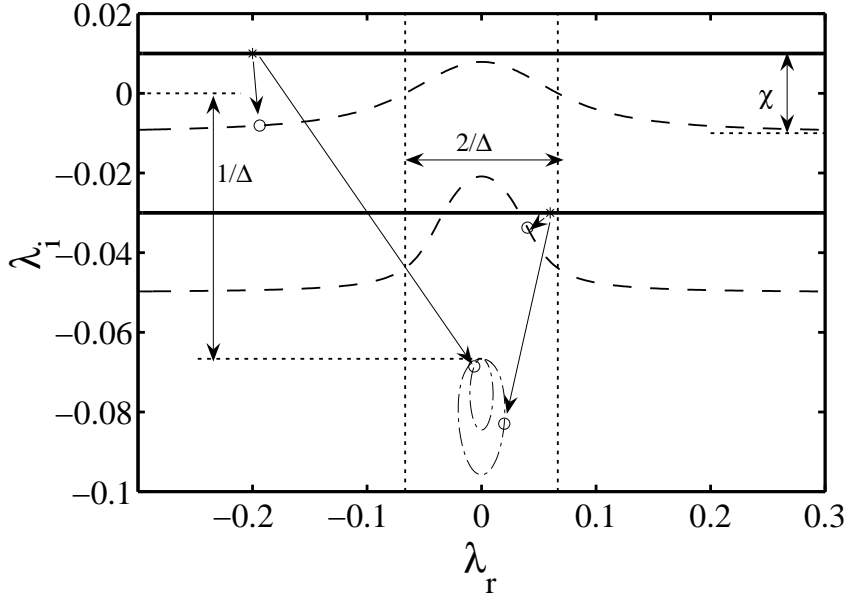


FIGURE 2. Mapping of two lines ( $\mu_i = 0.01$  and  $\mu_i = -0.03$ , —) in the complex plane due to the modified (linear) system (8). Two points originate from each complex eigenvalue  $\mu$ , one point corresponding to  $\lambda^+$  (----) and one corresponding to  $\lambda^-$  (-·-·).  $\chi = 0.02$ ,  $\omega_c = 1/\Delta = 1/15$ .

e.g.  $\omega_c \approx 1/2 \omega_{\text{dist}}$ . If the growth rate is unknown, one can estimate  $\chi$  to be slightly smaller than  $\mu_i + 1/\Delta \approx 1/\Delta$  assuming small  $\mu_i$ .

## 5. Results

The selective frequency damping (SFD) method is applied to compute the steady state of the two-dimensional flow over a long cavity, and of the separation bubble induced by an external pressure distribution. Implementation of the present method into an existing code amounts to increasing the memory to store the filtered variable  $\bar{q}$ , adding the forcing term in the original time-marching scheme and advance the linear equation (6).

The streamfunction pertaining to the steady state of the cavity-driven separated flow is displayed in figure 3, where the streamwise and wall-normal coordinates are made non-dimensional with the inflow boundary-layer displacement thickness  $\delta^*$ . The inflow profile is the Blasius profile at Reynolds number  $Re_{\delta^*} = 350$ . This value has been chosen by gradually increasing it until a global unstable flow is obtained. The streamwise extent of the computational domain is  $L_x = 409$ , with the cavity being confined to an area of  $x \in [30, 150]$ ,

whereas the wall-normal height is  $L_y = 80$ . The numerical code uses fourth-order central finite differences and Chebyshev collocation in the streamwise and wall-normal direction, respectively. The time integration is carried out by a semi-implicit second-order backward Euler/Adams-Bashforth scheme as described in Marquillie & Ehrenstein (2003). Time history of the streamwise velocity measured just above the cavity is shown in figure 4 for two different simulations. In the first simulation, the SFD is active from the beginning of the computation where a zero initial condition is used, whereas in the second simulation SFD is switched on at time  $t = 3000$ . Both simulations eventually converge to the exact same steady state, in one case smoothly and in the other by damping the existing oscillations, the saturated unstable global mode.

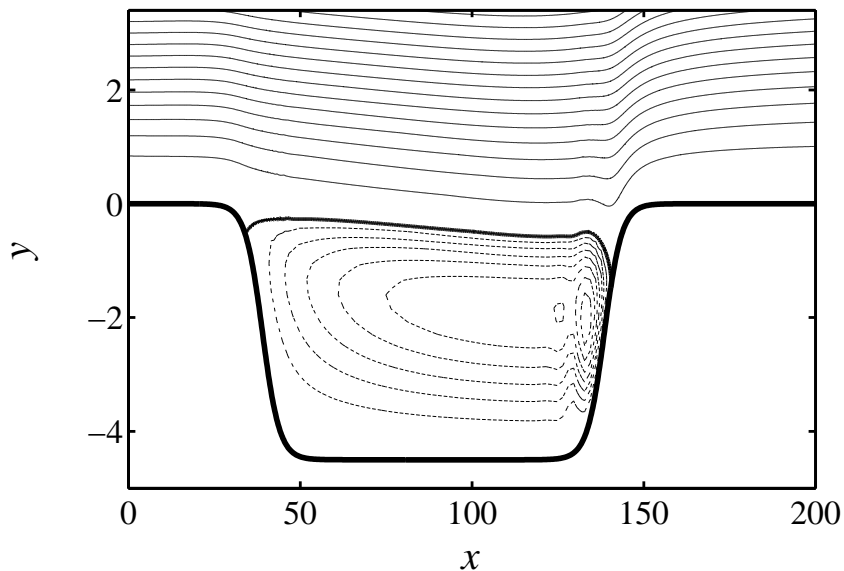


FIGURE 3. Contour lines of the steady-state streamfunction for the cavity case. Zero streamfunction is indicated by the thick line, solid lines indicate positive values with spacing 0.2, dotted lines negative values (spacing 0.025). The recirculation zone inside the cavity and the upward flow motion at the point of reattachment of the shear layer are clearly visible.

In the case of the separation bubble, a flow field subject to a pressure gradient prescribed via the streamwise velocity at the upper boundary is computed. The equations are solved in vorticity-velocity formulation, with the relaxation term  $-\chi(\vartheta_z - \bar{\vartheta}_z)$  being added to the right-hand side of the transport equation

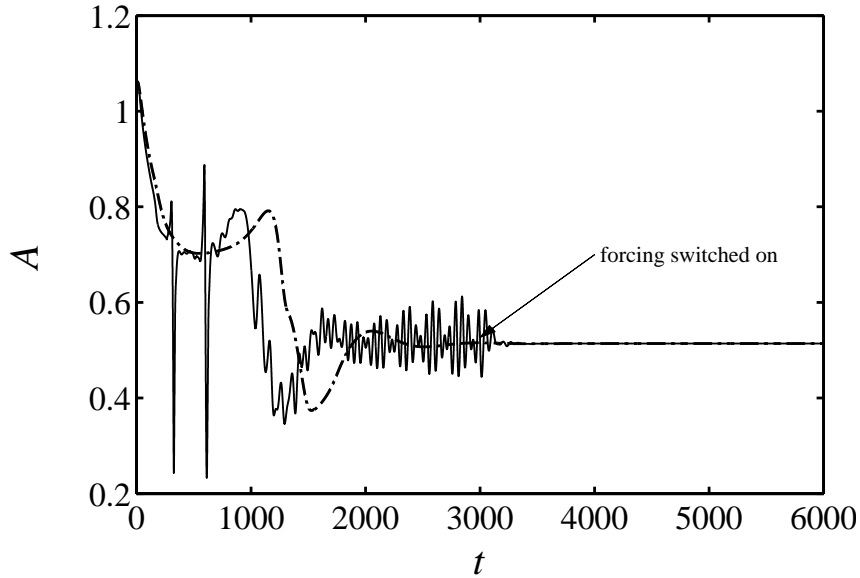


FIGURE 4. Time history of streamwise velocity measured just above the cavity at  $x = 153.4$ ,  $y = 0.8485$ . (---): Simulation started with zero initial condition. (—): SFD turned on at  $t = 3000$ . Both cases are converging to identical steady states.

for the spanwise vorticity  $\vartheta_z$ . The code uses fourth/sixth-order finite differences on a Cartesian grid for the streamwise and wall-normal discretization together with an explicit fourth-order Runge-Kutta time integration (Kloker 1998). For the present case, a Blasius profile is prescribed at the inflow ( $Re_{\delta^*}=1000$ ) while at the upper boundary, the streamwise velocity is quickly decreasing to about 10% of the free-stream velocity and then increasing again. The box size is  $L_x \times L_y = 562 \times 64$ , and  $\chi=0.4$ ,  $\Delta=0.75$ . Two different resolutions ( $801 \times 193$  and  $1601 \times 385$ ) were used, with the time step adapted accordingly. The resulting steady state is shown in figure 5. To check convergence towards an exact solution of the steady equations, the absolute difference between the filtered and the unfiltered vorticity  $\vartheta_z - \bar{\vartheta}_z$  was sampled over time and its maximum in the domain is plotted in figure 6. Without the SFD, no steady state could be reached. The damped oscillatory behavior visible in figure 6 is not related to the frequency of the vortex shedding. It is conjectured that this is an indication of a stable oscillatory movement of the bubble itself, i.e. so-called flapping of the separation bubble. Note that the quantity  $\vartheta_z - \bar{\vartheta}_z$  displayed in figure 6 is in fact proportional to both the amplitude of the relaxation term and the time derivative of the evolution equation of the filtered solution,  $\bar{\vartheta}_z$ . The simultaneous

vanishing (to order  $10^{-6}$ , which is sufficiently accurate for most applications) of  $\partial\bar{\vartheta}_z/\partial t$  and the relaxation term as  $t$  becomes large implies that  $\vartheta_z$  and  $\bar{\vartheta}_z$  each essentially attain time independence; that is, a steady state has been achieved. Additionally, both grid resolutions showed the exact same convergence behavior which further stresses the point that an actual physical solution has been found. We also checked that no drifting of the steady solution is present by considering the evolution of  $\vartheta_z(t+T) - \vartheta_z(t)$  over time  $t$  with  $T$  being large compared to the dominant shedding frequency. A similar behavior as in figure 6 was found and the diagram is therefore not shown here. In the case of the laminar separation bubble, the flow parameters are not incremented to follow a bifurcation but the pressure distribution is chosen arbitrarily to have an unstable flow. We thus show that the method allows attainment of a steady state without any initial guess. Of course, the initial condition becomes relevant in cases where multiple steady states coexist.

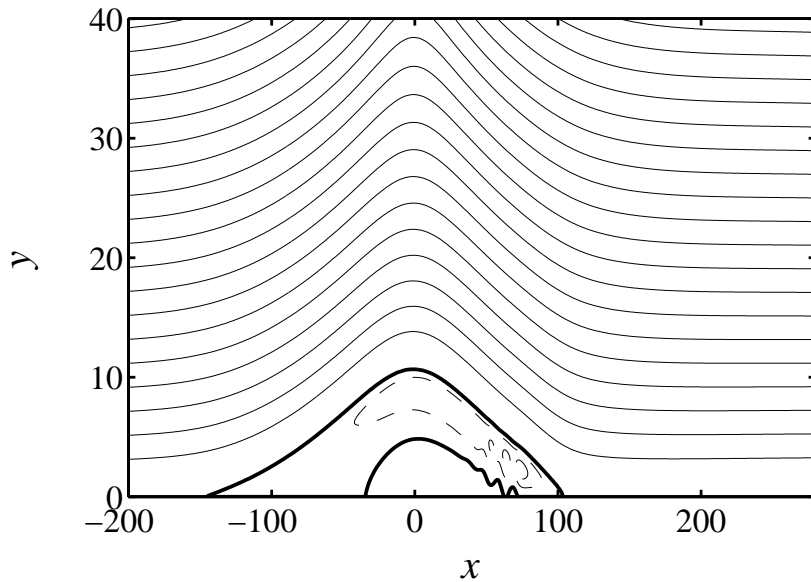


FIGURE 5. Contour lines of the streamfunction for the separation bubble. Zero streamfunction is indicated by the thick line, solid lines indicate positive values with spacing 0.1, dashed lines negative values (spacing 0.005).

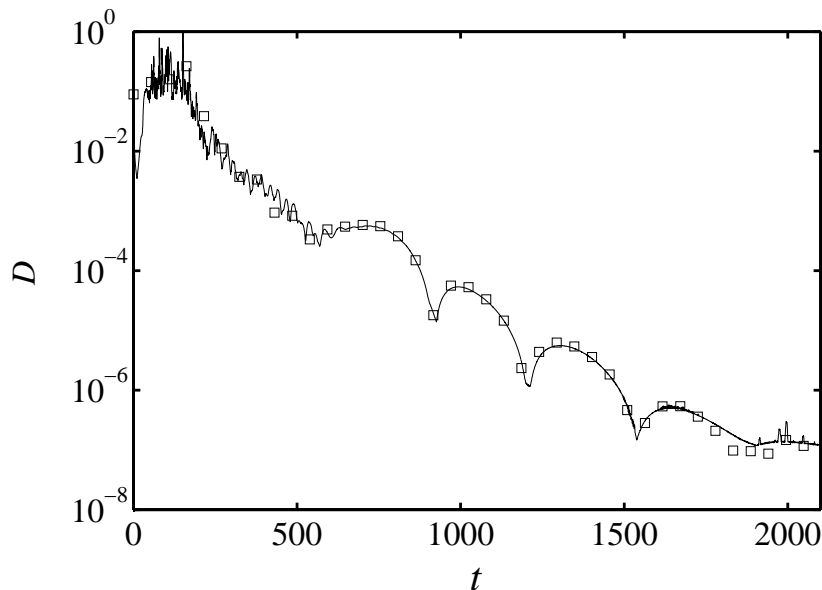


FIGURE 6. Convergence towards steady state for the separation-bubble case, showing the maximum difference between the filtered and unfiltered vorticity field,  $D = \max_{x,y} |\vartheta_z - \bar{\vartheta}_z|$ . — lower resolution,  $\square$  higher resolution.

## 6. Conclusions

A simple numerical approach to compute steady solutions of the Navier-Stokes equations is presented. The most attractive advantages of such a strategy can be summarized as follows. It is easy to implement into an existing numerical code; it does not require a good initial guess of the solution; steady states can be computed without specific knowledge of the critical bifurcation parameters. To our experience, the SFD method appears to be very robust, and therefore this procedure provides a viable alternative to the classic Newton method.

## Acknowledgements

The authors wish to acknowledge a fruitful discussion with Arne Nordmark (KTH Mechanics). P.S. thanks financial support by the Göran Gustafsson Stiftelse. O.M. acknowledges the Deutsche Forschungsgemeinschaft DFG under grant Ma 3916/1-1. Ulrich Rist and Markus Kloker (IAG, University of Stuttgart) and Uwe Ehrenstein (University of Nice-Sophia Antipolis) are thanked for providing the DNS codes.

## References

- CHOMAZ, J.-M. 2005 Global instabilities in spatially developing flows: non-normality and nonlinearity. *Annu. Rev. Fluid Mech.* **37**, 357–392.
- KAILATH, T. 1980 *Linear systems*. Prentice Hall.
- KLOKER, M. J. 1998 A robust high-resolution split-type compact fd scheme for spatial direct numerical simulation of boundary-layer transition. *Appl. Sci. Res.* **58**, 353–377.
- MARQUILLIE, M. & EHRENSTEIN, U. 2003 On the onset of nonlinear oscillations in a separating boundary-layer flow. *J. Fluid Mech.* **490**, 169–188.
- PRUETT, C. D., GATSKI, T. B., GROSCH, C. E. & THACKER, W. 2003 The temporally filtered Navier–Stokes equations: Properties of the residual stress. *Phys. Fluids* **15** (8), 2127–2140.
- PRUETT, C. D., THOMAS, B. C., GROSCH, C. E. & GATSKI, T. B. 2006 A temporal approximate deconvolution model for LES. In *Phys. Fluids*, **18** (028104), 1–4.
- SCHLATTER, P., STOLZ, S. & KLEISER, L. 2004 LES of transitional flows using the approximate deconvolution model. *Int. J. Heat Fluid Flow* **25** (3), 549–558.
- STOLZ, S., ADAMS, N. A. & KLEISER, L. 2001 An approximate deconvolution model for large-eddy simulation with application to incompressible wall-bounded flows. *Phys. Fluids* **13** (4), 997–1015.
- TADMOR, E. 1989 Convergence of spectral methods for nonlinear conservation laws. *SIAM J. Numer. Anal.* **26** (1), 30–44.
- THEOFILIS, V. 2003 Advances in global linear instability analysis of non-parallel and three-dimensional flows. *Prog. Aerosp. Sci.* **39** (4), 249–315.



# Paper 3

3



# Optimal growth, model reduction and control in a separated boundary-layer flow using global eigenmodes

By **Espen Åkervik**<sup>1</sup>, **Jérôme Hoëpfner**<sup>2</sup>, **Uwe Ehrenstein**<sup>2</sup> and **Dan S. Henningson**<sup>1</sup>

<sup>1</sup> Linné Flow Centre, KTH Mechanics, SE-100 44 Stockholm, Sweden

<sup>2</sup> IRPHE, Université de Provence, F-13384 Marseille Cedex 13, France

Two-dimensional global eigenmodes are used as a projection basis both for analysing the dynamics and building a reduced model for control in a prototype separated boundary-layer flow. In the present configuration, a high aspect ratio smooth cavity-like geometry confines the separation bubble. Optimal growth analysis using the reduced basis shows that the sum of the highly non-normal global eigenmodes are able to describe a localized disturbance. Subject to this worst-case initial condition, a large transient growth associated with the development of a wavepacket along the shear layer followed by a global cycle related to the two unstable global eigenmodes is found. The flow simulation procedure is coupled to a measurement feedback controller, which senses the wall shear stress at the downstream lip of the cavity and actuates at the upstream lip. A reduced model for the control optimization is obtained by a projection on the least stable global eigenmodes, and the resulting linear-quadratic-gaussian controller is applied to the Navier–Stokes time integration. It is shown that the controller is able to damp out the global oscillations.

---

## 1. Introduction

Open flows, such as boundary layers, wakes and mixing layers are subject to convective instabilities, where the flow acts as an amplifier of disturbances as they are transported downstream. For some of the flow cases and in particular parameter ranges, self-sustained oscillations may occur. This self-sustaining mechanism can be captured by the unstable global eigenmodes of the linearized Navier–Stokes operator. However, a combination of damped global modes is also capable of representing convective instabilities in non-parallel flows (Cossu & Chomaz 1997; Schmid & Henningson 2002; Ehrenstein & Gallaire 2005). Numerical investigations performed by Marquillie & Ehrenstein (2003) addressed separated boundary-layer flow produced by two-dimensional bump geometries. They showed that elongated separation bubbles are likely to undergo bursting

leading to unsteadiness. By confining the recirculation bubble between two successive bumps on the plate, Marquillie & Ehrenstein (2003) interpreted the flow oscillations in terms of the existence of a global saturated mode oscillating at a well-defined period. Building on their findings we introduce a smooth high aspect-ratio (length to depth ratio  $L/D \approx 25$ ) cavity-like geometry, which induces a geometrically confined separation bubble in the boundary-layer flow as seen in figure 1. Note that this flow case differs from the sharp-edged small aspect-ratio (typically  $L/D = 2$ ) high Reynolds number compressible cavity flow arising in aerospace applications (see e.g. Rowley & Williams 2006). We view this flow case as a prototype separated flow, where both streamwise non-normality and global instability play a central role. In this non-parallel configuration global eigenmodes of the linearized Navier–Stokes operator becomes a natural tool for stability analysis. In this paper we first show that a sum of the non-normal global modes well describes the development of a wavepacket and the onset of a global oscillating cycle associated with the two unstable eigenmodes. Given this ability to reproduce the flow dynamics, the eigenmodes are used as a basis for a Petrov/Galerkin projection in view of model reduction for control.

During the last decade modern control theory has increasingly been applied to fluid flow problems, given the available computer capacities and sensor/actuator developments. Linear optimal control theory has been introduced to flow systems governed by linear instability mechanisms (Bewley & Liu 1998), as for instance spatially developing boundary layers (Högberg & Henningson 2002) and it may also be relevant for nonlinear flows, such as turbulent boundary-layers (Kim 2003). Optimal control of fluid flow based on full state-space representation of the flow field necessitates manipulation of very high-dimensional dynamical systems. In weakly non-parallel flow configurations the problem may become tractable by determining control and estimation kernels for individual wavenumbers in the approximately homogeneous space directions (Högberg & Henningson 2002). In practical flow situations full state information is not available, hence the flow state must be estimated based on sensor measurements. The estimation process can be seen as an optimal filtering problem using a Kalman filter, based on the linearized Navier–Stokes equations. Appropriate stochastic models for the relevant statistics of sensor noise and external disturbances are essential in order to extract the relevant information from the system (Hæpffner *et al.* 2005). In the present work we use the linear quadratic gaussian (LQG) control synthesis, where the two sub-problems of full information control and estimation are solved separately in an optimal manner. Combining the two leads to an optimal measurement feedback control, where the estimated flow is used for control feedback (see e.g. Lewis & Syrmos 1995).

The design of the controller is intimately related to model reduction and the usual procedure is that of projecting the equations onto a subspace. One

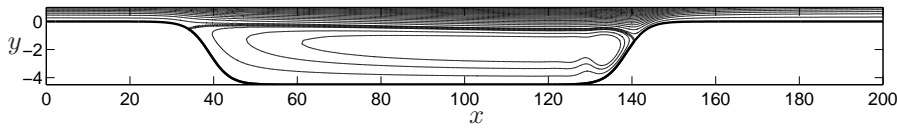


FIGURE 1. Streamlines of steady state base flow solution used for stability analysis at  $Re = 350$ . The thick line represents the zero level contour. Note the large aspect ratio of  $L/D \approx 25$  and the smooth lips.

possible approach is to use the proper orthogonal decomposition modes of the excited flow, thereby capturing the high-energy content of the flow. Balanced truncation provides a more attractive basis by selecting vectors that are equally controllable and observable. When the system becomes large (e.g. 1000 states or more) the standard approach of directly solving Lyapunov equations needed for balanced truncation becomes intractable. Rowley (2005) discussed a computationally tractable approach to obtaining the balancing vectors, based on time-marching algorithms. In globally unstable flow configurations, the global eigenmodes of the linearized Navier–Stokes system form a natural projection basis due to their immediate physical interpretation. For instance one can judge the best placement of the sensors and actuators for observability and controllability, intimately connected to the localization of the least stable direct and adjoint modes respectively (Chomaz 2005).

## 2. Flow configuration and numerical methods

The Navier–Stokes equations are solved in the domain  $0 \leq x \leq 400$ ,  $\eta(x) \leq y < 80$ , large enough to recover freestream uniform flow. All variables are made non-dimensional with the displacement thickness  $\delta^*$  and the free-stream velocity  $U_\infty$  at the inflow  $x = 0$ , where a blasius profile is prescribed. The Reynolds number is defined as  $Re = U_\infty \delta^* / \nu$ , where  $\nu$  is the kinematic viscosity. The function  $\eta(x)$  is the graph of the wall. The smooth cavity is symmetric with respect to its centre at  $x_c = 89$ , and its upstream part is given by  $\eta(x) = -2.25 (\tanh(a(x - b)) + 1)$ ,  $0 \leq x \leq x_c$  with  $a = 0.2$  and  $b = 39$  matching smoothly the flat plate upstream and downstream.

The streamlines in a subset of the computational domain for the steady state at  $Re = 350$  are depicted in figure 1. Note that the main effect of the smooth cavity is the generation of a recirculation zone and a shear layer. The Direct Numerical Simulation (DNS) procedure has previously been used in Marquillie & Ehrenstein (2003). Accounting for wall curvature a mapping transforms the physical coordinates into the computational ones, which are discretized using fourth-order finite differences in streamwise direction (with 2048 grid points) and Chebyshev-collocation in the vertical direction (with 97 collocation points).

2.1. *Steady state*

We found that above  $Re = 325$  the flow became subject to self-sustained oscillations. For a general geometry of this type it is the Reynolds number combined with the length to depth ratio  $L/D$  and the non-dimensional depth  $D/\delta^*$  that constitutes the relevant non-dimensional quantities, however when fixing the length and depth of the smooth cavity the Reynolds number is the only relevant bifurcation parameter. In a globally unstable regime any noise present in the high order numerical discretization will grow exponentially, making it impossible to numerically compute a steady-state solution by standard time-marching methods. Therefore the technique proposed in Åkervik *et al.* (2006) is used to recover the steady state at the current Reynolds number of  $Re = 350$ . The Navier–Stokes equations are forced by adding a term proportional to the difference between the flow state and a filtered solution. If  $\dot{q} = \text{NS}(q)$  represents the nonlinear Navier–Stokes system, the modified system reads

$$\dot{q} = \text{NS}(q) - \chi(q - \bar{q}), \quad \dot{\bar{q}} = (q - \bar{q})/\Delta, \quad (1)$$

where the rightmost equation represents the differential form of a causal low-pass temporal filter. The steady state of (1) is also a steady state of the Navier–Stokes system. A filter width of  $\Delta = 15$  has been chosen such that the frequencies of the instability are targeted and a damping coefficient  $\chi = 0.02$  was found to be appropriate (see Åkervik *et al.* 2006).

2.2. *Eigenmodes*

The global eigenmodes are computed linearizing the Navier–Stokes system about the steady state  $\mathbf{U}(x, y) = (U(x, y), V(x, y))$ . The disturbance flow field  $\mathbf{u}(x, y, t) = \hat{\mathbf{u}}(x, y) e^{-i\omega t}$  and pressure  $p(x, y, t) = \hat{p}(x, y) e^{-i\omega t}$  satisfy the partial differential system

$$-i\omega \hat{\mathbf{u}} = -(\mathbf{U} \cdot \nabla) \hat{\mathbf{u}} - (\hat{\mathbf{u}} \cdot \nabla) \mathbf{U} - \nabla \hat{p} + \frac{1}{Re} \nabla^2 \hat{\mathbf{u}}, \quad (2)$$

$$0 = \nabla \cdot \hat{\mathbf{u}}. \quad (3)$$

After discretization this is written

$$-i\omega_l \mathbf{B} \mathbf{q}_l = \mathbf{A} \mathbf{q}_l \quad \text{with adjoint} \quad i\omega_l \mathbf{B}^H \mathbf{q}_l^+ = \mathbf{A}^H \mathbf{q}_l^+ \quad (4)$$

for the eigenfunction  $\mathbf{q}_l$  with corresponding adjoint eigenfunction  $\mathbf{q}_l^+$ ,  $\mathbf{B}$  is the projection of the total disturbance field on the velocity components;  $\mathbf{A}^H$  is the adjoint discretized operator (conjugate transpose) and the bi-orthogonality condition  $\langle \mathbf{q}_k, \mathbf{B} \mathbf{q}_l^+ \rangle = \delta_{kl}$  with respect to the finite-dimensional inner product applies. The operators of the eigenvalue problem have been discretized on a domain of extent  $0 \leq x \leq 300$ ,  $\eta(x) \leq y \leq 75$ , sufficiently large to produce converged eigenmodes. Homogeneous Dirichlet boundary conditions are used at all boundaries except at the outflow, where Neumann condition is imposed.

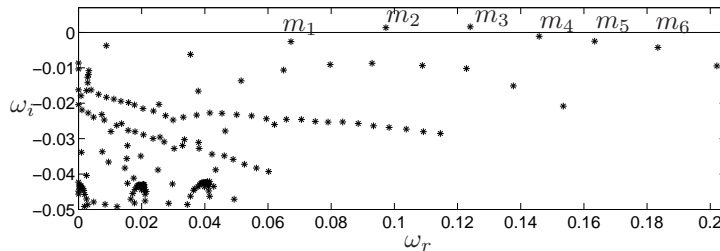


FIGURE 2. Eigenvalues of the direct problem (4). There are two unstable modes. The modes labelled  $m_1 - m_6$  is depicted in figure 3.

The domain is mapped into  $[-1, 1] \times [-1, 1]$  and a Chebyshev-Chebyshev collocation discretization is used. The basic steady flow is then interpolated on the new grid. A similar procedure has been used in Ehrenstein & Gallaire (2005) for the computation of global modes in the flat plate boundary layer. A collocation grid with  $350 \times 65$  collocation points yielded converged stability results. The resulting eigenvalue problem is far too large to be solved by standard  $QZ$  algorithms. However Krylov subspace projections with dimension  $m = 800$  together with the Arnoldi algorithm (see Nayar & Ortega 1993) proved suitable to recover the part of the spectrum relevant for our analysis.

For the steady state shown in figure 1 the spectrum is depicted in figure 2. For the present parameters there are 2 unstable eigenvalues labelled  $m_2$  and  $m_3$  (only half of the spectrum with  $\omega_r > 0$  is shown). Figure 3a)-f) show the vertical velocity components of the direct eigenfunctions associated with the eigenvalues labelled  $m_1 - m_6$  in figure 2, respectively. As can be seen, there are many similar eigenfunctions, a typical feature of non-normal operators, and in the following section we will describe the implications of this when it comes to optimal growth. The vertical velocity component of the adjoint eigenfunction corresponding to the least stable eigenvalue  $m_3$  is depicted in figure 3g). We observe a clear separation in space between the direct (see figure 3c)) and adjoint eigenfunctions, indicating a strong streamwise non-normality (see Chomaz 2005).

### 3. Optimal growth

For sufficiently low-amplitude flow perturbations  $\mathbf{q}(t)$ , an eigenmode expansion

$$\mathbf{q}(t) = \sum_{l=1}^N \kappa_l(t) \mathbf{q}_l, \quad (5)$$

can be used to describe the flow dynamics. The flow evolution is initiated by superimposing the optimal initial condition  $\mathbf{q}_0$  to the steady state, leading to

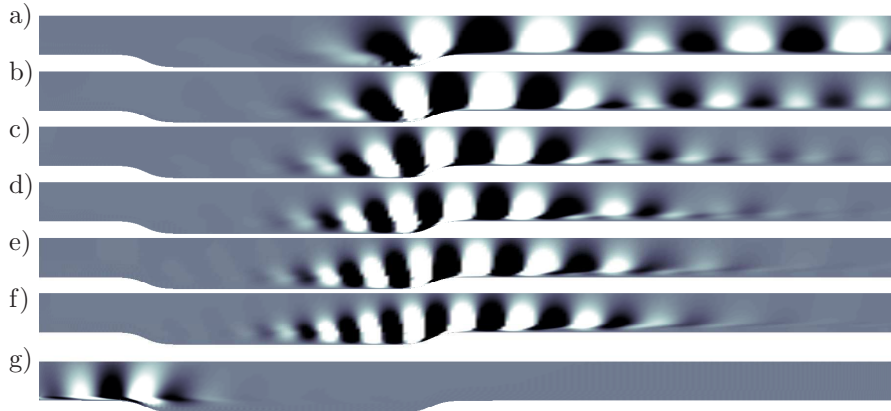


FIGURE 3. a)-f) Vertical velocity components of direct eigenfunctions corresponding to the eigenvalues labelled  $m_1 - m_6$  in figure 2, respectively. g) Adjoint eigenfunction corresponding to  $m_3$ , the most unstable eigenvalue. Black indicates large negative values and white indicates large positive values, with the grey tones adjusting accordingly. The domain is truncated at  $y = 14$ .

the maximum energy growth  $\|\mathbf{q}(t)\|_E$  at a given time  $t$ :

$$G(t) = \max_{\mathbf{q}_0 \neq 0} \frac{\|\mathbf{q}(t)\|_E}{\|\mathbf{q}_0\|_E}.$$

The procedure to compute the optimal initial condition is outlined in Schmid & Henningson (2001) and the subsequent energy envelope for the present flow case is depicted in figure 4a). Using one mode we observe the exponential growth of the most unstable mode. All of the direct eigenfunctions shown in figure 3 are similar; they are oscillatory and exponentially growing along the shear layer. By optimally summing the non-normal eigenmodes, cancelling results in an upstream located initial wavepacket, leading to a fast transient energy growth up to  $t = 200$ , followed by a global cycle with a period of approximately 300 time units. This cycle is associated with the least stable eigenvalues in figure 2. Since the real parts of these modes are a distance of  $\delta \approx 0.02$  apart, and the corresponding eigenfunctions have a very similar structure, they have the ability to cancel each other, giving rise to a “beating” with a period of  $2\pi/\delta$ . Schmid & Henningson (2002) observed the same phenomena studying a model equation for a falling liquid curtain. Figure 4b) shows the actual energy evolution when integrating the eigenmode system (thick line) and DNS system (thin line) in time using the optimal initial condition based on 100 modes, confirming the ability of the eigenmode system to describe the relevant flow dynamics. Note

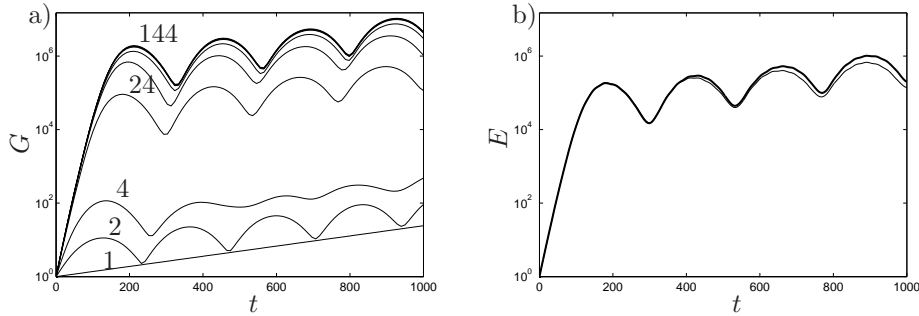


FIGURE 4. a) Envelope of maximum energy growth from initial conditions. The different lines correspond to increasing number of eigenmodes included in the optimization, 1, 2, 4, 24,  $\dots$ , 124, 144 from bottom to top. b) One realization using initial condition based on 100 modes, thick line shows eigenmode system integrated in time and thin line shows DNS evolution.

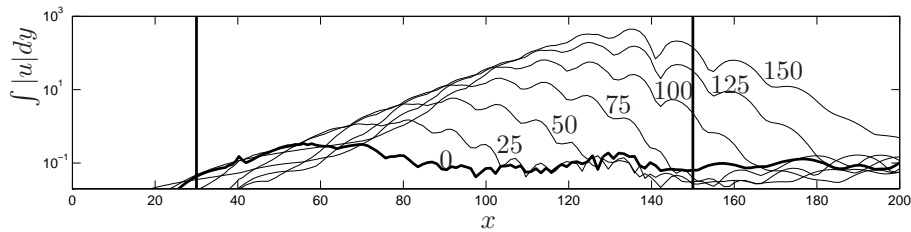


FIGURE 5. Snapshots of  $y$ -integrated streamwise velocity at times 0, 25,  $\dots$ , 150, showing propagation of wavepacket in the eigenmode system. The thick line shows the initial disturbance. The vertical lines indicate the approximate start and end of the recirculation region.

that in the DNS system the initial condition is superimposed to the steady state.

The initial evolution of the wavepacket in the eigenmode system is shown in figure 5. We observe the spatial exponential growth in disturbance amplitude as the wavepacket propagates along the shear layer. The spatio-temporal diagram of the dynamics in the DNS system is depicted in figure 6, where one sees the convection and growth of the wavepacket along the shear layer, and regeneration at the upstream cavity lip. A global pressure change, visible in the form of vertical rays, occurs when the wavepacket reaches the downstream cavity lip; the subsequent propagation of the regenerated wavepacket is emphasized by the oblique line. This instability mechanism may be seen as a destabilization of

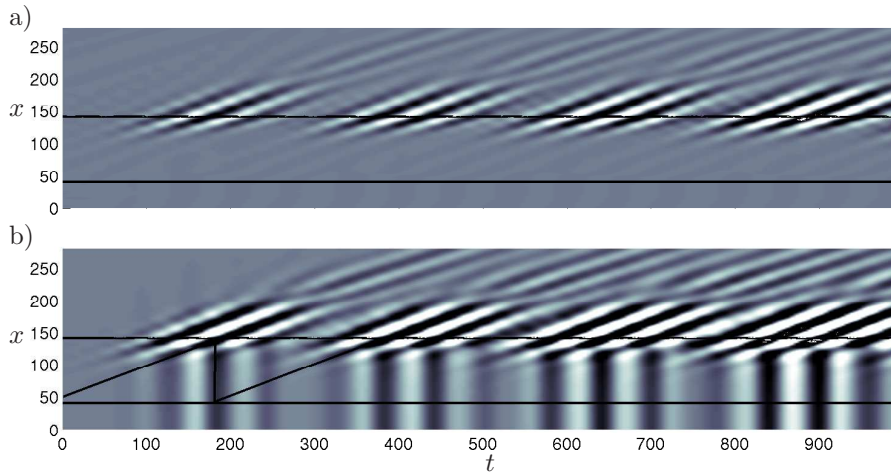


FIGURE 6.  $x/t$  diagram for a) the vertical flow velocity at  $y = 2$  and b) the pressure at  $y = 10$ , tracing the quantities in the streamwise direction and in time at their respective vertical position. Black indicates large negative values whereas white indicates large positive values. The flow initial condition is the optimal initial condition. The horizontal lines show the location of the cavity lips. The oblique lines trace the path of the wavepacket back to its origin and the triggering position at the upstream lip of the cavity at the first reflection.

the global mode by the pressure field, where the pressure yields an immediate feedback mechanism and the strong streamwise non-normality causes a large growth of the disturbances along the shear layer.

#### 4. Control

To control the cavity flow, we introduce one sensor and one actuator as sketched in figure 7. The actuator is located at the upstream limit of the cavity, where the least stable adjoint eigenfunctions have their maximum, so as to trigger the most efficient response. The least stable adjoint eigenfunction is shown in figure 3b). The sensor is placed in the vicinity of the downstream cavity lip where the eigenfunctions have large amplitude. The sensor measures the wall shear stress  $\int \mathcal{C}(x)(\partial u/\partial y)dx$ , where  $\mathcal{C}(x)$  is a Gaussian function with a width of  $\approx 20$ . This operation may formally be written as  $r = C^{DNS}q$  for the flow state  $q$ . The actuator is a volume forcing of Gaussian shape on the vertical velocity component located close to the wall at the upstream cavity lip, with a width of  $\approx 20$  and a height of  $\approx 2$ .

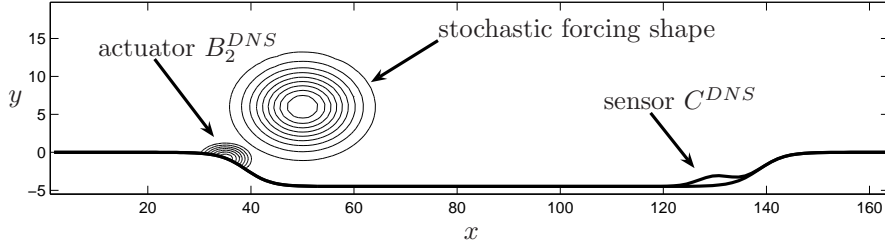


FIGURE 7. Sketch of the control setting, with a volume forcing actuator, and a wall skin friction sensor.

A dynamic model for the cavity flow is built using the eigenmode expansion (5). Based on this model a LQG control procedure gives rise to the system

$$\begin{cases} \dot{k} = Ak + B_1 w + B_2 \phi, & r = Ck + g, \\ \dot{k}_e = Ak_e + B_2 \phi - L(r - r_e), & r_e = Ck_e, \\ \phi = Kk_e. \end{cases} \quad (6)$$

The vector  $k(t) = [\kappa_1(t), \dots, \kappa_N(t)]^T$  of the expansion coefficients of the flow obeys the model dynamics, where  $A$  is the diagonal matrix of the eigenvalues. The external disturbances are modelled as white noise stochastic input  $w(t)$  with variance  $W$ , and  $B_1$  is the projection on the eigenmodes of the Gaussian-shaped spatial forcing function centered at  $x = 50$ . The projected actuator is denoted  $B_2$ , and  $\phi(t)$  is the actuation signal. These projections are achieved by performing the inner product with the adjoint modes. The measurement is denoted  $r$ , and  $C$  is the measurement matrix. The measurement is corrupted by a stochastic sensor noise  $g(t)$  with variance  $G^2$ . An estimator is built, with estimated state  $k_e$ , obeying the model dynamics, and with an estimation feedback forcing  $L(r - r_e)$ . The estimation gain  $L$  will be designed such that the estimated state  $k_e$  converges to the flow state  $k$ , *i.e.* minimizes the mean kinetic energy of the estimation error  $k - k_e$ . The control actuation  $\phi$  is a feedback of the estimated flow state, with control feedback gain  $K$  that will be designed such as to minimize a weighted sum of the flow mean kinetic energy and the actuation effort.

A central issue is the controllability and observability of the flow for the chosen actuator and sensor pair. Since, as observed in §3 the eigenmodes capture the relevant dynamics, the magnitude of the projections  $B_2$  and  $C$  of the actuator and sensor indicate the controllability and observability for each eigenmode. In this manner one can choose the shape and location of the actuator and sensor based on the magnitude of these coefficients on the relevant modes as a measure of the quality of the representation of the actuator and sensor in the reduced system. We have checked that the response from an

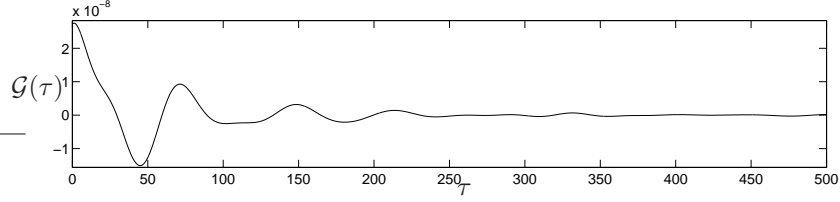


FIGURE 8. Impulse response  $\mathcal{G}(\tau)$  from measurement signal to control signal. The controller uses information from about 350 time units in the past.

impulsive input from the actuator in the DNS and in the eigenmode system give the same measurement signal in the two systems.

The optimal feedback gains  $K$  and  $L$  that minimize the flow and estimation error mean kinetic energy are found by the solution of two algebraic Riccati equations (see Skelton 1988)

$$\begin{aligned} 0 &= A^H X_c + X_c A - X_c B_2 \ell^{-2} B_2^H X_c + Q, \\ 0 &= A X_e + X_e A^H - X_e C^H G^{-2} C X_e + B_1 W B_1^H, \end{aligned}$$

for the matrix unknowns  $X_c$  and  $X_e$ , and the feedback gains can be obtained as  $K = -\ell^{-2} B_2^H X_c$  and  $L = -X_e C^H G^{-2}$ . In our computations, we have assumed an external disturbance  $w$  with unit variance ( $W = 1$ ). The control penalization and sensor noise variance were chosen  $\ell = 5 \cdot 10^5$  and  $G = 7 \cdot 10^5$  in order to enforce low amplitude feedback gains. The matrix  $Q$  is defined such that  $k^H Q k$  measures the kinetic energy of the disturbances.

Once the two Riccati equations are solved and the feedback gains are obtained, we can couple the flow and the controller in the following manner

$$\dot{q} = \text{NS}(q) + B_2^{DNS} \phi, \quad r = C^{DNS} q \quad (7)$$

$$\dot{k}_e = (A + B_2 K + L C) k_e - L r, \quad \phi = K k_e \quad (8)$$

where  $B_2^{DNS}$  and  $C^{DNS}$  are the actuator and sensor expressed in the DNS. The measurement  $r$  is driving the estimated state  $k_e$ , which in turn is updated online by a Crank-Nicholson time-integration procedure, feeding back at every time step the control signal  $\phi$  to the DNS.

To emphasize the linear relation between the measurement signal and the control signal through the controller system, we can write

$$\phi(t) = \int_0^\infty \underbrace{K e^{(A+B_2 K+L C)\tau} L}_{\mathcal{G}(\tau)} r(t-\tau) d\tau, \quad r(t) = 0, t < 0, \quad (9)$$

where  $\mathcal{G}(\tau)$  is the impulse response from  $r$  to  $\phi$ , and illustrates how the actuation  $\phi(t)$  depends on past measurements  $r(t-\tau)$ . The impulse response is shown in figure 8. Note that this formulation could provide an alternative

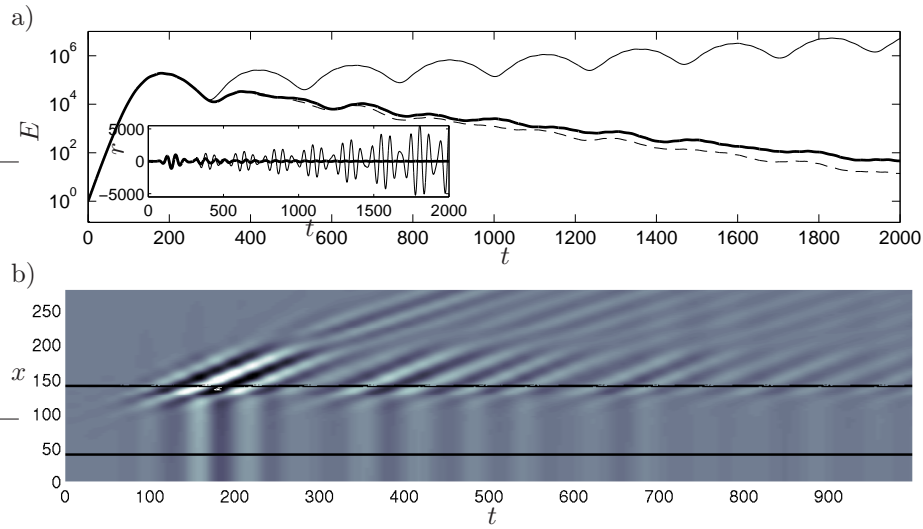


FIGURE 9. a) Energy of the uncontrolled flow (*thin solid line*), controlled flow using model with 4 modes (*thick solid*) and 25 modes (*dashed*). Inserted frame shows the sensor signal in the uncontrolled case as *thin solid line* and controlled using 4 modes as *thick solid line*. b)  $x/t$  diagram for the pressure when the control is applied. This is to be compared to figure 6b).

hardware implementation of the controller. In order to assess the performance of the computed control and estimation gains the controller is applied to the same configuration that led to the evolution shown in figure 6. Reduced models consisting of the 25 and the 4 least stable eigenmodes are considered. Figure 9a) shows that when control is applied, the exponential energy growth is turned into exponential decay after the first peak. There is an almost equivalent performance for both controller dimensions. The sensor signals for the controlled and uncontrolled case are shown in the inserted frame in figure 9a). The sensor signal from the controlled case decays after the first reflections of the wavepacket at  $t \approx 125$ . It is not possible to control the initial energy growth, before the wavepacket has reached the sensor located at the downstream cavity lip. The  $x/t$  diagram for the controlled flow in figure 9b) is to be compared with figure 6b). When the control is applied one still observes the vertical rays of the global pressure changes but the wavepacket regeneration is reduced, leading to a decrease in the levels of fluctuations at each cycle, *i.e.* flow stabilization.

## 5. Conclusions

The cavity flow considered here may be seen as a prototype of non-parallel flow with self-sustained global instability behaviour. Due to the non-normality of the underlying operator, computed eigenmodes are sensitive to numerical errors and require high resolution even when using spectral collocation. This sensitivity is however mostly seen in loss of accuracy for the location of eigenvalues in the complex plane; the mechanism of wavepacket propagation followed by pressure reflections obtained through optimally summing the non-normal modes proved robust and in close agreement with DNS, even at lower resolution. Despite the fact that about 100 modes are required for converged results of optimal growth, much fewer modes are needed for a stabilizing controller. There is only a negligible loss of control performance when using as few as 4 modes in the reduced model. The small controller is run in parallel to the DNS at a low computational cost, and provides the feedback control signal based on the measurement signal taken from the full DNS. The satisfactory performance of the controller, combined with the low online computational effort provides promising perspectives of using reduced order models for fluid flows, built by projection on global eigenmodes in the LQG framework.

## References

- ÅKERVIK, E., BRANDT, L., HENNINGSON, D. S., HEPFFNER, J., MARXEN, O. & SCHLATTER, P. 2006 Steady solutions of the Navier–Stokes equations by selective frequency damping. *Phys. Fluids* **18**, 068102.
- BEWLEY, T. R. & LIU, S. 1998 Optimal and robust control and estimation of linear paths to transition. *J. Fluid Mech.* **365**, 305.
- CHOMAZ, J. M. 2005 Global instabilities in spatially developing flows: non-normality and nonlinearity. *Annu. Rev. Fluid Mech.* **37**, 357.
- COSSU, C. & CHOMAZ, J.M. 1997 Global measures of local convective instability. *Phys. Rev. Lett.* **77**, 4387–90.
- EHRENSTEIN, U. & GALLAIRE, F. 2005 On two-dimensional temporal modes in spatially evolving open flows: the flat-plate boundary layer. *J. Fluid Mech.* **536**, 209.
- HEPFFNER, J., CHEVALIER, M., BEWLEY, T. R. & HENNINGSON, D. S. 2005 State estimation in wall-bounded flow systems. part I: Laminar flows. *J. Fluid Mech.* **543**, 263.
- HÖGBERG, M. & HENNINGSON, D. S. 2002 Linear optimal control applied to instabilities in spatially developing boundary layers. *J. Fluid Mech.* **470**, 151.
- KIM, J. 2003 Control of turbulent boundary layers. *Phys. Fluids* **15**, 1093.
- LEWIS, F. & SYRMOS, V. 1995 *Optimal control*. John Wiley and Sons, New York.
- MARQUILLIE, M. & EHRENSTEIN, U. 2003 On the onset of nonlinear oscillations in a separating boundary-layer flow. *J. Fluid Mech.* **490**, 169.
- NAYAR, M. & ORTEGA, U. 1993 Computation of selected eigenvalues of generalized eigenvalue problems. *J. Comput. Phys.* **108**, 8.
- ROWLEY, C. R. 2005 Model reduction for fluids, using balanced proper orthogonal decomposition. *Int. J. Bifurcation and Chaos* **15**, 997–1013.
- ROWLEY, C. R. & WILLIAMS, D. R. 2006 Dynamics and control of high-reynolds-number flow over open cavities. *Annu. Rev. Fluid Mech.* **38**, 251–276.
- SCHMID, P. J. & HENNINGSON, D. S. 2001 *Stability and Transition in Shear Flows*. Springer, New York.
- SCHMID, P. J. & HENNINGSON, D. S. 2002 On the stability of a falling liquid curtain. *J. Fluid Mech.* **463**, 163–171.
- SKELTON, R. E. 1988 *Dynamics System Control*. John Wiley and Sons, New York.



# Paper 4

4



# Two-dimensional optimal growth in the flat plate boundary-layer flow

By **Espen Åkervik<sup>1</sup>**, **Uwe Ehrenstein<sup>2</sup>**, **François Gallaire<sup>3</sup>**,  
**Dan S. Henningson<sup>1</sup>**

<sup>1</sup> Linné Flow Centre, KTH Mechanics, SE-100 44 Stockholm, Sweden

<sup>2</sup> IRPHÉ, Université de Provence, F-13384 Marseille Cedex 13, France

<sup>3</sup> Laboratoire J.A. Dieudonné, Parc Valrose, F-06108 Nice Cedex 02, France

The stability of a two-dimensional flat plate boundary-layer flow is studied by means of global eigenmodes. The superposition of these modes, depending on both the streamwise and wall-normal coordinate, describes both the Tollmien-Schlichting (TS) wave evolution and the so called Orr mechanism. The transient growth analysis shows that when optimizing for small times the optimal is a disturbance growing due to the Orr-mechanism which is located downstream, near the end of the computational box, and the growth scales linearly with the outflow Reynolds number. When optimizing for larger times the optimal initial disturbance is located upstream in the form of Orr type of structures giving rise first to a tilting with the shear and then the onset of a TS-wave like wavepacket. Optimal forcing analysis is performed as well, giving again rise to a optimal forcing function with Orr-type structure leaning against the shear. The expansion of the flow dynamics in two-dimensional temporal stability modes is hence shown to provide an alternative way, with respect to the conventional locally parallel flow assumption, of studying the instability of the flat-plate boundary-layer.

---

Boundary layers, jets and mixing layers are commonly referred to as open flows, where disturbances are amplified while being advected downstream. In these so called convectively unstable configurations, the disturbances relax in the absence of external disturbances. For certain parameter ranges, for example if the backflow in separated boundary layers becomes large, the flow might become absolutely unstable. Instead of constantly requiring external input to maintain the flow disturbances, pockets of absolutely unstable regions support self-sustained oscillations. Following a phase of linear growth of the global mode, there is a saturation into a non linear limit cycle with the absolutely unstable flow domain acting as a wavemaker shedding vorticity into the convectively unstable region. When the flow under consideration is slightly non-parallel it is possible to determine criteria for transition from globally stable,

to convectively unstable and finally to absolutely unstable based on classical local analysis (Huerre & Monkewitz 1990). In local analysis the streamwise and spanwise directions of the flow are taken to be homogeneous, yielding eigenvalue problems depending only on the wall normal direction. When the length scales of the disturbances becomes comparable to those of the base flow, which is the case for highly non-parallel flows, it is clear that one has to resort to a global formulation of the stability problem, treating also the streamwise direction as inhomogeneous. The resulting matrix eigenvalue problem is typically very large, but owing to increased computer capabilities and efficient large scale eigenvalue solving strategies based on Krylov methods it is nowadays tractable to compute eigenmodes for many flow cases.

As the relevance of global analysis is well established for highly non-parallel flows (Åkervik *et al.* 2007), there are still some important issues to be dealt with when it comes to applying this methodology to slightly non-parallel situations. Considering the model problem of the Ginzburg-Landau with spatially varying coefficients, Cossu & Chomaz (1997) demonstrated that the non-normality of the streamwise eigenmodes leads to transient growth. This non-normality is considered to be associated with the streamwise separation of the direct and adjoint global modes due to the basic advection (Chomaz 2005). Schmid & Henningson (2002) advocated the robustness of optimally summing the streamwise eigenmodes when studying a model problem for a falling liquid curtain, as the sum of modes in contrast to single modes yielded results, in agreement with experiments. The use of global modes as a tool for studying the stability characteristics of the slightly non-parallel boundary-layer flow was addressed in Ehrenstein & Gallaire (2005). They found that a superposition of the damped global eigenmodes associated with Tollmien-Schlichting (TS) type of structures gave rise to a localized wavepacket at the inflow boundary. The wavepacket would grow while being advected downstream, in close agreement with direct numerical simulation results.

It is now well established that when incoming disturbances exceed a certain amplitude threshold the flat-plate boundary layer is likely to undergo transition due to three-dimensional instabilities through the lift-up effect (Ellingsen & Palm 1975; Landahl 1980). This transient growth scenario, where streamwise vortices forms into streamwise streaks by the action of the mean flow was studied for a variety of shear flows in the locally parallel assumption in several works (Butler & Farrell 1992; Reddy & Henningson 1993; Trefethen *et al.* 1993). The extension to the non-parallel flat plate boundary layer was performed at the same time by Luchini (2000) and Andersson *et al.* (1999) using the parabolized stability equations.

While emphasizing the strength of three-dimensional disturbances in general shear flows Butler & Farrell (1992) found a two-dimensional instability mechanism not related to the TS-waves. This instability could extract energy from the mean shear by transporting momentum down the mean momentum

gradient through the action of the perturbation Reynolds stress. This means that structures that are tilted against the shear, would first rise to an upright position while borrowing energy from the mean flow, after which the energy is returned to the mean flow and the disturbances decay. They referred to this as the Reynolds stress mechanism, commonly also known as the Orr mechanism.

In this paper we readdress two-dimensional stability mechanisms in the flat-plate boundary-layer flow, by considering the cooperation or competition of the wall-normal non-normal effects responsible for the Orr mechanism and the streamwise non-normal effects triggering the TS-waves, bearing in mind that the latter are the building blocks for the onset of the so-called classical transition in a low-level noise environment (Herbert 1988). The analysis is based on the computation of temporal two-dimensional modes and is hence free from any assumption concerning spatial length-scales. The non-normality of these eigenmodes of the linearized Navier-Stokes operator is shown to lead to large energy gain due to combination of the Orr and TS mechanisms.

The paper is organized as follows. Section 2 is devoted to the description of the numerical tools and convergence results of the global eigenvalue spectrum are provided in Section 3. The optimal initial condition leading to the maximum energy gain is computed and discussed in Section 4. The signalling problem, that is the determination of the optimal harmonic forcing distribution of the Navier-Stokes system, is addressed in Section 5. In particular, the disturbance flow evolution obtained through projection on the set of global eigenmodes is compared to the forced Navier-Stokes dynamics. Some conclusions are provided in Section 6.

## 1. Numerical tools

The Navier–Stokes equations are solved in the domain  $0 \leq x \leq 1000$ ,  $0 \leq y < 80$ , large enough in the wall-normal  $y$ -direction to recover freestream uniform flow.

The Reynolds number is based on the displacement thickness at inflow  $x = 0$  where a Blasius profile is prescribed. The Direct Numerical Simulation (DNS) procedure has previously been used in Ehrenstein & Gallaire (2005). The flow variables are discretized using fourth-order finite differences in streamwise direction (with 5120 grid points) and Chebyshev-collocation in the vertical direction (with 97 collocation points). The disturbance flow field with velocity components  $\mathbf{u}(x, y, t)$  and pressure field  $p(x, y, t)$  satisfy the partial differential equation

$$\frac{\partial \mathbf{u}}{\partial t} = -(\mathbf{U} \cdot \nabla) \mathbf{u} - (\mathbf{u} \cdot \nabla) \mathbf{U} - \nabla p + \frac{1}{Re} \nabla^2 \mathbf{u}, \quad (1)$$

$$0 = \nabla \cdot \mathbf{u}. \quad (2)$$

which after discretization in the space variables can be written

$$\frac{d}{dt}\mathbf{B}\mathbf{q} = \mathbf{A}\mathbf{q}, \quad (3)$$

where  $\mathbf{q} = [\mathbf{u}, p]^T$  and  $\mathbf{B}$  is the projection of the total disturbance field  $\mathbf{q}$  on its velocity components, i.e.  $\mathbf{B}\mathbf{q} = [\mathbf{u}, 0]$ . Note that in (3) for a divergence-free velocity field  $\mathbf{B}\mathbf{A}\mathbf{q} = \mathbf{A}\mathbf{q}$ . Taking the exponential Ansatz for the time dependence  $\mathbf{q}(x, y, t) = \tilde{\mathbf{q}}(x, y)e^{-i\omega t}$  yields the generalized eigenvalue problem

$$-i\omega_l\mathbf{B}\tilde{\mathbf{q}}_l = \mathbf{A}\tilde{\mathbf{q}}_l \quad (4)$$

with a divergence free velocity field  $\tilde{\mathbf{u}}_l$  associated to each eigenmode  $\tilde{\mathbf{q}}_l$ . The box extension in the wall normal direction is  $0 \leq y \leq 40$ . This height was found sufficient to also resolve the eigenvectors associated with the low frequency part of the spectra. In the streamwise direction different lengths have been considered but the main parts of the results are presented for  $0 \leq x \leq 800$ . Indeed the flat-plate boundary layer flow is convectively unstable and the box length will put a bound on the timescale at which the spatially growing disturbance wavepacket leaves the domain. Accordingly, the eigenmodes and the instability mechanisms due to their interactions will also be function of the box length. At the lower wall and at freestream homogeneous Dirichlet conditions are imposed and at inflow and outflow the non-homogeneous Robin conditions proposed in Ehrenstein & Gallaire (2005) has been used. These boundary conditions essentially amounts to matching the streamwise derivative of the global mode with spatial local analysis so that  $\partial\mathbf{u}/\partial x = i\alpha\mathbf{u}$ . The local dispersion relation connecting the wave number  $\alpha$  to the frequency  $\omega$  is nonlinear, but performing a Gaster-type of transformation

$$\alpha \approx \alpha_{0,r} + \frac{\partial\alpha_r}{\partial\omega_r}(\omega_0)(\omega - \omega_0) \cdots \quad (5)$$

yields a good linear approximation, as long as the imaginary parts of the complex frequency and wavenumber are small. Here the real frequency  $\omega_0$  is chosen such that  $\alpha_0 = \alpha_{0,r}$  at the inflow boundary, that is at a frequency of neutral instability for the Blasius profile at inflow. These boundary conditions proved to be suitable to recover a converged set of eigenmodes in one large-scale stability computation, as shown in the next Section. Note that using homogeneous Dirichlet conditions at inflow and Neumann conditions at outflow we obtained a similar spectra but recovered fewer eigenmodes for the same computational parameters. The domain is mapped into  $[-1, 1] \times [-1, 1]$  and a Chebyshev-Chebyshev collocation discretization is used for the stability system. Indeed, Chebyshev-collocation provides the most efficient discretization in terms of grid size, which puts a reasonable bound on the dimension of the resulting generalized matrix eigenvalue problem. Consequently, the basic steady flow computed by means of DNS is interpolated on the new grid (cf Ehrenstein & Gallaire (2005) for details). We have chosen to consider the steady state for the Navier-Stokes system, rather than the self-similar solution of the flat-plate

boundary-layer equation. Indeed, one goal of the present analysis is to compare the Navier-Stokes dynamics with the time evolution of the eigenmodes system. It will be shown in Section 3 that a collocation grid with  $250 \times 45$  collocation points yields converged stability results. The resulting eigenvalue problem is still far too large to be solved by standard  $QZ$  algorithms. Large-scale Krylov subspace projections with dimension  $m = 2000$  together with the Arnoldi algorithm (Nayar & Ortega 1993) proved suitable to provide a complete, with respect to the disturbance dynamics, set of eigenvalues and corresponding eigenmodes.

### 1.1. Mode superposition

When determining the possibility of growth in a flow system the notions of optimal initial condition and optimal forcing are essential. These features are both closely related to the non-normality of the underlying operators (Schmid & Henningson 2001). We will here give a brief summary on how these optimals are computed. The dynamical system (3) obtained after discretization defines an initial value problem by adding the initial condition

$$\mathbf{u}(0) = \mathbf{u}_0 \quad (6)$$

for a divergence-free velocity field  $\mathbf{u}_0$ . We are looking for initial disturbances that maximize the energy at time  $t$

$$G(t) = \max_{\mathbf{u}_0 \neq 0} \frac{\|\mathbf{u}(t)\|_E^2}{\|\mathbf{u}_0\|_E^2}$$

and a convenient form of this expression can be obtained by expanding the solution in terms of the generalized eigenmodes  $\mathbf{u}(t) = \sum_{l=1}^N \kappa_l(t) \tilde{\mathbf{u}}_l$ . Recall that the eigenmodes being solution of the generalized eigenvalue problem (4), the associated velocity fields are divergence free. Hence the flow dynamics is described by

$$\frac{d\kappa}{dt} = \Lambda \kappa, \quad \kappa(0) = \kappa_0, \quad (7)$$

where  $\kappa$  is the vector of expansion coefficients and  $\Lambda$  is a diagonal matrix whose elements are given by  $\Lambda_l = -i\omega_l$ . The maximum growth expressed in this basis reads

$$G(t) = \max_{\kappa_0 \neq 0} \frac{\|\kappa(t)\|_E^2}{\|\kappa_0\|_E^2} = \|\exp(\Lambda t)\|_E^2 = \|F \exp(\Lambda t) F^{-1}\|_2^2. \quad (8)$$

where  $F$  is the Cholesky factor of the Hermitian energy of the Hermitian energy measure matrix  $\mathbf{M}$  with entries  $M_{ij} = \int \tilde{\mathbf{u}}_i^H \tilde{\mathbf{u}}_j dx dy$  expressed in the basis of eigenmodes.

The largest growth at time  $t$  is given by the largest singular value of  $F \exp(\Lambda t) F^{-1}$  and the optimal initial condition  $\kappa_0$  is the corresponding right singular vector. Alternative ways of computing the optimal initial condition is

by calculus of variations (Butler & Farrell 1992) or by time-marching/space-marching algorithms involving the adjoint operator (Luchini 2000; Andersson *et al.* 1999).

Let us now formulate the optimal forcing frequency and the corresponding forcing function. Consider the harmonically forced system

$$\frac{\partial}{\partial t} \mathbf{B} \mathbf{q} = \mathbf{A} \mathbf{q} + \{\mathbf{q}_f \exp -i\Omega t\} \quad \Omega \text{ real.} \quad (9)$$

The asymptotic long time response for the stable system reads

$$\mathbf{q}(t) = -(\mathbf{A} + i\Omega \mathbf{B})^{-1} \mathbf{q}_f \exp -i\Omega t. \quad (10)$$

Expressing the state in the basis of eigenmodes yields

$$\kappa(t) = -(\Lambda + i\Omega I)^{-1} \kappa_f \exp -i\Omega t. \quad (11)$$

The maximum response to the harmonic forcing at a frequency  $\Omega$  expressed in this basis is

$$R(\Omega) = \max_{\kappa_f} \frac{\|(\Lambda + i\Omega I)^{-1} \kappa_f\|_E}{\|\kappa_f\|_E} = \|(\Lambda + i\Omega I)^{-1}\|_E = \|F(\Lambda + i\Omega I)^{-1} F^{-1}\|_2. \quad (12)$$

The norm of the the resolvent is readily obtained as the largest singular value of  $F(\Lambda - i\Omega I)^{-1} F^{-1}$  and the optimal forcing is the corresponding right singular vector, the left singular vector being the corresponding steady state harmonic response. Two different contributors to large resolvent norms may be identified: resonances are triggered whenever the forcing frequency is chosen close to an eigenvalue of the system. On the other hand, optimal forcings may exploit the large condition number of  $F$ , related to the non-orthogonality of the eigenvectors.

## 2. The spectra and convergence of optimals

Figure 1 shows the spectra obtained for the inflow Reynolds number,  $Re_{\delta^*} = 1000$ , based on the local displacement thickness. The box size of  $L_x = 800$ ,  $L_y = 40$  required  $N_x = 250$  and  $N_y = 45$  in order to yield converged results. The largest Krylov subspace size considered is  $m = 2000$ . We found that increasing the number of points in the streamwise direction only moved the most damped eigenvalues, associated with areas of a resolvent norm of the order of  $10^{-6}$  (Trefethen & Embree 2005), however the more robust features such as optimal growth remained unchanged. As can be observed from the figure, there are many eigenmodes coming out of the eigenvalue calculation. Some of them, such as the eigenvalue labelled  $m_1$ , are related to TS type of instabilities. In addition there are slightly damped modes that have their maximum in the freestream, where of one is labelled  $m_2$ . Finally there is a family of highly damped eigenvalues with corresponding eigenfunctions that have a tilted structure, appearing as reflection type of modes, shown in the lower frame of figure 2 and labelled  $m_3$  in figure 1. By selecting only the TS

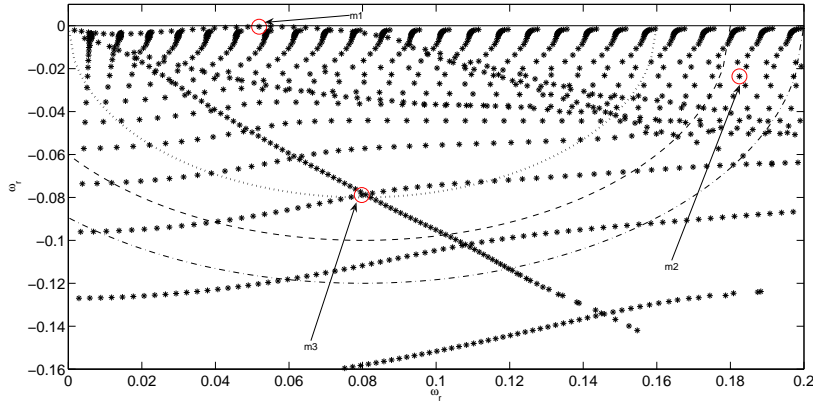


FIGURE 1. Spectra at  $Re_{\delta^*} = 1000$ . Included is also contours in the complex plane indicating size of Krylov subspace according to  $|\omega - \sigma_0| < R$ . (...) shows  $R = 0.08$ , (---) shows  $R = 0.1$  and (-.-) shows  $R = 0.12$ . Eigenvectors corresponding to labels  $m_1$ ,  $m_2$  and  $m_3$  are depicted in figure 2.

type of modes, Ehrenstein & Gallaire (2005) could obtain a growth in energy of one order of magnitude for  $Re_{\delta^*} = 780$  and a box length of 500 for the propagating wavepacket. In this paper we will show that by adding the other types of modes, one obtains a much larger growth which is associated with the combination of the so called Orr mechanism (Butler & Farrell 1992) and the spatio-temporal growth of wavepacket made of TS waves. First the question of convergence in terms of the optimal initial disturbance growth is addressed, by increasing the set of eigenmodes as the projection basis. Figure 1 depicts the spectrum obtained with a very large Krylov subspace of dimension 2000, together with the Arnoldi method using the shift and invert strategy. For a given dimension of a Krylov subspace converged eigenvalues are contained within a circle of radius  $R$  around the shift value which has been taken as  $\omega_s = 0.08$ . Increasing the Krylov subspace dimension is equivalent to drawing a larger circle in the complex space, where eigenvalues are obtained. The resulting eigenvalues hence satisfy

$$|\omega - \omega_s| \leq R \quad (13)$$

where the radius  $R$  depends on how large the Krylov subspace is. Figure 1 shows the radius resulting from three different Krylov subspace sizes on top of the spectra. The optimal growth envelope, as computed according to equation (8), obtained using different truncations is shown in figure 3. It is seen that a radius of  $R = 0.08$  is not sufficient to obtain converged results, whereas for  $R > 0.1$ , one may neglect the modification of the optimal growth envelope induced by a further increase of modes included in the optimization procedure.

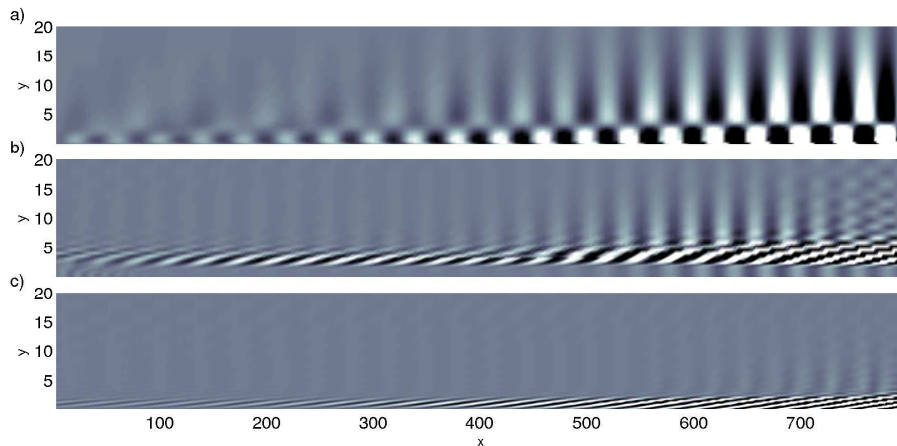


FIGURE 2. Eigenvectors corresponding to the eigenvalues labelled  $m_1$  to  $m_3$  in figure 1. a) ( $m_1$ ) Least stable mode. b) ( $m_2$ ) Freestream reflection mode c) ( $m_3$ ) Boundary layer reflection mode. The last two are typical modes that due to cancelling with other non-orthogonal modes contribute to the so called Orr mechanism.

Cossu & Chomaz (1997), working on the model problem of Ginzburg-Landau mimicking convective growth, conjectured that the more parallel the base flow becomes, the more non-normal the operator becomes and that consequently more modes are needed in order to locate optimal perturbations upstream when the flow is more parallel. We have checked this hypothesis for the present case, and we found that for the more non-parallel case of inflow Reynolds number  $Re_{\delta^*} = 500$  and an equivalent box-length a smaller number of eigenmodes are needed in obtaining converged energy growth (corresponding to a radius of  $R = 0.08$ ).

### 3. Optimal initial condition

In the previous section we mentioned that it was possible to get a larger growth than that obtained when considering only the propagation of the TS type of wavepacket, and that this was due to the Orr mechanism. Figure 4 shows the envelope and actual energy developments in a log scaling, to emphasize the quick growth due to the Orr mechanism. The thick solid line shows the envelope, whereas the thin solid shows the actual energy evolution due to the optimal initial condition with the combined Orr and TS mechanism. From the thin dash-dotted line one can see that the optimal growth due to the pure Orr mechanism is a fast growing fast decaying disturbance.

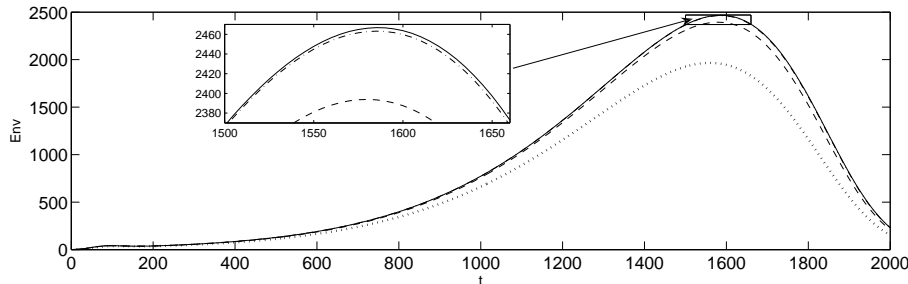


FIGURE 3. Envelope of optimal growth for different Krylov subspace sizes. (...) corresponds to  $R = 0.08$ , (---) to  $R = 0.1$  and (-.-) to  $R = 0.12$ . The solid line shows the envelope including all modes obtained ( $R = 0.16$ ). The small figure shows a zoom at the maximum, indicating that the optimal growth is converged at  $R = 0.12$ .

Note that the growth-factor as well as the corresponding optimal time ( $t = 100$  and  $E = 42.8$ ) are approximately twice as high as those provided by the local analysis of Butler and Farrell for a parallel Blasius boundary layer at  $Re = 1000$  ( $t = 45$  and  $E = 28$ ). However, according to the time evolution of the streamwise velocity during the growth interval displayed in figure 5, it becomes clear, that comparison with the local theory should not be attempted using the inlet Reynolds number  $Re = 1000$  but with a local Reynolds number representative of the location of the initial condition (using for instance the midpoint of the support of the initial perturbation, located at  $x = 610$ , this yields  $Re_{\delta^*} = 1700$ ). We have therefore performed local optimal growth calculations (whenever a local maximum could be defined, since a locally parallel Blasius boundary layer is unstable for a certain wavenumber range), based on a parallel Blasius boundary layers of thickness 1.7 and  $Re = 1700$ , yielding an optimal time  $t = 120$ , optimal growth 34.8, in better agreement with the global optimals. The corresponding optimal wavelength then equals 25 and is depicted by an double arrow in figure 5, comparing favorably with the underlying wavelength making the wavepacket. Our local computations have further shown a tendency for the Orr mechanism of increasing optimal growth, increasing optimal time and increasing optimal wavenumber, when the boundary layer thickness and thereby the Reynolds number both increase. This tendency is clearly illustrated by figure 6 which shows for various box lengths,  $L_x = 800, 600, 400$  for the different frames from top to the bottom, that the optimal initial condition for this pure Orr mechanism is always located as far downstream as possible within the box. In contrast to the downstream located structures that yields the maximum growth for short-time optimization, long time optimization yields structures located far upstream. The energy gain due

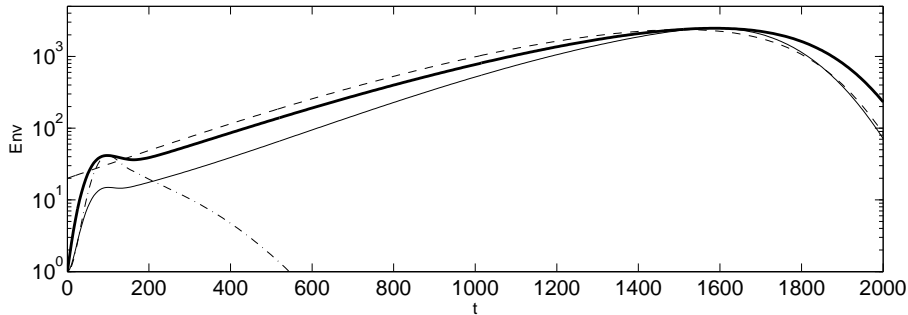


FIGURE 4. Envelope of growth due to worst case initial conditions. Solid thick line shows the envelope using a Krylov subspace corresponding to  $R = 0.12$ , leading to the combined Orr mechanism and the TS wave growth. The thin solid shows the actual energy evolution when using only the initial condition leading to the maximum growth of all times. The thin dash-dotted shows the energy evolution due to the pure Orr mechanism. The dashed thin line shows the envelope obtained when using only the TS type of modes in the optimization, magnified by a factor of 20, i.e. there is a gain of  $\approx 20$  in combining the Orr and TS mechanism.

to the upstream Orr mechanism is only half of that of the downstream located one (compare thin-solid and dash-dotted lines in figure 4), however as can be seen from figure 7 the flow gains energy from rising to an upright position, after which they have the form of a TS type of wavepacket that propagates throughout the domain. The dotted line in figure 4 shows that one through the Orr mechanism has gained a factor of  $\approx 20$  in energy compared to initializing with a clean TS type of wavepacket. This demonstrates that while the long-time behavior of the disturbance is governed by the traveling wavepacket, its starting amplitude is optimized through the Orr mechanism.

#### 4. Optimal forcing

Since boundary layers are convectively unstable, acting thereby as noise amplifiers, a prominent role is played by the response to forcing, rather than by the detailed time-evolution of the initial condition, and the optimal forcing is therefore a relevant measure of the maximum possible growth that may be obtained in the box. While the evolution due to the optimal initial condition can be seen as a wave packet propagating, eventually leaving the computational box (or measurement section), the response from the flow to forcing will be persistent structures that at each streamwise station have a fixed amplitude,

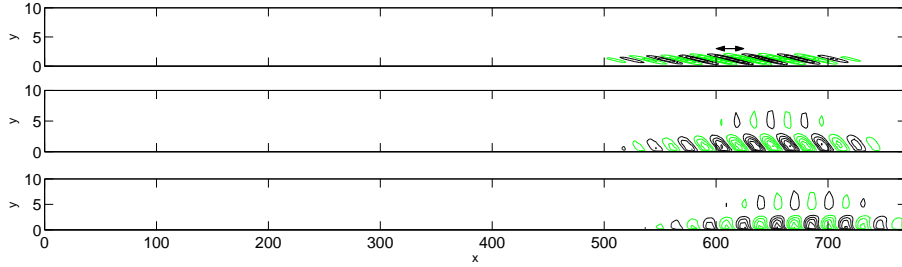


FIGURE 5. Initial condition and response for streamwise velocity with the Orr mechanism. The maximum is located at  $T = 100$  for which  $\frac{E_T}{E_0} = 41.6$ . The double arrow in the upper frame shows the wave length of 25 as predicted by local theory.

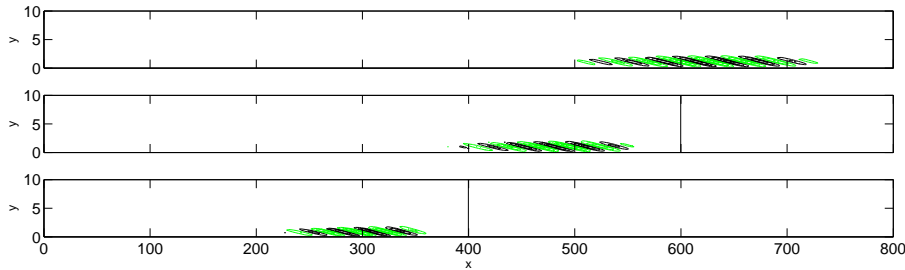


FIGURE 6. Initial conditions corresponding to the pure Orr mechanism for different domain lengths. a)  $L_x = 800$ , b)  $L_x = 600$  and c)  $L_x = 400$ . The vertical lines indicates the end of the computational domain.

oscillating around the mean flow. In this section we are investigating the structure of the optimal forcing and the response at different frequencies. Figure 8 shows the resolvent norm as defined in (12), where a large value indicates a large response to the given frequency real  $\Omega$ . Note that the magnitude of the resolvent norm is both influenced by the distance in the complex plane to the eigenvalues and the condition number of the energy measure. For normal operators the condition number is 1, hence the distance from an eigenvalue and the resolvent coincides. However, we are here dealing with non-normal operators/matrices, where the condition number is considerably larger than 1. The peak of the response is at the frequency  $\Omega = 0.055$  and the streamwise component of the corresponding forcing structure is shown in figure 9. Analogous to the optimal initial condition case, here the optimization procedure produces Orr type of structures. The optimal forcing structure is more elongated in the streamwise direction than the optimal initial condition. The corresponding frequency coincides with the frequency of the least damped eigenmode, however

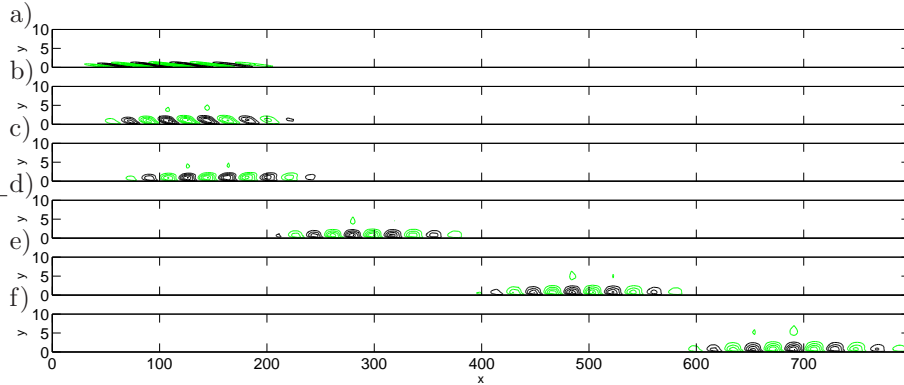


FIGURE 7. Initial condition and response for streamwise velocity with the combined Orr and TS mechanism. Note that the amplitude is growing from frame to frame.

strongly amplified (a factor of  $\approx 40$ ) by non-normal effects. The neutral point for this frequency (branch I) predicted by local theory is located at  $x = 0$ . We would expect the optimal forcing to be located in the vicinity of this neutral point, and indeed the forcing is located close to branch I. For lower frequencies we observe that the optimal forcing structures move further downstream and consists of longer wave lengths.

#### 4.1. Direct Numerical Simulation results

A verification of the ability of the eigenmode system to capture the relevant dynamics of the flow is performed by applying the optimal forcing in DNS. For this purpose the real part of the optimal forcing device  $\mathbf{q}_f \exp(-i\Omega t)$  has been interpolated on the DNS grid and added as a forcing function to the Navier-Stokes system. The time evolution in the eigenmode system is given explicitly by equation (12). Figure 10 shows the pointwise energy integrated in the wall-normal direction, comparing the evolution in the DNS (solid lines) and the eigenmode system (dash-dotted lines). Snapshots are taken at times 80, 720, 1360 and 2000 with the amplitude growing as time increases. The response from the optimal forcing is the Orr mechanism followed by a TS wave. At time 2000 the disturbances has filled the box and the energy reaches a threshold where TS waves occupy most of the domain. The simple evaluation of 919 expansion coefficients yields an evolution in close agreement with the DNS, which for comparison has  $1.5 \cdot 10^6$  degrees of freedom. At time 2000, even though the two systems are in phase an amplitude difference appears, most likely due to nonlinear effects as well as to some possible weak reflections in the eigenmode system.

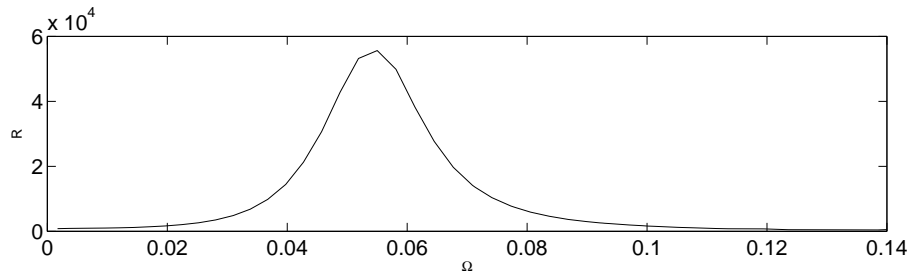


FIGURE 8. Response to forcing at different frequencies. The peak response is at  $\Omega = 0.055$ .

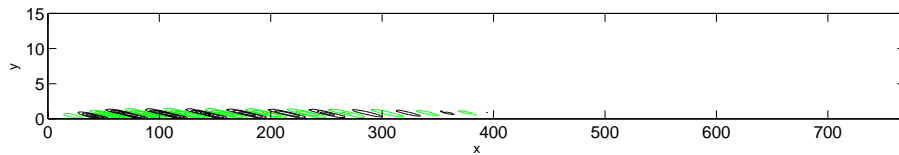


FIGURE 9. Streamwise component of optimal forcing structure.

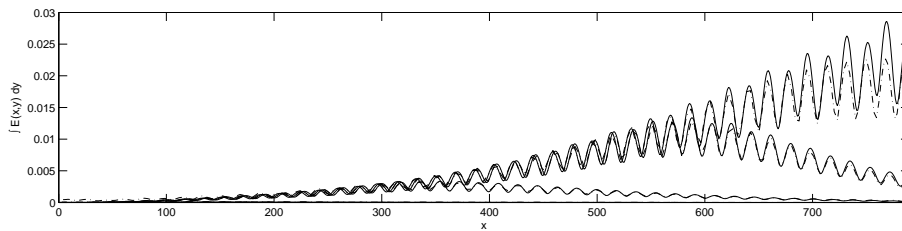


FIGURE 10. Evolution of pointwise energy integrated in wall-normal direction at times 80, 720, 1360 and 2000. Solid lines shows DNS whereas dash-dotted shows eigenmode system. The amplitude is growing with increasing times. Note that at time 2000 the disturbances has filled the box and the energy reaches a threshold where TS waves occupy most of the domain.

## 5. Conclusions

For highly non-parallel flows the validity of the local approach is questionable rendering the global eigenmodes the natural tool for stability analysis. If the flow under consideration is only slightly non-parallel local analysis may still provide correct results, but it is still interesting to establish the stability characteristics of the flow in terms of the global eigenmodes of the operator. The

global eigenmodes provides the “full” description of the dynamics within the computational box. The Arnoldi method using the shift and invert strategy computes the eigenmodes within a Krylov subspace size dependent radius in the complex plane. The computed eigenmodes serve as a reduced basis in view of stability investigations, for which the basic procedure is to study resolvent features such as optimal initial conditions and optimal forcing. For the slightly non-parallel flow case studied here, many eigenmodes are needed in order to obtain converged results in terms of these measures. Both the optimal growth and optimal forcing analysis shows that a combined effect of the Orr and TS-wave mechanism yields a large potential for downstream amplification in this convectively unstable regime. It is the description of the upstream located tilted Orr structures that requires a large number of modes; the description of the TS waves only requires about 20 eigenmodes. Optimal forcing structures are applied both in the eigenmode system and in the DNS, and the subsequent time-evolution in the two systems match very well. This confirms the robustness of optimally summing eigenmodes in order to bring out the important dynamics of the flow.

### **Acknowledgement**

The authors would like to thank Matthieu Marquillie for providing the DNS code and Jérôme Hœpffner for fruitful discussions.

## References

- ÅKERVIK, E., HÖPFFNER, J., EHRENSTEIN, U. & HENNINGSON, D. S. 2007 Optimal growth, model reduction and control in a separated boundary-layer flow using global eigenmodes. *J. Fluid Mech.* Accepted for publication.
- ANDERSSON, P., BERGGREN, M. & HENNINGSON, D. S. 1999 Optimal disturbances and bypass transition in boundary layers. *Phys. Fluids* **11**, 134–150.
- BUTLER, K. M. & FARRELL, B. F. 1992 Three-dimensional optimal perturbations in viscous shear flow. *Phys. Fluids A* **4**, 1637–1650.
- CHOMAZ, J. M. 2005 Global instabilities in spatially developing flows: non-normality and nonlinearity. *Annu. Rev. Fluid Mech.* **37**, 357–392.
- COSSU, C. & CHOMAZ, J. 1997 Global measures of local convective instability. *Phys. Rev. Lett.* **77**, 4387–90.
- EHRENSTEIN, U. & GALLAIRE, F. 2005 On two-dimensional temporal modes in spatially evolving open flows: the flat-plate boundary layer. *J. Fluid Mech.* **536**, 209–218.
- ELLINGSEN, T. & PALM, E. 1975 Stability of linear flow. *Phys. Fluids* **18**, 487–488.
- HERBERT, T. 1988 Secondary instability of boundary layers. *Annu. Rev. Fluid Mech.* **20**, 487–526.
- HUERRE, P. & MONKEWITZ, P. 1990 Local and global instabilities in spatially developing flows. *Annu. Rev. Fluid Mech.* **22**, 473–537.
- LANDAHL, M. T. 1980 A note on an algebraic instability of inviscid parallel shear flows. *J. Fluid Mech.* **98**, 1–34.
- LUCHINI, P. 2000 Reynolds-number-independent instability of the boundary layer over a flat surface: Optimal perturbations. *J. Fluid Mech.* **404**, 289–309.
- NAYAR, M. & ORTEGA, U. 1993 Computation of selected eigenvalues of generalized eigenvalue problems. *J. Comput. Phys.* **108**, 8–14.
- REDDY, S. C. & HENNINGSON, D. S. 1993 Energy growth in viscous channel flows. *J. Fluid Mech.* **252**, 209–238.
- SCHMID, P. J. & HENNINGSON, D. S. 2001 *Stability and transition in shear flows*. Springer.
- SCHMID, P. J. & HENNINGSON, D. S. 2002 On the stability of a falling liquid curtain. *J. Fluid Mech.* **463**, 163–171.

- TREFETHEN, L. N., TREFETHEN, A. E., REDDY, S. C. & DRISCILL, T. A. 1993  
Hydrodynamic stability without eigenvalues. *Science* **261**, 578–584.
- TREFETHEN, N. & EMBREE, M. 2005 *Spectra and Pseudospectra; The Behaviour of nonnormal matrices and operators*. Princeton University Press.